

VIBRATION AND ACOUSTIC NUMERICAL ANALYSIS OF GREGORIAN  
TYPE COMMUNICATION ANTENNA PLANTED ON COMMUNICATION  
SATELLITE

A THESIS SUBMITTED TO  
THE GRADUATE SCHOOL OF NATURAL AND APPLIED SCIENCES  
OF  
MIDDLE EAST TECHNICAL UNIVERSITY

BY

ONUR KAAAN KARAOĞLU

IN PARTIAL FULFILLMENT OF THE REQUIREMENTS  
FOR  
THE DEGREE OF MASTER OF SCIENCE  
IN  
MECHANICAL ENGINEERING

JANUARY 2020



Approval of the thesis:

**VIBRATION AND ACOUSTIC NUMERICAL ANALYSIS OF GREGORIAN  
TYPE COMMUNICATION ANTENNA PLANTED ON COMMUNICATION  
SATELLITE**

submitted by **ONUR KAAAN KARAOĞLU** in partial fulfillment of the requirements  
for the degree of **Master of Science in Mechanical Engineering Department,**  
**Middle East Technical University** by,

Prof. Dr. Halil Kalıpçılar  
Dean, Graduate School of **Natural and Applied Sciences**

\_\_\_\_\_

Prof. Dr. M. A. Sahir Arıkan  
Head of Department, **Mechanical Engineering**

\_\_\_\_\_

Assoc. Prof. Dr. Mehmet Bülent Özer  
Supervisor, **Mechanical Engineering, METU**

\_\_\_\_\_

**Examining Committee Members:**

Assoc. Prof. Dr. Yiğit Yazıcıoğlu  
Mechanical Engineering, METU

\_\_\_\_\_

Assoc. Prof. Dr. Mehmet Bülent Özer  
Mechanical Engineering, METU

\_\_\_\_\_

Assist. Prof. Dr. Orkun Özşahin  
Mechanical Engineering, METU

\_\_\_\_\_

Assist. Prof. Dr. Gökhan Özgen  
Mechanical Engineering, METU

\_\_\_\_\_

Assoc. Prof. Dr. S. Çağlar Başlamışlı  
Mechanical Engineering, Hacettepe University

\_\_\_\_\_

Date: 23.01.2020

**I hereby declare that all information in this document has been obtained and presented in accordance with academic rules and ethical conduct. I also declare that, as required by these rules and conduct, I have fully cited and referenced all material and results that are not original to this work.**

Name, Surname: Onur Kaan Karaođlu

Signature:

## **ABSTRACT**

### **VIBRATION AND ACOUSTIC NUMERICAL ANALYSIS OF GREGORIAN TYPE COMMUNICATION ANTENNA PLANTED ON COMMUNICATION SATELLITE**

Karaođlu, Onur Kaan  
Master of Science, Mechanical Engineering  
Supervisor: Assoc. Prof. Dr. Mehmet Bülent Özer

January 2020, 127 pages

The acoustic load during lift-off of the spacecraft rockets is one of the most destructive loads especially for the light and large space structures. This thesis mainly focuses on vibro-acoustic behavior of a large composite reflector satellite antenna. The study starts with manufacturing processes, material properties and design criteria of the antenna which is Gregorian type with two reflectors. Then, Finite Element Model (FEM) of the antenna which is prepared in HyperMesh is analyzed structurally with calculation of modal and frequency response in MSC. NASTRAN. The FEM model and results are adjusted by using the sine-sweep test results performed on a modal shaker. After obtaining proper FEM model, vibro-acoustic numerical model is constructed and solved in MSC. ACTRAN. One of the strongest parts of this thesis is presenting acoustic test results performed in a reverberant chamber which provides the diffuse sound field. In summary, this thesis presents manufacturing processes of satellite reflector antenna and examines the vibration and acoustic test responses and FEM results with their comparisons.

Keywords: Vibro-Acoustic, Satellite Antenna, Composite, Vibration, Acoustic

## ÖZ

### **HABERLEŞME UYDUSU ÜZERİNE YERLEŞTİRİLMİŞ GREGORYEN TİPİNDEKİ HABERLEŞME ANTENLERİNİN TİTREŞİM VE AKUSTİK SAYISAL ANALİZLERİ**

Karaoğlu, Onur Kaan  
Yüksek Lisans, Makina Mühendisliği  
Tez Danışmanı: Doç. Dr. Mehmet Bülent Özer

Ocak 2020, 127 sayfa

Akustik yükler, uydu roketlerinin fırlatılması sırasında geniş ve hafif yapılar üzerindeki en yıkıcı yüklerden biridir. Bu tez kapsamında, geniş kompozit bir reflektöre sahip olan bir uydu antenin titreşim-akustik davranışlarına odaklanılmıştır. Çalışma, iki reflektörlü Gregoryen tipli bu antenin üretim süreçleri, malzeme özellikleri ve tasarım detaylarıyla başlamaktadır. HyperMesh'te hazırlanan Sonlu Elemanlar Modeli (SEM), modal ve frekans cevap analizleri gibi yapısal analizler MSC.NASTRAN yazılımında çözülmüştür. Model, sarsıcı üzerindeki sinus tarama testlerinin sonuçları kullanılarak güncellenmiştir. Doğrulanmış bir SEM hazırlandıktan sonra, titreşim yanıtı da içeren akustik sayısal model hazırlanmış ve MSC.ACTRAN'da çözdürülmüştür. Bu tezin en güçlü yanlarından biri de yaygın ses dağılımı yaratan çınlama odasında gerçekleştirilen test sonuçlarını sunması ve akustik modelin deney sonuçları ile doğrulanmış olmasıdır. Özetle, bu tez, geniş reflektörlü kompozit uydu antenlerinin üretim süreçlerini sunmakta ve titreşim ve akustik analiz sonuçlarını, test cevaplarını ve bunların karşılaştırmalarını sunmaktadır.

Anahtar Kelimeler: Titreşim-Akustik, Uydu Anteni, Kompozit, Titreşim, Akustik

To my family and friends

## ACKNOWLEDGEMENTS

I would like to express my special regards and gratitude to my advisor Assoc. Prof. Dr. Mehmet Bülent Özer for his excellent support and guidance. From the beginning of thesis period, his knowledge and motivation courage the author to work hard.

I wish to show my gratitude to Mert Atasoy. It is whole-heartedly appreciated that his great advice for the study monumental towards the success of this thesis. His technical support and invaluable assistance will stay in the heart forever.

I would like to thank my colleague Cihan Turgut for his discussions and supports on the space applications.

The opportunities and supports provided by ASELSAN is truly appreciated. Without their support and funding, this project could not have reached its goal.

Also, I wish to express my deepest feelings to my parents, Şengül and Saim; my brothers, Anıl and İlkem. This work would not been possible without their input.

The author also wishes to thank his friends for their support and understanding.

## TABLE OF CONTENTS

ABSTRACT .....	v
ÖZ .....	vi
ACKNOWLEDGEMENTS .....	viii
TABLE OF CONTENTS .....	ix
LIST OF TABLES .....	xii
LIST OF FIGURES .....	xiv
LIST OF ABBREVIATIONS .....	xviii
LIST OF SYMBOLS .....	xx
1. INTRODUCTION .....	1
1.1. Background .....	1
1.2. Motivation of the Thesis.....	3
1.3. Gregorian Type Configuration and Introduction of the Antenna.....	4
1.3.1. Gregorian Type Antenna .....	4
1.3.2. The Antenna.....	5
1.3.2.1. Composite Structures of the Antenna .....	6
1.3.2.2. Metallic Parts of the Antenna.....	7
1.3.2.3. Manufacturing Process.....	8
1.4. Vibro-Acoustic Test .....	11
1.5. Literature Review .....	15
1.6. Simulation Approach used in Numerical Analysis .....	21
1.6.1. Fundamental Composite Material Modelling in Nastran .....	22
1.6.2. Fundamentals of Diffuse Acoustic Field Generation in Actran .....	23

1.6.3. Fundamentals of Acoustic Structural Coupled Analysis in Actran.....	25
1.7. Outline of the Thesis .....	26
2. VIBRATION TESTS AND FEM ANALYSIS OF THE ANTENNA .....	29
2.1. Sine Sweep Test of the Antenna .....	29
2.1.1. Background Information about the Vibration Test .....	29
2.1.2. Vibration Test Set-Up .....	31
2.1.3. Sine Sweep Test Results.....	35
2.2. Vibration FEM Analysis of the Antenna .....	41
2.2.1. FEM Model of the Antenna.....	41
2.2.2. Modal Analysis of the Antenna.....	46
2.2.3. Frequency Response Analysis of the Antenna .....	50
2.2.3.1. Damping and Half-Power Bandwidth Method .....	51
2.2.3.2. Frequency Response Analysis Results .....	53
2.3. Comparisons of the Vibration Tests and FEM Analysis of the Antenna.....	59
3. VIBRO-ACOUSTIC TESTS AND FEM ANALYSIS OF THE ANTENNA...	65
3.1. Vibro-Acoustic Tests .....	65
3.1.1. Background Information about the Vibro-Acoustic Tests .....	65
3.1.1.1. Reverberant Chamber and Test Set-Up .....	67
3.1.2. Vibro-Acoustic Tests of the Fixture .....	73
3.1.3. Vibro-Acoustic Tests of the Antenna .....	77
3.1.4. Discussion of the Vibro-Acoustic Tests .....	86
3.2. Vibro-Acoustic FEM Analysis of the Antenna.....	93
3.2.1. Vibro-Acoustic FEM Model of the Antenna.....	93

3.3. Comparisons of the Vibro-Acoustic Tests and FEM Analysis of the Antenna .....	103
4. CONCLUSION AND FUTURE WORK .....	113
4.1. Conclusion .....	113
4.2. Future Work .....	115
REFERENCES .....	117
A. MSC NASTRAN's Composite Calculations .....	121
B. Additional Sine Sweep Test Data .....	122

## LIST OF TABLES

### TABLES

Table 1.1. Thermal Expansion Coefficients [5,28].....	6
Table 1.2. Mechanical Properties of Used Metals.....	8
Table 1.3. Summary of Vibro-Acoustic Testing .....	12
Table 1.4. Sound Pressure Level Tolerance Limits for Octave Band [10].....	14
Table 1.5. Comparisons of FEM, BEM and SEA[12].....	16
Table 2.1. Sine Sweep Test Information .....	34
Table 2.2. Situations of Each Channels for Tower X-Axis Sine Sweep Test .....	36
Table 2.3. Natural Frequencies of Tower and Main Reflector Resulted From Sine Sweep Test.....	38
Table 2.4. Maximum Responses and Corresponding Frequencies of Tower Sine Sweep.....	40
Table 2.5. Maximum Responses and Corresponding Frequencies of Main Reflector Sine Sweep.....	40
Table 2.6. Finite Element Model Details .....	44
Table 2.7 Properties of the MEFFMASS Card.....	47
Table 2.8 Effective Mass Fractions for Tower .....	47
Table 2.9 Effective Mass Fractions for Main Reflector .....	48
Table 2.10. Tower's Frequency Response Analysis Maximum Values .....	54
Table 2.11. Main Reflector's Frequency Response Analysis Maximum Values .....	55
Table 2.12. Comparison of the Natural Frequencies Obtained From Test and Modal Analysis Results up to 750 Hz.....	60
Table 3.1. Acoustic Loading.....	65
Table 3.2. Vibro-Acoustic Test Sequence .....	67
Table 3.3. Overview of the Data Acquisition of Acoustic Test.....	71

Table 3.4. Acoustic Test: 10 Maximum Response Values, Corresponding Frequencies and Accelerometer ID's .....	81
Table 3.5. Maximum Responses [ $g^2/Hz$ ] of MR2, T8-Z and SR1 Accelerometers at Each Test.....	83
Table 3.6. Acoustic Test: 10 Maximum Response Values of the Tower and Sub-Reflector, Corresponding Frequencies and Accelerometer ID's .....	84
Table 3.7. Natural Frequency Comparison of the Sine-Sweep and Acoustic Test ....	88
Table 3.8. Mesh Dimension and Total Acoustic Element Number for Different Frequencies .....	97
Table 3.9. Damping Values for the First Vibro-Acoustic Analysis.....	98
Table 3.10. Natural Frequency Comparison of the Acoustic/Sine Sweep Tests and Modal/Vibro-Acoustic (1 <sup>st</sup> ) Analyses .....	100
Table 3.11. Natural Frequency Comparisons of the Vibro-Acoustic Test and Analysis .....	103
Table 3.12. Damping Values for the Finalized Vibro-Acoustic Analysis .....	103
Table 0.1. Situations of Each Channels for Sine Sweep Test .....	123
Table 0.2. 273 Natural Frequencies of Tower Subassembly .....	126
Table 0.3. 250 Natural Frequencies of Main Reflector Subassembly.....	127

## LIST OF FIGURES

### FIGURES

Figure 1.1. Launching of Ariane 5 Spacecraft [2] .....	2
Figure 1.2. Gregorian Type Antenna [4] .....	4
Figure 1.3. Principal Components of The Antenna .....	5
Figure 1.4. Sandwich Structure [6].....	7
Figure 1.5. Machining of Sandwich Panels .....	9
Figure 1.6. Composite Assembly and Sticking Processes .....	10
Figure 1.7. Tower and Main Reflector Sub-Assemblies .....	11
Figure 1.8. Schematic of the Diffuse Sound Field [12].....	13
Figure 1.9. Comparison of FEM and SEA results with test data [1] .....	17
Figure 1.10. Comparison FEM, BEM and test results [12].....	18
Figure 1.11. Predicted (FEM) and Measured (Test) Comparisons at Different Locations [17].....	19
Figure 1.12. Comparison of Acoustic Test vs. BEM Analysis [36] .....	20
Figure 1.13. Particular Plane Wave and Corresponding Coordinate System .....	24
Figure 2.1. Coordinate System of the the Antenna.....	30
Figure 2.2. Mounting Holes of the Antenna .....	31
Figure 2.3. Accelerometer Positions of the Vibration Test .....	32
Figure 2.4. Tower and Main Reflector covered by MLI positioned on Shaker.....	33
Figure 2.5. Data Resolution Plot of the Sine Sweep Tests .....	34
Figure 2.6. Sine Sweep Test Results of Tower along X-axis .....	35
Figure 2.7. Sine Sweep Test Results of Main Reflector along X-axis .....	36
Figure 2.8. Sine Sweep Test Results of Tower X-Axis (up to 2000Hz in the log-log scale).....	37
Figure 2.9. Sine Sweep Test Results of Tower X-Axis (up to 750Hz) .....	38
Figure 2.10. CQUAD4 and CTRIA3 elements [25] .....	42

Figure 2.11. PCOMP Card constructing the sandwich composite structure.....	43
Figure 2.12. FEM Mesh of the Antenna via PATRAN.....	45
Figure 2.13. Tower's 1 <sup>st</sup> and 2 <sup>nd</sup> Mode Shapes .....	49
Figure 2.14. Main Reflector's 1 <sup>st</sup> , 2 <sup>nd</sup> , 4 <sup>th</sup> and 8 <sup>th</sup> Mode Shapes .....	50
Figure 2.15. Half-Power Bandwidth Method Schematic [20] .....	52
Figure 2.16. TABDMP1 Card, Damping Ratios of Tower .....	52
Figure 2.17. Frequency Response Analysis Results for Tower in X-axis (to 750Hz) .....	53
Figure 2.18. Displacement and Stress Output of Tower at 90.75 Hz.....	56
Figure 2.19. Displacement and Stress Output of Tower at 97 Hz.....	57
Figure 2.20. Displacement and Stress Output of Main Reflector at 216.5 Hz.....	58
Figure 2.21. Displacement and Stress Output of Main Reflector at 658 Hz.....	58
Figure 2.22. Comparison Plot of T5-X and T7-X accelerometers for Tower X-axis excitation.....	61
Figure 2.23. Comparison Plot of T8-X and T8-Y accelerometers for Tower X-axis excitation.....	62
Figure 2.24. Comparison Plot of MR5-X in X-excitation and MR5-Y in Y-excitation for Main Reflector.....	63
Figure 3.1. SPL Comparisons of Different Launchers with the Turkish Space Program [18, 37, 38, 39] .....	66
Figure 3.2. Reverberation Chamber and Test Setup .....	70
Figure 3.3. Accelerometers on the Acoustic Test Fixture.....	71
Figure 3.4. Accelerometers of the Acoustic Test.....	72
Figure 3.5. SPL of Low Level Acoustic Test of Fixture.....	73
Figure 3.6. SPL of Medium Level Acoustic Test of Fixture .....	74
Figure 3.7. SPL of Qualification Level Acoustic Test of Fixture.....	74
Figure 3.8. Structural Responses of the Fixture Under Acoustic Loading .....	76
Figure 3.9. SPL of Low Level Acoustic Test of Antenna.....	78
Figure 3.10. SPL of Medium Level Acoustic Test of Antenna .....	79
Figure 3.11. SPL of Qualification Level Acoustic Test of Antenna.....	79

Figure 3.12. Comparison of Fixture and Antenna Tests at Qualification Level.....	80
Figure 3.13. Comparisons of Critical Accelerometers of Tower, Main Reflector and Sub Reflector .....	82
Figure 3.14. PSD Responses of MR2 of Different Tests.....	83
Figure 3.15. PSD Responses of SR1 Under Acoustic Loading.....	85
Figure 3.16. PSD Responses of T8-Z Axis Under Acoustic Loading.....	86
Figure 3.17. Structural Responses of the Accelerometers of MR2, T8, SR2, Fixture and WG2 at the Qualification Test Level .....	87
Figure 3.18. Acoustic Test Configuration .....	89
Figure 3.19. Pre and Post Low Level Test Comparison at MR2 Along Normal Axis .....	90
Figure 3.20. Pre and Post Low Level Test Comparison at MR16 Along Z Axis.....	91
Figure 3.21. Pre and Post Low Level Test Comparison at Along Normal Axis .....	91
Figure 3.22. Pre and Post Low Level Test Comparison at T8 Along Z Axis.....	92
Figure 3.23. Antenna inside the Acoustic Domain.....	95
Figure 3.24. Acoustic Mesh and Acoustic-Structure Coupling Surfaces .....	96
Figure 3.25. Modelling of Diffuse Sound Field .....	98
Figure 3.26. Responses of First Vibro-Analysis at MR2, SR1 and T10-Y .....	99
Figure 3.27. Acoustic Test Fixture and its Finite Element Model.....	101
Figure 3.28. Mode Shapes of the Acoustic Test Fixture .....	101
Figure 3.29. Vibro-Acoustic Model and Boundary Conditions .....	102
Figure 3.30. Comparison of the Analysis Results of MR2, SR1 and T10-Y .....	104
Figure 3.31. Comparison of Analysis Results with Test Data at MR2.....	105
Figure 3.32. Comparison of Analysis Results with Test Data at MR16-Z.....	105
Figure 3.33. Comparison of Analysis Results with Test Data at T10-Y .....	106
Figure 3.34. von Mises Stress Outputs of the MR2, MR16 and T10 .....	107
Figure 3.35. Vibro-Acoustic Analysis' Displacement and Stress Results Graphs at 46Hz.....	108
Figure 3.36. Vibro-Acoustic Analysis' Displacement and Stress Results Graphs at 100Hz.....	108

Figure 3.37. Vibro-Acoustic Analysis' Displacement and Stress Results Graphs at 160Hz .....	109
Figure 3.38. Vibro-Acoustic Analysis' Displacement and Stress Results Graphs at 246Hz .....	109
Figure 3.39. Vibro-Acoustic Analysis' Displacement and Stress Results Graphs at 280Hz .....	110
Figure 3.40. Stress and Displacement Graph of Bottom Surface of Brackets at 280Hz .....	110
Figure 0.1. Sine Sweep Test Results of Tower in Y-axis .....	122
Figure 0.2. Sine Sweep Test Results of Main Reflector in Y-axis .....	122
Figure 0.3. Sine Sweep Test Results of Tower Y-Axis (up to 750Hz).....	124
Figure 0.4. Sine Sweep Test Results of Main Reflector X-Axis (up to 750Hz).....	124
Figure 0.5. Sine Sweep Test Results of Main Reflector Y-Axis (up to 2000Hz)....	125

## LIST OF ABBREVIATIONS

### ABBREVIATIONS

FEM : Finite Element Method

BEM : Boundary Element Method

SEA : Statistical Energy Approach

RF : Radio Frequency

OMT : Orthomode Transducer

I/F : Interface

FC : Feed Chain

NASA :National Aeronautics and Space Administration

ECSS :European Cooperation for Space Standardization

ESA : European Space Agency

SPL : Sound Pressure Level

MLI : Multi-Layer Insulation

CAD : Computer Aided Design

PSD : Power Spectral Density

RMS : Root-mean-square

PFM : Proto-Flight Model

DFAT :Direct Field Acoustic Testing

RFAT : Reverberant Field Acoustic Testing

MDOF: Multi Degree of Freedom

MR : Main Reflector

SR : Sub-Reflector

WG : Wave Guide

LL : Low-Level

ML : Medium Level

QL : Qualification Level

## LIST OF SYMBOLS

### SYMBOLS

$c$  : speed of sound

$\rho$  : density

$\lambda$  : wavelength of sound in any medium

$f$  : frequency

$k$  : wave number

$\nu$  : Poisson's ratio

# CHAPTER 1

## INTRODUCTION

### 1.1. Background

This thesis focuses on a Turkish national space antenna of a space program. The satellite has different communication antennas not only for Turkey but also different regions and continents such as Europe, some part of Africa and Middle East and India. The antenna that is designed and manufactured by REHİS (Radar-Electronic Warfare Systems) Group, ASELSAN.

The antenna has a composite sandwich structure which leads to light-weight material and large reflectors. Such antennas which have large and light reflectors are considered as critical under vibro-acoustic loads especially during launching of the rocket. Acoustic loads can be accepted as one of the most destructive loads for the satellite structures [1]. This launching period is significant because of the existence of aerodynamic effects the turbulent air flow and rocket engines [1]. The launching of the rocket, the air and engine phenomena can be seen in Figure 1.1 [2]. Ley and his colleagues propose the responses of the light and large structures may reach until 200-300 $g_{rms}$  which is a significantly highload for such light weight structures [26]. Since the launcher of the space program is not explicitly specified and contracted up to current point, the study and tests are performed by regarding the worst case of the possible options as will be explained in the related sections.

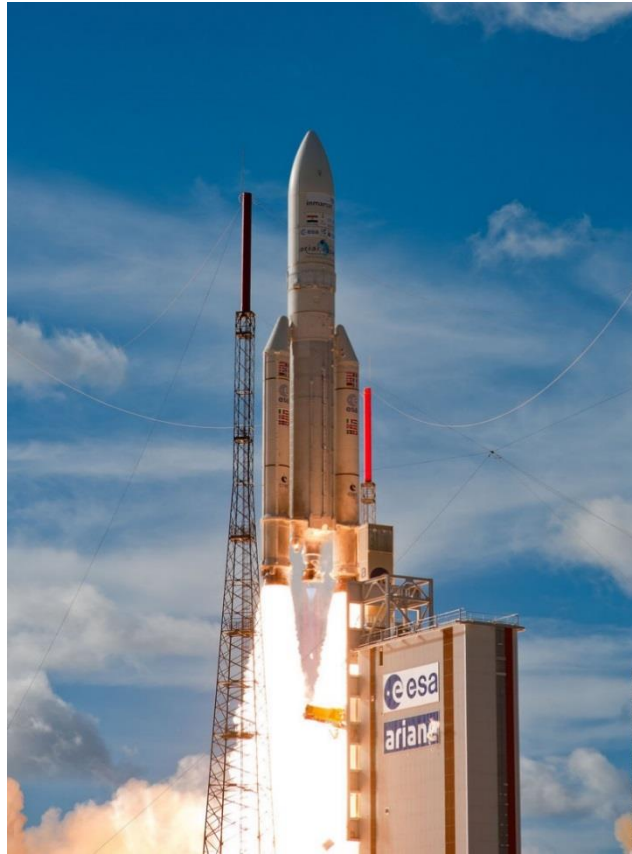


*Figure 1.1. Launching of Ariane 5 Spacecraft [2]*

Three conventional numerical methods which are Finite Element Method (FEM), Boundary Element Method (BEM) and Statistical Energy Approach (SEA) are conventionally used for vibro-acoustic numerical analyses. As Hambric et.al. states finite element method has been used since late 1970s for vibro-acoustic systems. Despite this method was used only for structural problems at its very early stages, they have transformed into a method for acoustic-structural coupled systems over the years [3]. Therefore, thanks to its accessibility, conventionally and traditionally usage, for numerical analysis of this thesis finite element method is focused. NASTRAN and ACTRAN packages used FEM are selected for performing modal/frequency response and vibro-acoustic analyses, respectively.

Consequently, in this thesis, the manufacturing processes of a large and lightweight reflector antenna made of carbon fiber reinforced composite is explained first, then

structural and acoustic tests will be compared with the structural and vibro-acoustic analysis.

## **1.2. Motivation of the Thesis**

The main motivation of this thesis is the extraordinary opportunity to study on an important space industry component for whole processes beginning from design, manufacturing to various vibration and acoustic tests. The dynamic and acoustic behavior of such complex composite space structures under different acoustic loading profiles is not a well-developed knowledge in our country. Before the components of the satellite is given permission for launch, standards require that they pass certain diffuse field acoustic loading tests in a reverberation chamber. These reverberation chambers are very large and such large volume reverberation chambers exist only in a handful of countries with a developed space industry. Therefore, each test in such reverberation chamber is very expensive. Due to cost and scheduling constraints, companies can perform these tests only towards the end of the project where design of each component is finalized. Learning that the antenna design fails the reverberation field tests at the end of the project timeline is an unacceptable risk for such large technical projects. Hence it is crucial that engineering team knows how the structural response will be to such diffuse field acoustic loading during design stage. Therefore, the main motivation and important outcome of this thesis is to obtain rather accurate numerical simulation capability for dynamic response of composite space structures under diffuse field acoustic loads.

This thesis tries to find the clear answer to the next questions:

- Is it possible to construct a numerical model to reflect the vibration, acoustic and vibro-acoustic test results?
- Does the thesis improve the literature with the composite antenna's test data?
- How close are the numerical and real test data?
- Are the models feasible in terms of numerical cost and solution time?
- What are the pros and cons of these models?

- If needed how can the design be improved so that engineering structure can endure such loads?

Over the thesis, the answer to above question will be investigated through numerical simulations.

### 1.3. Gregorian Type Configuration and Introduction of the Antenna

#### 1.3.1. Gregorian Type Antenna

J. Boshouwers and his colleagues defines the Gregorian type configuration as this type of antenna are consists of parabolic main reflector, sub-reflector, feed and support structures as given in the Figure 1.2 [4]. The parts of the feed are corrugated horn which provides the transmission and receiving of the radio frequency (RF) waves, duplexers and waveguides which provides the connection between feed and the satellite. The reflectors are shaped as crinkled surfaces, not regular parabolic ones, to obtain the exact field of view. The support structures may or not link the main and sub-reflectors. Hence, this complex structure provides an RF device which can be used in space like an antenna.

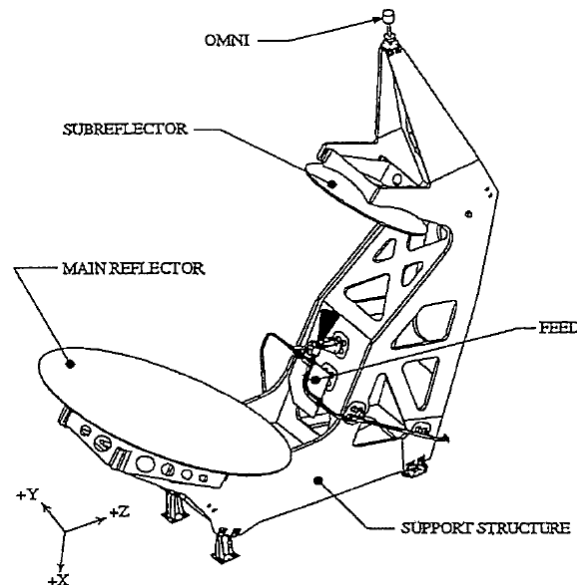


Figure 1.2. Gregorian Type Antenna [4]

### 1.3.2. The Antenna

The antenna is a Gregorian type antenna that has 3 main components Figure 1.3. In total, the antenna is constructed from 31 composite structures (2 reflectors, 29 ribs), 8 interface brackets, 1 feed chain (10 metallic parts), 10 feed brackets and various fasteners. First component is the main reflector whose diameter and mass are 1.6m and 8.5 kg, respectively. The support structure has 16 ribs to support the reflector and 4 titanium interface brackets. Tower assembly with 1.7m height is the second component of the antenna which holds the sub reflector whose diameter and mass are 0.6m and 1.1kg and feed chain. It is composed of sub-reflector, 13 structural composite ribs and 4 titanium interface brackets. The last component is the feed chain assembly which is the only metallic parts of the antenna except for the 8 interface brackets. The parts of the feed chain are horn, orthomode transducer (OMT), 2 diplexers, 4 waveguide runs and 13 brackets. All of the parts are displayed at the Figure 1.3.

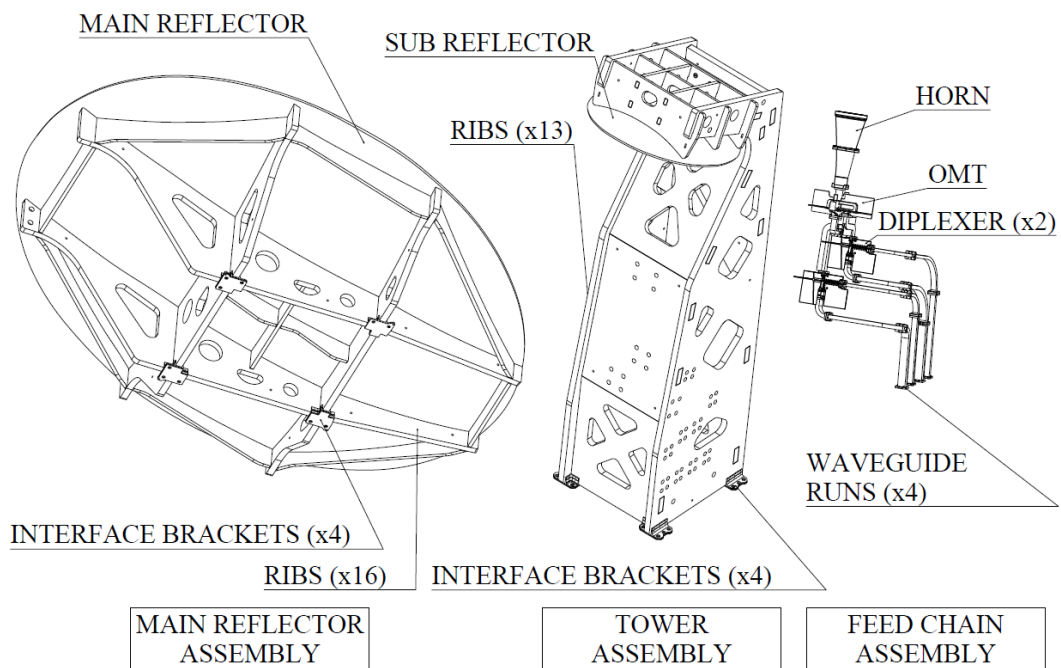


Figure 1.3. Principal Components of The Antenna

The main and sub reflectors and their ribs are composite sandwich structures. Since the space environment has high temperature difference, the thermal effects are

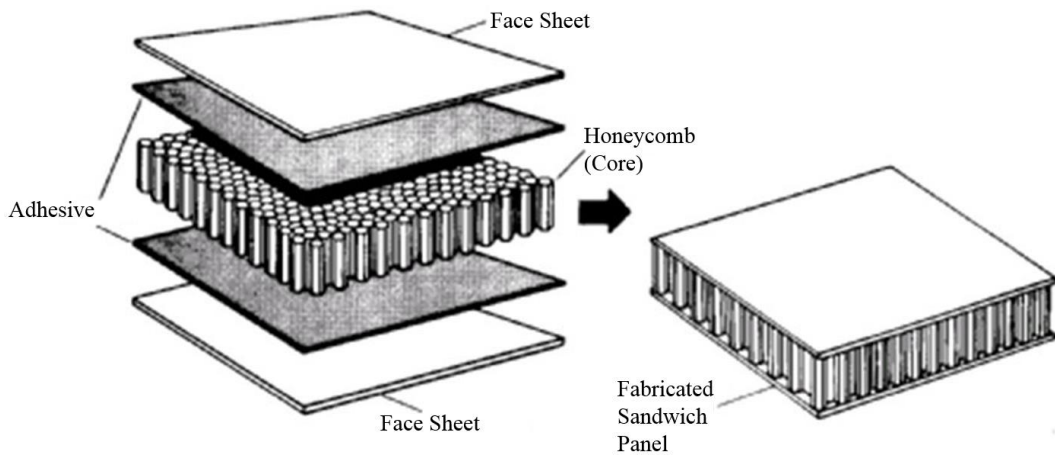
considered in the material selection. Especially, for the positional critical parts the materials with small thermal expansion coefficient are preferred during the design period. The considered materials and their thermal expansion coefficients are presented in the Table 1.1. Therefore, due to their small thermal expansion coefficient carbon-based materials are used for the composite structures and titanium (TI-6AL-4V) for the interface brackets. Moreover, horn and the 4 brackets at the very bottom of the waveguides are manufactured from titanium (TI-6AL-4V), as well. The other metallic parts and the brackets are machined by Aluminum (AL-6063-T5) due to its low density.

Table 1.1. *Thermal Expansion Coefficients [5,28]*

Material	Thermal Expansion Coefficient [ $10^{-6}(\frac{1}{K})$ ]
Carbon	1.1-1.3
Silicon	2.6-3.3
Epoxy-cast resin	45-65
Epoxy-glass fiber reinforced	36
Titanium	4.7-4.8
Aluminum (6063-T5)	21-24
Steel	11-12.5

### 1.3.2.1. Composite Structures of the Antenna

Sandwich structures offer light-weight and high strength, so they are preferred in space applications, commonly. Generally, sandwich structures are used where they (Figure 1.4) are composed of a core, face sheets (skin) and the adhesive used to bond the other two items. Each component of the sandwich structures has a different function. First of all, face sheets should be good at shear, tensile and compressive stresses, like honeycomb cores. Moreover, the honeycomb core should be resistant to buckling and crushing. In addition, the adhesive should be strong in terms of mechanical properties. Finally, all components should provide good sound attenuation [27]. Therefore, the components of the sandwich are selected in light of these criteria.



*Figure 1.4. Sandwich Structure [6]*

As it is mentioned before, carbon-based materials are used not only for the face sheet but also core. Cell size of the core fabricated from carbon is 3/8 inches while the density is 2.0 lbs/ft<sup>3</sup>. The face sheet is manufactured by curing 4 layers of carbon prepreg. The orientation of the layers is 0°/45°/−45°/0°. The last ingredient of the sandwich is the film adhesive. The adhesive is as critical as the core or face sheet since it sticks these two components to each other.

### **1.3.2.2. Metallic Parts of the Antenna**

Thirty metallic units are used in the antenna. Fourteen of these parts are made from titanium alloy which is Ti-6AL-4V also called as Ti-Grade5 and 16 of them are made from an aluminum alloy (AL-6063-T5 and AL-6061-T6), respectively. These parts are manufactured with tight tolerances in the light of the Turkish national standard in geometric dimensioning and tolerances [7] since all of the dimensions and tolerances become undoubtedly important at the assembly step. In the event of improper tolerances, components cannot be assembled. These brackets and items are manufactured by machining in the ‘Computer Numerical Control (CNC)’ machines and by brazing.

The mechanical properties of the used metals (TI-6AL-4V, AL-6063-T5 and AL-6061-T6) are listed in the Table 1.2. [8]

Table 1.2. *Mechanical Properties of Used Metals*

Material	Ultimate Strength (MPa)	Yield Strength (MPa)	Shear Strength (MPa)
TI-6AL-4V	895	825	545
AL-6063-T5	186	145	117
AL-6061-T6	275	240	185

### 1.3.2.3. Manufacturing Process

In this section manufacturing of composite parts whose mechanical details are given in section 1.3.2.1 and assembly processes will be presented. In the beginning, 3 sandwich panels whose dimensions are 2000mmX1000mmX20mm and 1 panel of 1000mmX1000mmX10mm are prepared to cure. Pre-cure conditions which is the temperature of 204 °C for 2 hours are applied to the preparation at the autoclave. The inserts are positioned with high precision and potted into the sandwich. The inserts are used for threaded fasteners, for example, the brackets of the feed chain are bolted through these inserts. Large sandwich panels are completed after curing the potting of the inserts. In the next step of obtaining the sandwich panels, those are split up into their final shapes and 29 parts are obtained (Figure 1.5).



*Figure 1.5. Machining of Sandwich Panels*

Then, the composite parts are gathered together by using an assembly fixture. Each composite structure is connected to its neighbor part directly or by using small L-cleats which are also made from CFRP. This procedure is shown in Figure 1.6.



*Figure 1.6. Composite Assembly and Sticking Processes*

Like attachment of composites, the interface brackets are also glued to the composite structure by using proper adhesive. This process is performed by using the sensitive pins and assembly fixtures, too. At the final step, the tower and main-reflector sub-assemblies are embodied (Figure 1.7).

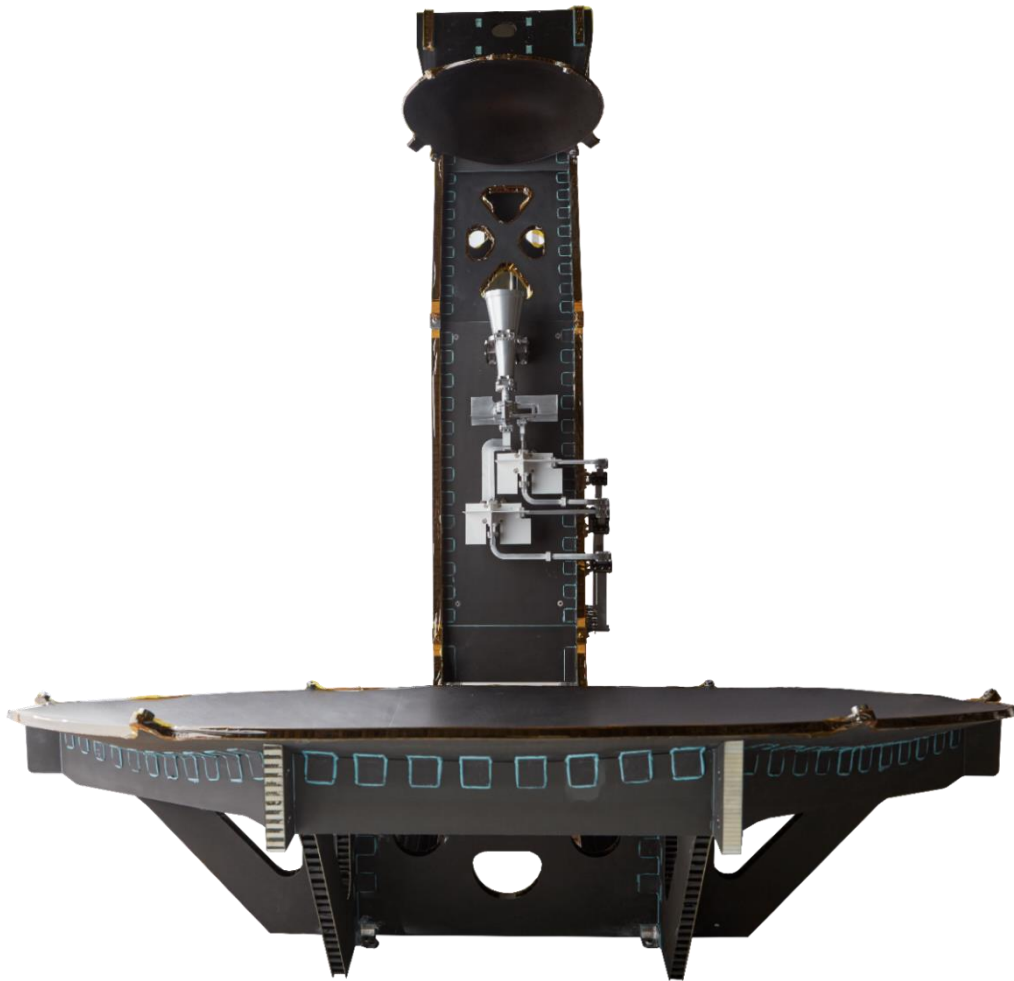


*Figure 1.7. Tower and Main Reflector Sub-Assemblies*

#### **1.4. Vibro-Acoustic Test**

The American and European space authorities which are National Aeronautics and Space Administration (NASA) and European Cooperation for Space Standardization (ECSS) that is supported by European Space Agency (ESA) put the requirements related to vibro-acoustics for the payloads. According to these standards, the light structures with large areas such as solar arrays, reflector antennas, etc. are susceptible

to acoustic loading. Therefore, NASA-STD-7001B and ECSS-E-ST-10-03C clarifies these vibro-acoustic requirements [9,10].

In space applications, generally the structure is tested at two levels which are qualification and flight acceptance levels. These levels symbolize the sound pressure level over the frequency band. Flight acceptance level is determined by the launcher as the maximum sound pressures for each frequency band that is called “Maximum Expected Flight Level (MEFL)” by NASA [9]. Qualification level is obtained by adding 3dB for each flight acceptance level [9,18]. The test durations of flight acceptance level and qualification levels are 1 minute and 2 minutes, respectively. Table 1.3 summarizes the critical vibro-acoustic aspects of both standards.

Table 1.3. Summary of Vibro-Acoustic Testing

Test Name	Level	Duration (minutes)
Flight Acceptance Test	MEFL	1
Qualification Test	MEFL+3dB	2

The tests are made at the reverberant acoustic chambers to get homogenous sound pressure levels over the acoustic room. [11] Faby explains the diffuse sound field concept as “*the central concept is that of a sound field consisting of a very large set of statistically unrelated (uncorrelated) elemental plane waves of which the propagation direction is random with a uniform probability distribution.*”. The schematic reflects this phenomenon in Figure 1.8 [12]. Stavrinidis also takes attention to the diffuse field as acoustic waves with the same energy in all directions with a random attitude [13]. As Pierce proves the diffuse field as a superposition of the plane waves the following formulation ( 1 ), Sikström presents the formula yielding the diffuse sound field by summation of all these plane waves at a specific frequency [12,14].

$$\hat{p} = \sum_q \hat{p}_q e^{ik\bar{n}_q \bar{x}} \quad (1)$$

where  $\hat{p}$  is the resultant acoustic pressure,  $\hat{p}_q$  is the pressure carried by each plane wave,  $k$  is the wave number ( $k = 2\pi/\lambda$ ),  $\hat{n}_q$  is the normal directions of each plane wave.

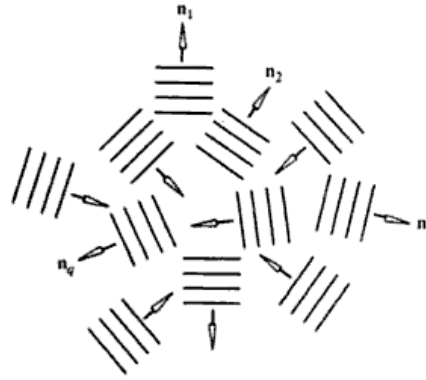


Figure 1.8. Schematic of the Diffuse Sound Field [12]

The book of “*Foundation of Vibroacoustics*” also lists the criteria of the reverberant chambers to obtain diffuse sound field as [11]:

- Reverberant chambers have to be very large with similar edge lengths,
- All of the surfaces of the chambers should have comparable sound absorption coefficients,
- Scattering property of the reverberant chambers’ surfaces have to be high,
- The chambers should contain more than one acoustic sources such as horns or loudspeakers.

The ratio of the reverberant chamber over the test specimen has to be larger than 10. The sound pressure levels have to be controlled minimum 4 microphones in the reverberant chambers according to NASA-STD-7001B [9]. The microphones should be positioned for the minimum effects of the test specimen surfaces. In order to prove the uniformity of the reverberant chamber the tolerances of the sound pressure level for each of microphones have to be satisfied. The test is accepted as successful if the SPL values are between the upper and lower tolerance limit which is determined by ECSS [10] and shown in Table 1.4 for each octave band level.

Table 1.4. *Sound Pressure Level Tolerance Limits for Octave Band* [10]

Octave Band Centre Frequency (Hz)	<i>Lower Tolerance Limit (dB)</i>	<i>Upper Tolerance Limit (dB)</i>
31.5	-2	+4
63	-1	+3
125	-1	+3
250	-1	+3
500	-1	+3
1000	-1	+3
2000	-1	+3
Overall (OASPL)	-1	+3

Since the vibro-acoustic tests can be destructive for the reflector antennas the structural effects of the acoustic loads on the specimen have to be examined for any defects, cracks, or so on. In order to characterize these kinds of structural damage, ECSS offers a low level which is 8dB lower from the qualification level acoustic test phenomena. As stated in [15], two low level tests should be tasked just before and after the qualification level which is the harshest acoustic condition of the test series.

*“The success criteria for the resonance search shall be:*

- 1. less than 5 % in frequency shift, for modes with an effective mass greater than 10 %;*
- 2. less than 20 % in amplitude shift, for modes with an effective mass greater than 10 %.”* [15],

Another option addition to low level acoustic tests is the resonance sweep tests. The same comparison might be made preceding and succeeding qualification level acoustic tests. To sum up, if the differences at the frequencies with large effective mass are small enough in both low level vibro-acoustic tests and resonance sweep tests, structure passes the acoustic test successfully.

## 1.5. Literature Review

This section presents the literature survey from different space agencies' studies, some books and article. Firstly, different numerical techniques like FEM, BEM and SEA are compared. Secondly, previous studies including vibro-acoustic analysis and their comparisons with test data and the difficulties of this phenomena will be illustrated. Moreover, some guidance about acoustic testing will be presented.

Almost all of the authors of vibro-acoustic studies have a common opinion that the acoustic loads resulted from engines of the rocket and aerodynamic effects during the launch is highly destructive for the large and light structures [1, 12, 17, 26, 27, 36]. As it is mentioned before, there are three conventional numerical methods for vibro-acoustic problems which are Finite Element Method (FEM), Boundary Element Method (BEM) and Statistical Energy Method (SEA). The selection of which method should be used is dependent on different aspects such as accessibility to resources, solution accuracy at different frequencies, affordability of the solver software, required computational time. Each method has its own advantage and disadvantages. First of all, FEM is advantageous because of the existence of various sources and accessibility of software; on the other hand, this method is computationally expensive because of the requirement of meshing and low precision at high frequencies. Vibro-acoustic analysis with FEM gives results with high precision at low frequency analysis since it performs mode-by-mode analysis [1]. Secondly, BEM proposes medium level advantages in terms of accessibility of sources and software, computational time while it is good at accurate results at low frequencies and weak for high frequency accuracy. The final method, SEA, is a very specific statistical method to make precise vibro-acoustic analysis at high frequency ranges; however its usage and sources are limited. Siktröm compares these three methods in his thesis, and the comparison summary provided by him and general information is presented in Table 1.5 [12] where each ‘\*’ represents the success of the method for the corresponding aspect.

Table 1.5. Comparisons of FEM, BEM and SEA[12]

Property	FEM	BEM	SEA
Usage Frequency/Accessibility to sources	***	**	*
Accessibility/Price of Software	***	**	*
Required Computational Time	*	**	***
Accuracy at Low Frequencies	***	***	**
Accuracy at High Frequencies	*	*	***

Determining the boundaries of the frequency range may change from case to case. 300Hz is generally accepted as a threshold for the determination of the low/high frequency ranges in vibro-acoustic analysis (for air). The range smaller than 300Hz is accepted as low-frequency range, while high-frequency range considers the frequencies larger than 300Hz [1,12].

Ullio and Maruchi perform both FEM and SEA analysis of The Gravity Field and Steady-State Ocean Circulation Explorer (GOCE) by ESA in their article named as “*Goce Satellite Vibro-Acoustic Performance Predictions Using Alenia Integrated FEM&SEA Approach*”[1]. The FEM and SEA analyses are performed up to 300Hz and 4000Hz in the MSC. NASTRAN and AutoSEA2, respectively. They concluded their studies as although the results of FEM and SEA are close to each other at their overlapping regions, both FEM and SEA underestimates the results compared to test in related regions [1]. Figure 1.10 summarizes their studies. Although their study shows that FEM results may be acceptable at the only mid-frequency range while the SEA results reflect only the behavior of the response curve, they conclude that both of the FEM and SEA results are far from the test data, unfortunately.

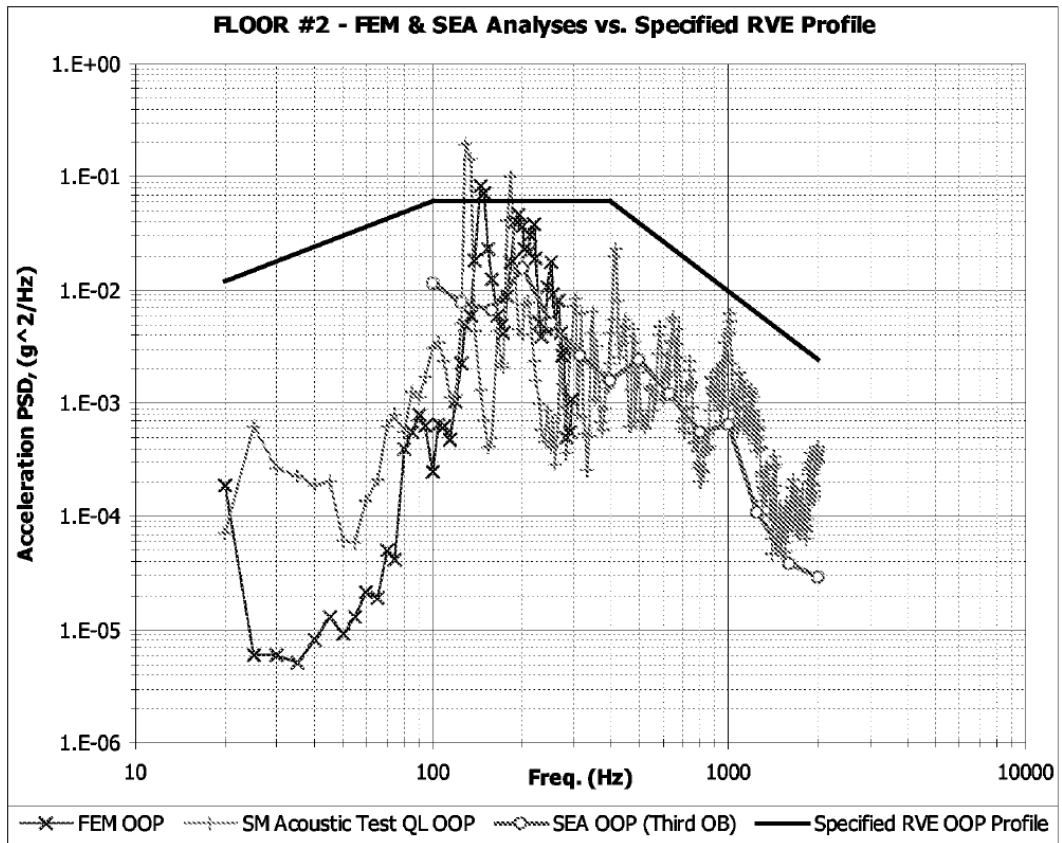


Figure 1.9. Comparison of FEM and SEA results with test data [1]

Secondly, Sikström [12] investigated the performance of FEM vibro-acoustic analysis between 20-300Hz and compared it with BEM results and funded by ESA's project, "In-Flight Thermo-Elastic Stability Improvement of Carbon Reflector". The focused reflector's diameter is 2.4m, mass is 11.72kg. He uses a specific technique called as 'split loading' by dividing the reflector into 32 or 42 patches then compares these FEM results with BEM result and the test results, as illustrated in Figure 1.10. As a result of this study, FEM results (red and pink curves) are larger at low frequencies while smaller at higher frequencies compared to test data (blue curve). Both of the FEM and BEM results have an only agreement about the locations of the peak, nearly, the maximum values of those curves cannot be satisfied. In contrast to these, the analysis results of this study can be accepted as close to the test data in terms of root mean square (rms) values.

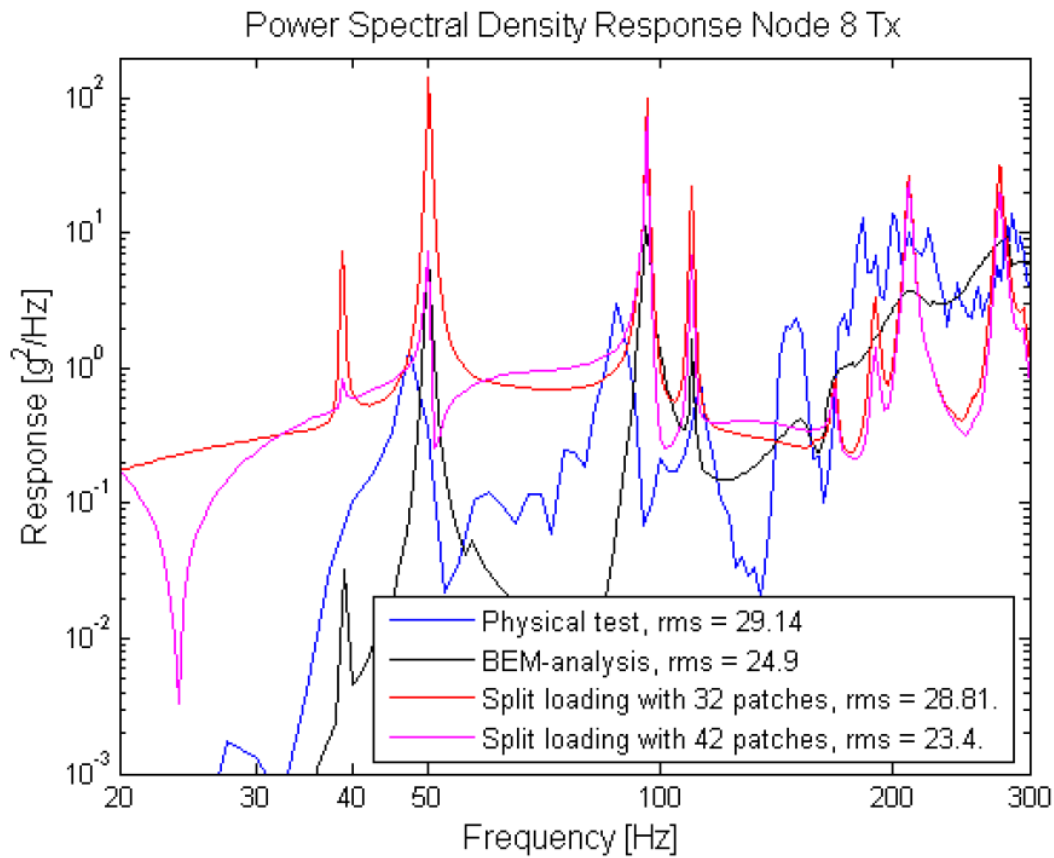


Figure 1.10. Comparison FEM, BEM and test results [12]

Wickramasinghe and his colleagues also propose vibro-acoustic FEM analysis responses (up to 250Hz) of the CASSOPE satellite's proto-flight model and compare these analysis results with test data performed in reverberant chamber [17]. Figure 1.11 shows their structural response results for two different accelerometers [17]. This study is much more successful than the previous ones since it reflects the similar behaviors of the test and analysis results. However, generally their FEM results underestimate the test. Although it is accepted as FEM is good at the low frequencies, the figure illustrates that this case is not commonly satisfied with their valuable study.

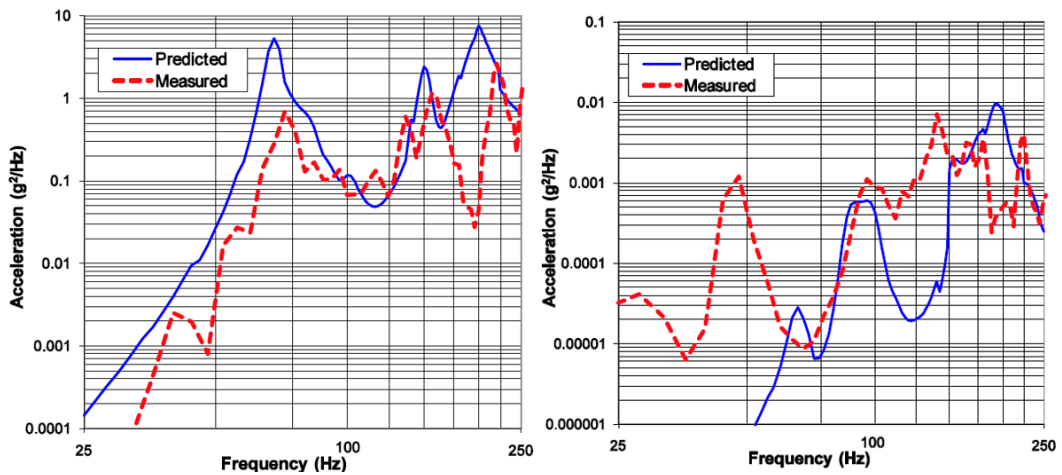


Figure 1.11. Predicted (FEM) and Measured (Test) Comparisons at Different Locations [17]

Additionally, two main acoustic test techniques exist for space structures. These techniques are Direct Field Acoustic Testing (DFAT) where the acoustic loads sourced by speakers or horns are directly applied to the test specimen and Reverberant Field Acoustic Testing (RFAT) [36]. In contrast to DFAT, RFAT requires reverberant chambers whose walls are highly reflective in order to obtain a homogenous sound pressure level in it. Marshall presents a comparison of a BEM analysis with random vibration results of the DFAT test for a spacecraft in his thesis titled as “*Acoustic Analysis of Spacecraft Cavities using the Boundary Element Method*” [36]. In the study, the structural responses of the spacecraft walls made of the composite are measured. The comparisons are provided in Figure 1.12. Although there are some studies about DFAT, RFAT is a more commonly used method. This thesis focuses on the acoustic tests performed in the reverberant chambers.

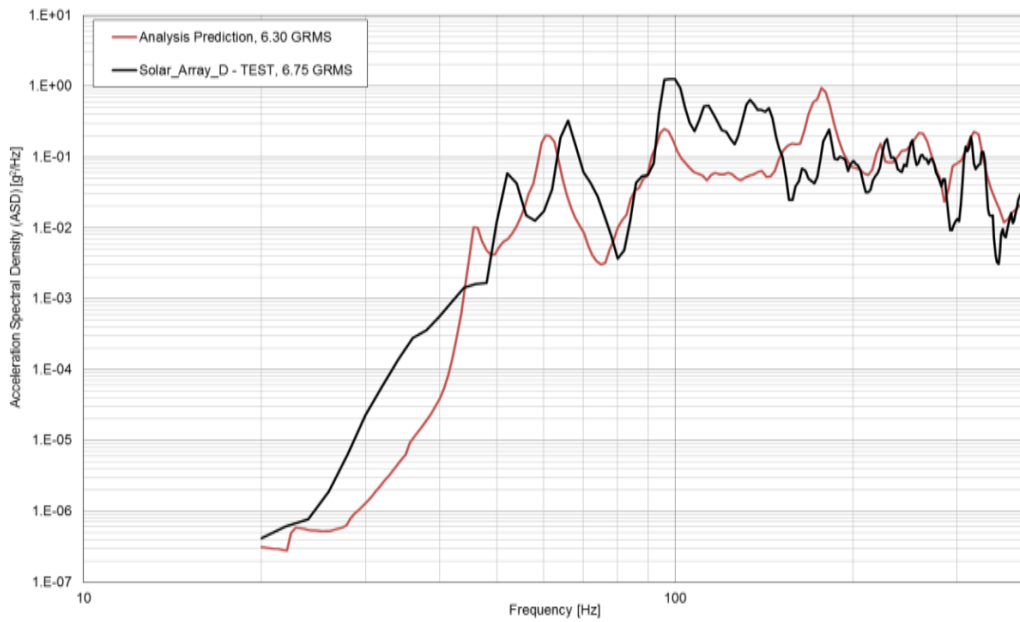


Figure 1.12. Comparison of Acoustic Test vs. BEM Analysis [36]

It can be concluded from these studies that matching vibro-acoustic analysis results with test data has difficulties. At this point, Cotoni offers a FEM-SEA hybrid method that FEM should be used at low frequencies or structures with fewer mode shapes, while SEA should be used for the vice versa [32]. The studies found from the literature show that there are some issues with the accuracy of the numerical prediction throughout the whole frequency range. It is observed from studies that determination of the amplitude at the resonant frequencies seems to be more difficult than determining the locations of the resonance peaks, possibly due to the complex nature of damping in the composite structures.

To sum up, the literature presents various precious vibro-acoustic studies including different analysis techniques such as FEM, BEM or SEA and different tests which are direct and reverberant field acoustic tests. Although each of these techniques has individual advantages, it is commonly referred that the comparisons of the test and analysis results have challenges and matching the response for a wide frequency range is a difficult task.

## 1.6. Simulation Approach used in Numerical Analysis

The calculations and simulations performed throughout this thesis are performed by using NASTRAN software for structural analyses and ACTRAN for vibro-acoustic analyses. For completeness, essential high-level formulations and relations which describe the fundamentals of the methodology used by the numerical simulation software will be given in this section. Since no contributions to the theoretical approach are aimed in this thesis, only limited and fundamental equations are provided. Specifically, it is aimed to explain with a low amount detail how structural-acoustic coupling is performed and how is the modeling of composite structures is handled in the simulation tools used in this study.

The governing equations, which are the structural equation of motion ( 2 ), homogenous Helmholtz equation ( 3 ) and the vibro-acoustic coupling relation ( 4 ) are presented below. Nastran and Actran use these general governing equations and some details will be given in the next sections.

$$\text{Structure:} \quad [-\omega^2[M] + i\omega[D] + [K]]\{x_o\{\omega\}\} = \{F_p(\omega)\} \quad (2)$$

$$\text{Acoustic:} \quad \nabla^2 p + k^2 p = 0 \quad (3)$$

$$\begin{array}{l} \text{Vibro-} \\ \text{Acoustic:} \\ \text{Coupling} \end{array} \quad \begin{bmatrix} K_s + i\omega D_s - \omega^2 M_s & C \\ \omega^2 C^T & K_a + i\omega D_a - \omega^2 M_a \end{bmatrix} \begin{Bmatrix} u(\omega) \\ p(\omega) \end{Bmatrix} = \begin{Bmatrix} f_s(\omega) \\ f_a(\omega) \end{Bmatrix} \quad (4)$$

The terms of the equation ( 2 ) are summarized as [M], [D] and [K] are the mass, damping and stiffness matrices of the structure, respectively.  $\{F_p\}$  is the applied load to the system in the vector form. Under these conditions the response of the structure denoted by 'x' in harmonic solution and  $\omega$  is the excitation frequency. For the equation ( 3 ),  $p$  denotes the sound pressure and  $\nabla$  and  $q$  symbolizes the gradient operator and volume source flow and  $k$  is the wave number. The terminologies of the equation ( 4 ) are summarized as, the subscripts 's' and 'a' symbolize structural and

acoustic domains, respectively. K, D and M are the stiffness, damping and mass matrices. C is the acoustic-structure coupling matrix. ‘u’ and ‘p’ are the structure’s displacement and fluid’s pressure, respectively. ‘f’ shows the external/excitation load of structure or acoustic.

### 1.6.1. Fundamental Composite Material Modelling in Nastran

First of all, for the structural part of the thesis, the total response of the multi-degree of freedom (MDOF) systems are calculated by the following governing equation as it is included in the “*Engineering Vibroacoustic Analysis*” book [3] and Nastran uses equation ( 2 ) in the structural calculations. In the equation, [M], [D] and [K] are the mass, damping and stiffness matrices of the structure, respectively.  $\{F_p\}$  and  $\omega$  are the applied load to the system in the vector form and circular natural frequency.

Moreover the theories related to composites are introduced. The modeling of composite material is not commonly used because of its specific field of use. Although in the literature, there are some methods which construct the equivalent material properties, they may not be able to reflect the dynamic behavior of composite structures completely. NASTRAN qualified by NASA is able to model such layered materials.

Composite materials are anisotropic materials not isotropic because of their layers such as face sheets, cores and adhesives. [3] and [25] offer some governing equations related to anisotropic materials. Stress-strain relationship of those materials are given as

$$\begin{Bmatrix} \sigma_x \\ \sigma_y \\ \sigma_z \\ \tau_{xy} \\ \tau_{yz} \\ \tau_{xz} \end{Bmatrix} = \begin{bmatrix} G_{11} & G_{12} & G_{13} & G_{14} & G_{15} & G_{16} \\ G_{21} & G_{22} & G_{23} & G_{24} & G_{25} & G_{26} \\ G_{31} & G_{32} & G_{33} & G_{34} & G_{35} & G_{36} \\ G_{41} & G_{42} & G_{43} & G_{44} & G_{45} & G_{46} \\ G_{51} & G_{52} & G_{53} & G_{54} & G_{55} & G_{56} \\ G_{61} & G_{62} & G_{63} & G_{64} & G_{65} & G_{66} \end{bmatrix} \begin{Bmatrix} \varepsilon_x \\ \varepsilon_y \\ \varepsilon_z \\ \gamma_{xy} \\ \gamma_{yz} \\ \gamma_{xz} \end{Bmatrix} - (T - T_{ref}) \begin{Bmatrix} A_1 \\ A_2 \\ A_3 \\ A_4 \\ A_5 \\ A_6 \end{Bmatrix} \quad (5)$$

where  $\sigma$ ,  $\tau$ ,  $G$ ,  $\varepsilon$ ,  $\gamma$ ,  $T$  and  $A$  are stress, shear stress, shear modulus, strain, shear strain, temperature and thermal expansion coefficient, respectively.

MSC NASTRAN derives transverse shear stress, bending stress, membrane stress and their couplings as one solution for the laminated materials by using the material properties derived by the user. Since all the tests and analysis are performed in the reference temperature, the thermal effects are ignored. NASTRAN uses “Classical Lamination Theory” and “Transverse Shear Theory” at calculations for the composite materials [25].

### **1.6.2. Fundamentals of Diffuse Acoustic Field Generation in Actran**

In the acoustic parts of the thesis, the general wave equation is applied by Actran. The governing homogenous Helmholtz equation is presented via the equation ( 3 ) where  $k = \omega/c_0$ . In the formulation  $k$  is the wave number,  $c_0$  is the speed of sound at air (340 m/s) and  $\rho_0$  is the density of air as  $1.225 \text{ kg/m}^3$  at the room temperature [3], [44].

Both of the vibro-acoustic tests and analyses are performed under the diffuse sound field conditions. The reverberation chambers are typically used for obtaining diffuse sound fields. This study’s tests are also performed in the reverberation chamber as the details will be mentioned in the related sections. The explanation of the diffuse field by The Institute of Noise Control Engineering (INCE-USA) is given in the ACTRAN user guide as “*sound field in which the time average of the mean-square sound pressure is everywhere the same and the flow of acoustic energy in all directions is equally probable*” [44]. All of the formulations related to diffuse field are referenced from the section of “*Diffuse Incident Pressure Field*” at the ACTRAN user guide [44]. The diffuse sound field is symbolized as  $p_n(\mathbf{r}, t)$  where  $\mathbf{r} = (r, \theta, \phi)$  is the position of the vector corresponding to calculated point and  $t$  is the time. The subscript  $n$  shows the plane wave index. For any particular plane wave specific pressure calculated at the origin is expressed as  $x_n(t)$  and given by ( 6 ). In order to show this, two points ( $\xi_1$  and

$\xi_2$ ) are chosen. The critical issue is that it is accepted as  $\xi_1$  is the origin while  $\xi_2$  is at the location of  $(r,0,0)$ .

$$x_n(t) = p_n(0, t) \quad (6)$$

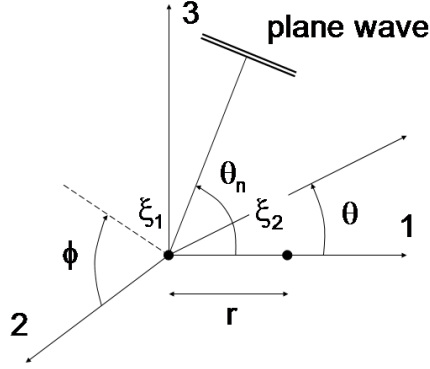


Figure 1.13. Particular Plane Wave and Corresponding Coordinate System

If the pressure at a point with distance  $r$  at any time along the axis 1, the spatial domain has to be transformed into the time domain as:

$$p_n(r, t) = p_n\left(0, t - \frac{r}{c} \cos\theta_n\right) = x_n\left(t - \frac{r}{c} \cos\theta_n\right) \quad (7)$$

For the diffuse field, it is assumed that there are infinitely many plane waves. Thus, the number of plane waves,  $N$  goes to infinity ( $N \rightarrow \infty$ ). Moreover, the diffuse field along direction 1 is calculated by summing the pressures of each individual plane wave:

$$p(r, t) = \lim_{N \rightarrow \infty} \frac{1}{\sqrt{N}} \sum_{n=1}^N p_n(r, t) = \lim_{N \rightarrow \infty} \frac{1}{\sqrt{N}} \sum_{n=1}^N x_n\left(t - \frac{r}{c} \cos\theta_n\right) \quad (8)$$

Therefore, the sound pressure inside the diffuse sound field simulating the reverberation chamber is modeled by ( 8 ).

### 1.6.3. Fundamentals of Acoustic Structural Coupled Analysis in Actran

Vibro-acoustic coupling presented via the equation ( 4 ) is succeeded by impedance coupling method. Incompatible vibro-acoustic coupling method which couples the nodes inside a threshold value which is 5mm of ACTRAN is used for this coupling. ACTRAN User Guide formulates the vibro-acoustic formulation [44]. There are 3 main assumptions for this calculation:

- The structure has to be made elastic material,
- The fluid has to be acoustic material,
- The displacements of the structures have to be small.

The main aim of this coupled system is to obtain  $u(\omega)$  and  $p(\omega)$  since they are unknowns. Equation ( 4 ) can be simplified by the change of variables of ‘Structural Dynamic Stiffness Matrix’,  $A_s(\omega)$  and ‘Acoustic Dynamic Stiffness Matrix’,  $A_a(\omega)$ .

$$A_s(\omega) = K_s + i\omega D_s - \omega^2 M_s \quad (9)$$

$$A_a(\omega) = K_a + i\omega D_a - \omega^2 M_a \quad (10)$$

In addition to new structural and acoustic dynamic stiffness matrix definitions, the acoustic unknown pressure,  $p(\omega)$ , is separated into two sub-vectors which are the fluid’s pressure for the coupled nodes ‘ $p^c(\omega)$ ’ and uncoupled nodes ‘ $p^u(\omega)$ ’. If all of these formulas are combined together, the following matrix system occurs:

$$\begin{bmatrix} A_s(\omega) & C & 0 \\ \omega^2 C^T & A_a^{cc}(\omega) & A_a^{cu}(\omega) \\ 0 & A_a^{uc}(\omega) & A_a^{uu}(\omega) \end{bmatrix} \begin{pmatrix} u(\omega) \\ p^c(\omega) \\ p^u(\omega) \end{pmatrix} = \begin{pmatrix} f_s(\omega) \\ f_a^c(\omega) \\ f_a^u(\omega) \end{pmatrix} \quad (11)$$

In the formulation the superscripts ‘u’ and ‘c’ symbolizes ‘uncoupled’ and ‘coupled’ nodes of the system.

The coupled solution is performed by projecting the structural equation set ( 11 ) onto the subspace of the first  $m_s$  structural modes. The generalized modal coordinates are denoted by  $\underline{q}^s(\omega)$  and the relation between the modal response (u) and generalized modal coordinates is given as:

$$u(\omega) \sim \underline{u}^s(\omega) = \psi^s \underline{q}^s(\omega) \quad (12)$$

Where  $\psi^s = [\psi_1^s, \psi_2^s, \dots, \psi_{m_s}^s]$  is the combined matrix of the first  $m_s$  structural modes. If the ( 12 ) and orthogonality conditions are applied to the ( 11 ) the following matrix system is obtained:

$$\begin{bmatrix} \underline{A}_s(\omega) & \underline{C} & 0 \\ \omega^2 \underline{C}^T & A_a^{cc}(\omega) & A_a^{cu}(\omega) \\ 0 & A_a^{uc}(\omega) & A_a^{uu}(\omega) \end{bmatrix} \begin{pmatrix} \underline{q}^s(\omega) \\ p^c(\omega) \\ p^u(\omega) \end{pmatrix} = \begin{pmatrix} \underline{f}_s(\omega) \\ f_a^c(\omega) \\ f_a^u(\omega) \end{pmatrix} \quad (13)$$

Where the diagonal modal stiffness and mass matrices are considered

$$\underline{A}_s(\omega) = \psi^{sT} A_s(\omega) \psi^s = \underline{K}_s + i\omega \underline{A}_s - \omega^2 M_s \quad (14)$$

$$\underline{C} = \psi^{sT} C \quad (15)$$

$$\underline{f}^s = \psi^{sT} f_s(\omega) \quad (16)$$

To sum up, Actran uses the equation ( 13 ) for the vibro-acoustic calculations.

## 1.7. Outline of the Thesis

In this part, the thesis is outlined chapter by chapter. Background information about the space applications and the motivation, scope and aim of the thesis are presented in the sections 1.1 and 1.2, respectively. Then, section 1.3 describes the Gregorian antenna types and considered antenna not only geometry but also materials and manufacturing details. Section 1.4 introduces the standards and approaches of the vibro-acoustic tests. In addition to these, in the Section 1.5, literature review including similar studies to this thesis is presented and some of the studies are summarized. Section 1.6 also proposes some important formulations that the software packages use.

The following chapter presents the vibration aspects of the thesis such as the sine sweep test, frequency response and modal analyses and comparison of tests and FEM analysis results, respectively. Section 2.1 offers information about vibration test. Section 2.1.1 expresses the background information about the test such as

accelerometers and their locations on the antenna, features of the shaker, data acquisition system, etc. This chapter is concluded by giving the frequency sweep test results and results in the Section 2.1.3. The FEM details such as material cards, grid and elements, stiffness values so on will be introduced in the Section 2.2.1 then the modal analysis and frequency response analysis with their elements and results will be proposed in Section 2.2.2 and Section 2.2.3, respectively.

Another important part of the thesis related to vibro-acoustic response is in the Chapter 3. In this chapter, the acoustic tests will be stated in the Section 3.1. The details about the test set-up, reverberant test chamber, accelerometers and data acquisition system are provided in Section 3.1.1. Section 3.1.2 and 3.1.3 include the acoustic tests without and with the antenna, respectively. At the final section of this chapter comparisons between the test and FEM analysis results will be given.

The thesis is concluded by the Conclusion and Future Work (Chapter 4).



## CHAPTER 2

### VIBRATION TESTS AND FEM ANALYSIS OF THE ANTENNA

#### 2.1. Sine Sweep Test of the Antenna

In this section, the preparation, details and results of the antenna's sine sweep test will be presented. Firstly, after the background information about the vibration tests, the details of the used test set-up, accelerometers and data acquisition systems will be introduced. Although the first option to determine the natural frequencies and mode shapes of any structure is modal (hammer) tests, in this thesis modal tests are not performed. The existing modal test setup is not suitable for such tower or main reflector structures because of the dimension limitations. Additionally, for the composite structures with geometrical and structural complexities the modal tests may be difficult to implement. Then, the options to obtain the natural frequencies and mode shapes are searched. Sarafin and his friends also defend that the sine sweep tests with low excitation would be helpful to determine natural frequencies, mode shapes and damping ratios [22]. Furthermore, Ley, Wittmann and Hallmann also suggests the low level sine vibration tests to update the finite element model [26]. Therefore, in this thesis, sine sweep tests are used to determine the natural frequencies of the tower and main reflector sub-assemblies of the antenna, instead of modal tests.

##### 2.1.1. Background Information about the Vibration Test

In order to extract the natural frequencies of the structures resonance sweep which is also called sine sweep vibration tests are performed. The tests are done in the  $-x$  and  $-y$  directions of the coordinate system of the antenna which is given in the Figure 2.1. Because of lack of the head expander which is a kind of a converter used to change the axis of the test, the vibration tests could not be performed in the  $z$ -axis.

In literature, sine sweep tests are regularly used for different purposes such as especially comparison of the two different cases, determining natural frequencies, simulations of earthquakes, so on [19,20,21]. In their paper, Haiyang uses sine sweep test to present the effect of a crack on a structure similar to a satellite with excitation level of 0.1g [19]. As it is seen from Haiyang's study, the input acceleration levels should be small in order not to damage the structure and be large enough to obtain the structural response. As Sarafin suggests that input amount of 0.25g would be proper for the structures weighs between 25kg and 250kg [22]. Thus, the input excitation is chosen as 0.25g for sine sweep test sequence while the mass is about 33kg.

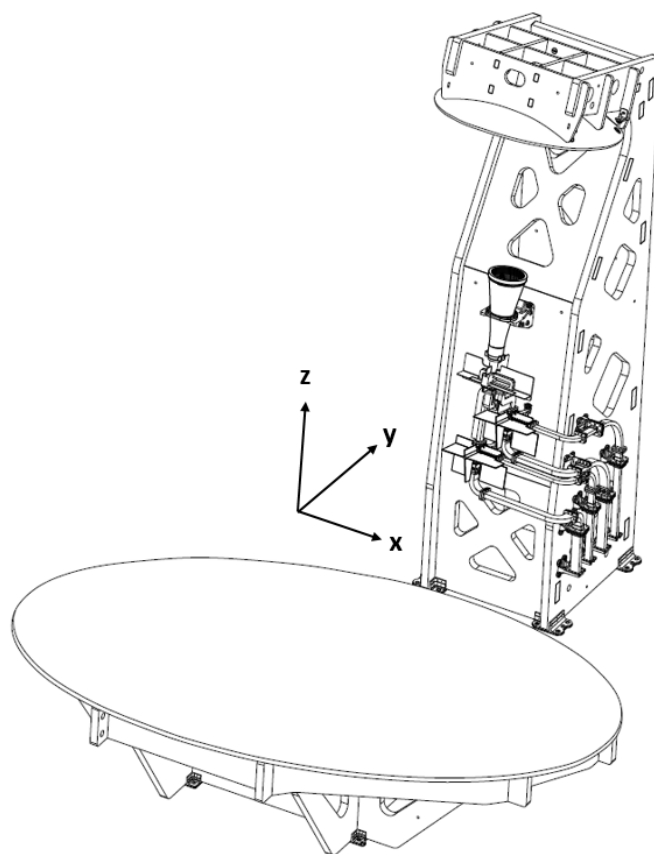


Figure 2.1. Coordinate System of the the Antenna

### 2.1.2. Vibration Test Set-Up

The vibration tests are performed by using the shaker at the REHİS, ASELSAN. The shaker is LDS V-9. The shaker is capable of the vibration tests until 1000 kg of test specimens. The test sequence consisted of 4 separate tests which are tower in  $-x$  axis, main reflector in  $-x$  axis, tower in  $y$ -axis and main reflector in  $-y$  axis. The reason for the frequency range which is up to 2,000Hz selection is related to vibro-acoustic analysis. Doubling of the frequency range interest of vibro-acoustic analysis which is up to 750Hz is necessary for vibration test. By this doubling, the first half of the vibration test proposes proper results by the rule of thumb; in other words the results up to 1000Hz require determining the response up to 2000Hz [22].

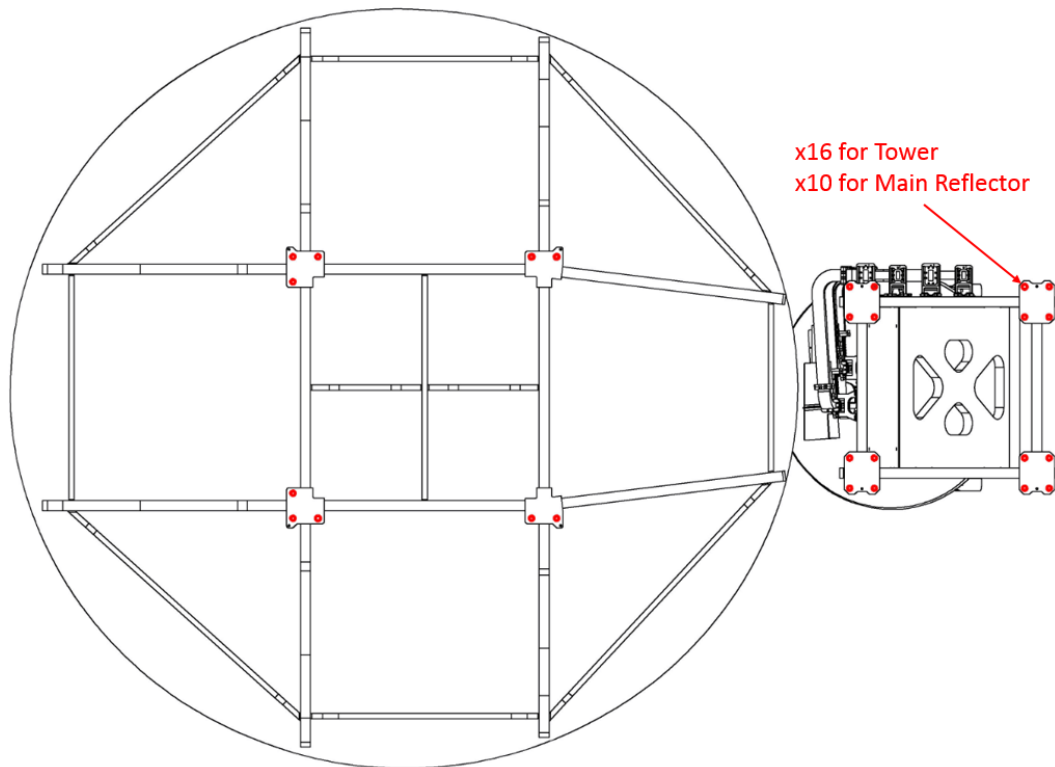


Figure 2.2. Mounting Holes of the Antenna

The antenna connections to the satellite or fixture for the tests are shown in Figure 2.2. There are 16 mounting holes for the tower while 10 for the main reflector

subassemblies. M6 A4 stainless steel bolts with 6.2mm hole diameters are used. The bolts are torqued with 9 Nm as it is specified in the standard [24].

The accelerometers used in the tests were calibrated and certified ones. 4 accelerometers are used on the tower where 2 of them take along 2-axis while the other two take data along a single axis. Similarly, 3 of 4 accelerometers on the main reflector which are positioned on the periphery of it are used as single axis (only normal direction) while one of them which is in the middle of the reflector was a tri-axial accelerometer. The accelerometer positions and naming that “t”, “sr” and “mr” symbolizes tower, sub reflector and main reflector are shown in the Figure 2.3. In addition to these accelerometers, one additional of it is placed on the test fixture in order to measure the input excitation. If the excitation resulted by shaker exceeds or falls behind the upper and lower limits, the data comes from these control accelerometers stops the shaker and test.

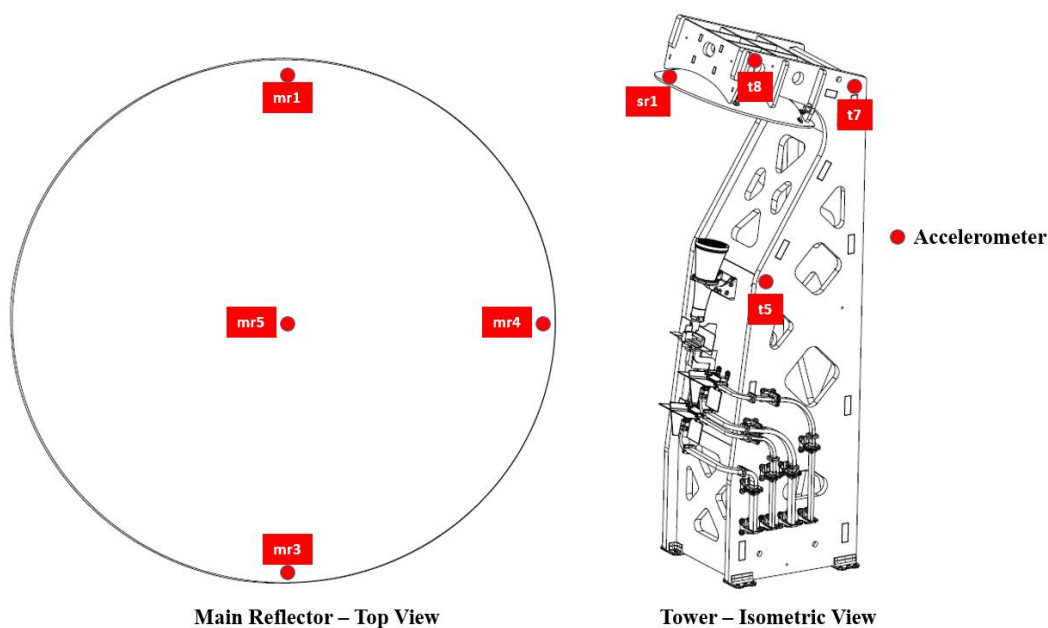


Figure 2.3. Accelerometer Positions of the Vibration Test

Lack of data channel on the acquisition system limits the tests into only 7 accelerometer usage. Previous modal analysis results helped us the placement of these accelerometers since the positions are so critical in order to obtain most of the mode

shapes. Although 8<sup>th</sup> accelerometers were placed at the tips of both main and sub-reflectors which are nearly most critical points, it is realized their channels in the data acquisition system were broken. Therefore; unfortunately no results were taken from the tip points of the reflectors. The accelerometers are bonded directly to the surfaces of the tower and reflector by using aluminum tape and proper Loctite. The axes of the accelerometers are aligned according to axes of the antenna. Then the Multi-Layer Insulation (MLI) parts are covered on the antenna. Figure 2.4 displays the tower and main reflector with their MLI covering positioned on the shaker. Although MLI does not behave significantly in the structural aspect, adding mass makes it important since it changes the natural modes. 2.26 kg of MLI is almost equally separated into tower and main reflector. Such an amount of mass could not be neglected since the total antenna mass is around 33kg.



Figure 2.4. Tower and Main Reflector covered by MLI positioned on Shaker

The software of the data acquisition system is “*Crystal Instruments EDM software Ver: 7.1.0.13*”. The sampling rate is 20.48 kHz by taking a linear average with an average number of 30. 4096 specific data is taken on the frequency domain. The sweeping rate is 2 Oct/Min. The test data are summarized in the Table 2.1. Extracting

data point resolution changes with the frequency. At the beginning of the test, the data acquisition system takes one data at each 0.007 Hz, this resolution expands up to 2.92 Hz at the end of the test. This data resolution depending on the range of frequency of the acquisition system is given in the next figure.

Table 2.1. *Sine Sweep Test Information*

Test Sequence	Tower in -X direction Tower in -Y direction Main Reflector in -X direction Main Reflector in -Y direction
Input Amplitude	0.25 [g]
Frequency Range	5-2000 [Hz]
Sampling Rate	20.48 [kHz]
Sweeping Rate	2 [Oct/Min]
Average Number	30
Data Points	4096

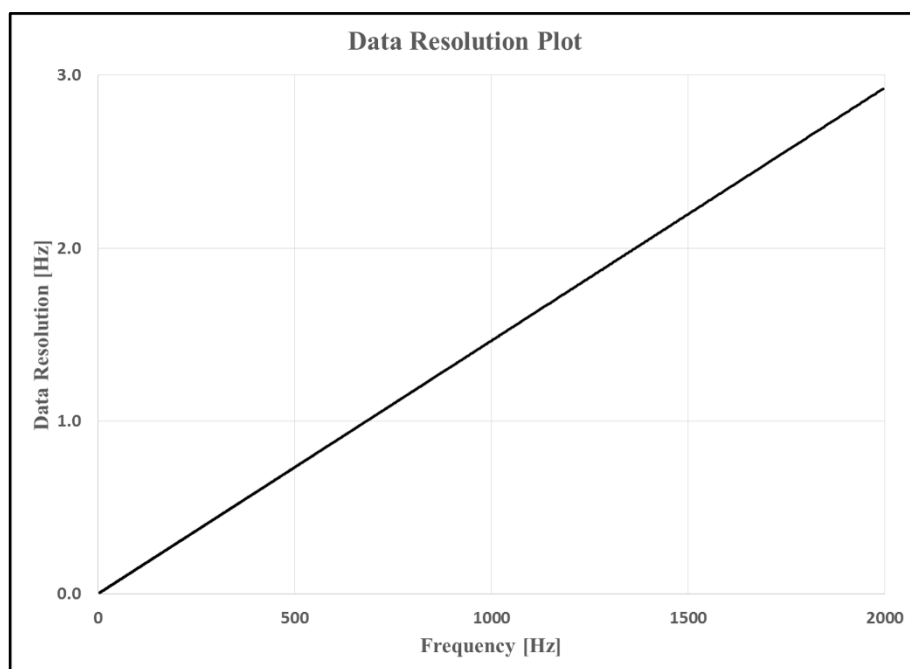


Figure 2.5. Data Resolution Plot of the Sine Sweep Tests

### 2.1.3. Sine Sweep Test Results

In the tests, results from Channel 1 which is the tip of the main reflector and sub reflector is not obtained, unfortunately. Although it is certain that the accelerometer was working before the tests, the test data cannot be reached. The test results were monitored in real-time in order to stop the test for the case of an emergency. The unexpected increase in the excitation or amplitude of the structure's response may be optional emergency cases that might be the reason for damage or failure on the structure. The high and low abortion limits are adjusted to 8dB and -3dB, respectively. The real-time plots in the frequency domain of the X-axis test results for both tower and main reflector are given below in Figure 2.6 and Figure 2.7, respectively. The Y-axis results will also be presented in the Part B of the Appendix via Figure 0.1 and Figure 0.2. All of these plots are prepared on log-log scale. In order to decrease the number of plots, only some of the tests and accelerometers are chosen to be presented. For example, for the vibration tests generally X-axis and mostly tower tests are focused.

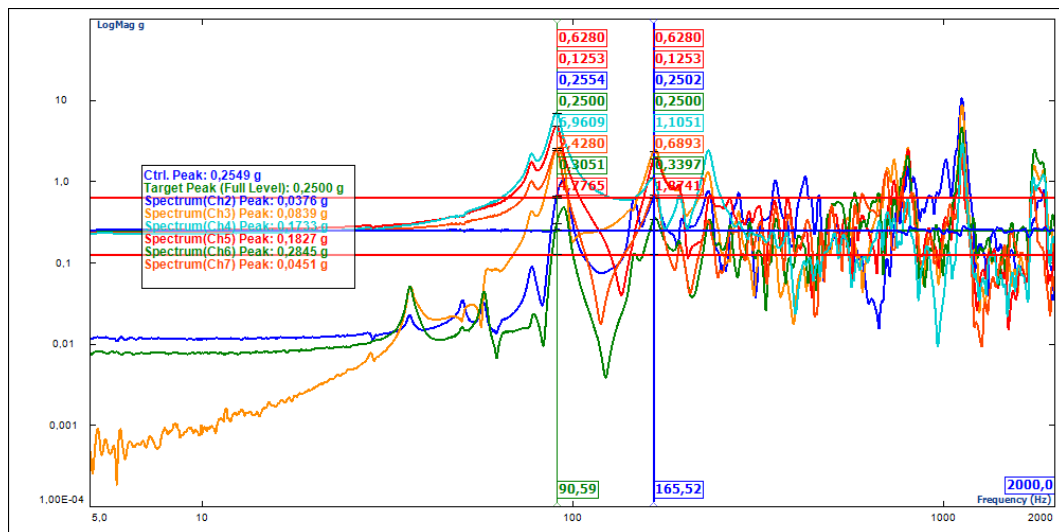


Figure 2.6. Sine Sweep Test Results of Tower along X-axis

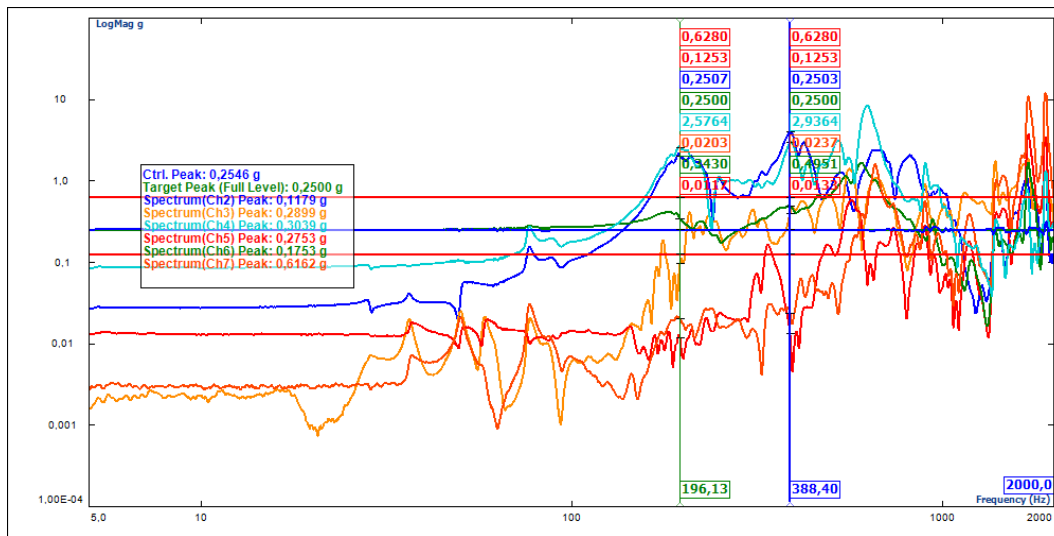


Figure 2.7. Sine Sweep Test Results of Main Reflector along X-axis

Reading the plots will be easier via following the table that gives information about channel id (Ch) and related accelerometers labeled in Section 2.1.2. Table 2.2 gives data only for tower results in X-axis. For the other results which tower Y-axis and main reflector –X and –Y axis Table 0.1 can be used given in the Appendix Part B.

Table 2.2. Situations of Each Channels for Tower X-Axis Sine Sweep Test

Accelerometer ID	Direction	Channel ID	Sensitivity (mV/g)	Max (g)	Overload
SR1	N	Ch2	9,61	10.63	No
T8	Y	Ch3	9,77	8.66	No
T8	X	Ch4	10,30	6.96	No
T7	X	Ch5	9,79	4.78	No
T5	Y	Ch6	9,73	4.61	No
T5	X	Ch7	9,52	2.44	No
Fixture	X	Ch8	9,21	0.28	No

The sine sweep tests involve the structural response data up to 2000Hz as shown in Figure 2.8 which is illustrated in the log-log scale because of its clear presentation. Since the test's range is specified via standards; on the other hand, the selection frequency range of both the tests and analysis is important. In the structural analysis, the low frequencies are accepted to be critical because of the higher displacements and existence of the fundamental frequencies of the structures. Stavrinidis also mentions

the structural importance of the low frequencies [13]. Moreover, Millan and his team support that finite element model should be replaced by hybrid or different methods for the frequencies larger than 800Hz [34]. The upper frequency limits of the vibro-acoustic analyses of the studies are selected as 250Hz by Wickramasinghe [17], 300 Hz by Sikström [12] and Ullio[1] and 400Hz by Marshall [36]. It can be concluded from the literature that if the space structure has its fundamental modes around the low frequency region (smaller than 300 Hz) these low frequencies are more critical for the structure. In addition, the maximum acoustic excitation level occurs at 250Hz, and above this frequency it starts to drop, the details of this acoustic excitation will be provided in the Section 3.1. Therefore, 750Hz is selected as the upper frequency limit of the vibration and acoustic analyses, conservatively, due to existing of the structurally critical modes at the low frequencies and the weak excitations above this frequency limit. Hence, Figure 2.9 illustrates the sine sweep test results up to 750 Hz, in normal scale, not log-log.

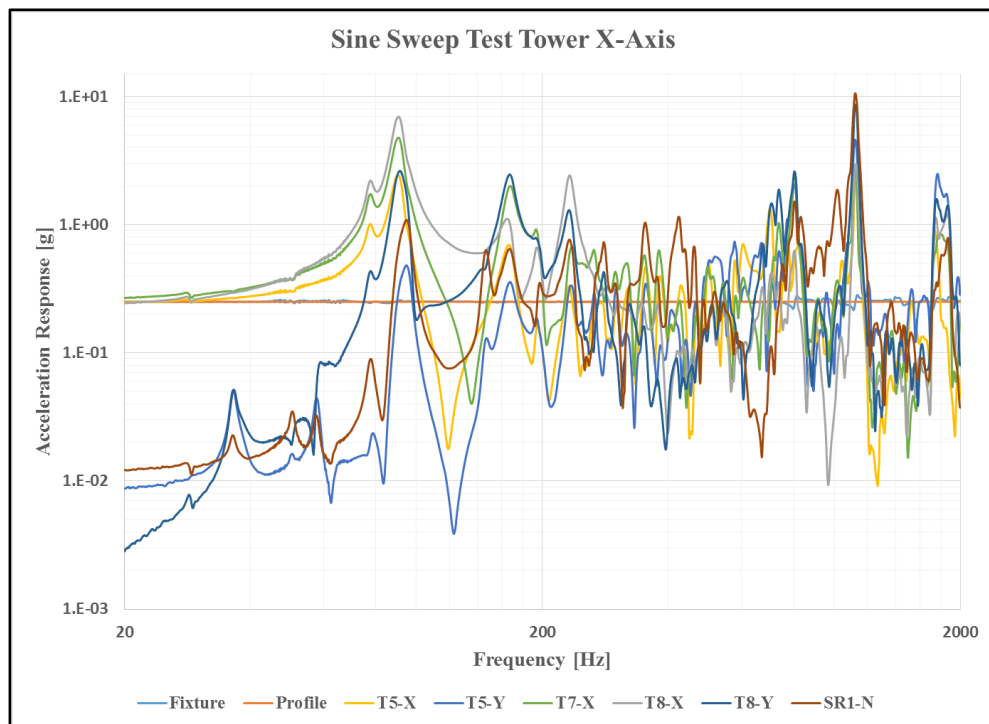


Figure 2.8. Sine Sweep Test Results of Tower X-Axis (up to 2000Hz in the log-log scale)

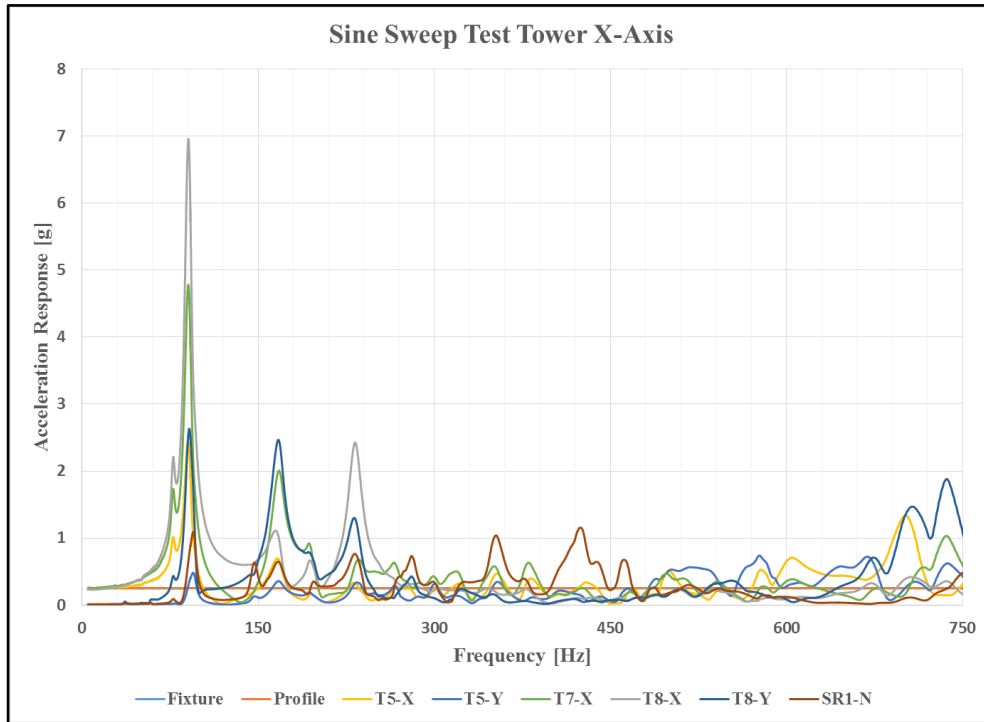


Figure 2.9. Sine Sweep Test Results of Tower X-Axis (up to 750Hz)

The main aim of these tests is to determine the first few modes of tower and main reflector which are structurally critical. The fundamental frequencies are 91 Hz and 173 Hz for tower and main reflector. Other observed resonance frequencies from data are listed in Table 2.3.

Table 2.3. Natural Frequencies of Tower and Main Reflector Resulted From Sine Sweep Test

Subassembly	Natural Frequencies
Tower	91Hz, 96 Hz, 167 Hz, 233 Hz, 265 Hz, 280 Hz, 300 Hz, 318Hz, 353Hz, 382Hz, 425Hz, 461Hz, 503Hz, 525Hz, 561Hz, 577Hz, 605Hz, 668Hz, 676Hz, 705Hz, 737Hz, 802Hz, 834Hz, 1105Hz, 1128Hz, 1200Hz, 1366Hz, 1536Hz
Main Reflector	191Hz, 214Hz, 244Hz, 287Hz, 319Hz, 339Hz, 424Hz, 439Hz, 481Hz, 525Hz, 569Hz, 585Hz, 630Hz, 658Hz, 665Hz, 742Hz, 828Hz, 862Hz, 881Hz, 902Hz, 941Hz, 1331Hz, 1426Hz

It is important to note that the extracted natural frequencies from the sine sweep test probably do not capture all of the modes since different from a modal analysis with an impulse hammer excitation is applied from one location only. However, it is believed that lower natural frequencies which are more likely to be excited significantly by acoustic waves are most likely captured. Since this test is not a modal test it lacks the ability to obtain the mode shapes with tests.

Moreover, it is important to remark that, although the frequency range of the test is 2000Hz, the main focus is the first 750Hz since it is the upper limit of the vibro-acoustic analysis because acoustic load in the reverberation chamber test starts to drop significantly for frequencies above 750 Hz as will be emphasized in the relevant sections. In order to make a good discussion about the tests, each accelerometer's maximum responses and corresponding frequency values (up to 750Hz) are presented via Table 2.4 and Table 2.5. Firstly, Table 2.4 presents that the maximum responses of the tower occur at the first two natural frequencies mostly. For example, for the tower's X-axis test 4 of the 6 channels have the maximum values at 91Hz which is the first natural frequency while the other two at 425 Hz and 91 Hz. For the Y-axis, 3 of the accelerometers have maximum responses at 91Hz, the others are at 96Hz, 148Hz and 707 Hz. In addition to this output, the maximum responses are 6.96091g at 91Hz for the X-axis while 7.35775g at 148Hz for the Y-axis. Remember that the input excitation is 0.25g and this implies that the tower amplifies the base excitation as 27.8 and 29.4 times at the X- and Y- axis. Furthermore, although the main reflector has specific peaks around 200Hz, the maximum responses are not focused on a specific point like the tower. The main reflector's X-axis test results maximum response at 630Hz with an amount of 8.48810g while the response of 6.01916g occurs at 572Hz for the Y-axis. Table 2.5 shows that the frequencies with maximum response for any channel at X-axis are different from each other. However; 3 of the 6 results of the Y-axis focus on the 572Hz. These focused natural frequencies imply that at those values, one of the most dominant mode shapes occurs. Additionally, main reflector's output over input ratios for the X- and Y- axis tests are 34 and 24.1 respectively. It can be concluded

that, main reflector is more critical in the X-axis than the Y-axis although the tower has similar behaviors at both axis.

Table 2.4. *Maximum Responses and Corresponding Frequencies of Tower Sine Sweep*

<b>Accelerometer ID / Direction</b>	<b>Tower – X-Axis</b>		<b>Tower – Y-Axis</b>	
	<b>Maximum Response [g]</b>	<b>Frequency [Hz]</b>	<b>Maximum Response [g]</b>	<b>Frequency [Hz]</b>
SR1-N	1.15	425	7.36	148
T8-Y	2.63	91	6.16	96
T8-X	6.96	91	1.32	91
T7-X	4.78	91	0.90	91
T5-Y	0.75	576	1.99	91
T5-X	2.44	91	0.68	707
Fixture	0.26	-	0.26	-

Table 2.5. *Maximum Responses and Corresponding Frequencies of Main Reflector Sine Sweep*

<b>Accelerometer ID / Direction</b>	<b>Main Reflector – X-Axis</b>		<b>Main Reflector – Y-Axis</b>	
	<b>Maximum Response [g]</b>	<b>Frequency [Hz]</b>	<b>Maximum Response [g]</b>	<b>Frequency [Hz]</b>
MR3-N	4.04	390	2.99	700
MR4-N	1.41	563	6.02	572
MR1-N	8.49	630	3.96	572
MR5-Y	0.58	572	2.01	572
MR5-X	1.69	605	0.77	742
MR5-Z	1.61	660	3.07	660
Fixture	0.26	-	0.26	-

Then, although some peaks burst near 2000 Hz, it is interpreted that these peaks show up because of the shaker’s modes. Another evidence of this case is that, all of four test results include peaks at this interval (1700-2000Hz) especially at 1760Hz and 1900Hz. Thus, the peaks at these regions are neglected since they are related to the natural frequencies of the tower or main reflector.

In conclusion, despite some disadvantages, sine sweep tests propose valuable outputs in terms of especially determining the natural frequencies like 91Hz and 173Hz for

tower and main reflector, respectively. Maximum responses show that tower has around 28 and 30 times while main reflector 34 and 24 times amplification factors at the X and Y-axes.

## **2.2. Vibration FEM Analysis of the Antenna**

In this section construction of the Finite Element Model (FEM), modal analysis and frequency response analysis of the antenna are introduced and the results will be presented at the related subsections.

### **2.2.1. FEM Model of the Antenna**

This section gives information about finite modelling of the antenna not only strategy behind it but also details such as used cards, element types so on. Firstly, for the building of FEM of the antenna the CAD model which is designed in CATIA is directly used. The mid-surfaces of each part and meshing steps are done by using HyperMesh and MSC. PATRAN. Since the sine sweep tests are separately performed for tower and main reflector, these subassemblies are modeled independently.

The structure is meshed in HyperMesh by surface elements. GRID elements symbolize the nodes and they are connected to each other via CQUAD (quadrilateral plate element) and CTRIA3 (triangular element connection) cards. CQUAD constructs element from 4 grid points while CTRIA3 uses 3 grids. CQUAD4 and CTRIA3 outputs the element results according to their local coordinate systems CQUADR and CTRIAR in default (Figure 2.10) [25]. Both of the element types provide membrane stiffness and bending are used as mesh elements and they have to be connected to the PSHELL card which is used for anisotropic materials like composites [25]. The CQUAD4 elements should not be used if sharp changes on the geometries; hence, most of the surfaces are meshed by CQUAD4, only few CTRIA3 are used where sharp edges exist.

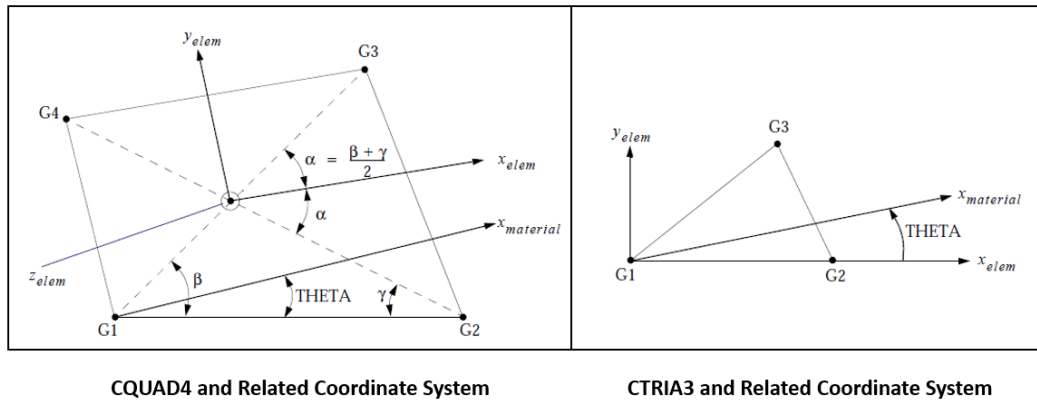


Figure 2.10. CQUAD4 and CTRIA3 elements [25]

The nodes are connected to each other by CBAR elements (simple beam) which has to be entered with PBAR card. Because of attachment of accelerometers at curved surfaces like reflectors, defining local coordinate systems is critical to read the results in the surfaces' normal directions. Thus, at each accelerometer points on the surfaces, local coordinate systems are defined by using CORD2R card.

The mesh dimensions are selected through mesh independence studies. The maximum mesh size is selected as 9 mm for composite, 5-10 mm for metallic parts of the antenna.

Furthermore, one of the main reasons for the selection of NASTRAN as the solver is its successful abilities on the layered composite materials. Some techniques that obtain equivalent material properties for composite sandwich structures are presented in the literature. For example, in their articles Bai and Boudjemai suggest different determination methods of equivalent material properties such as Young's and Shear Moduli, thickness, density, etc. for composite structures [29,30]. Denli and Sun also review Equivalent Single-Layer, Discrete-Layer, Zigzag, Layerwise and Variable Kinetic Theories [33]. Although these methods are beneficial especially for plate-like structures, their usage would not be proper for this study because of the complexity of the geometry and problem. Therefore, NASTRAN through its elements tailored for composite sandwich structures is convenient to use for this application. MAT8 card describes the orthotropic material properties for shell elements. MAT8 card requires elastic moduli ( $E_1, E_2$ ), Poisson's ratio ( $\nu_{12}$ ), in-plane and transverse shear moduli

$(G_{12}, G_{1z}, G_{2z})$ , thermal expansion coefficients  $(\alpha_1, \alpha_2)$ , allowable stresses or strains and structural damping coefficients where subscripts 1 and 2 show the longitudinal and transverse directions. For each different type of composite materials such as prepreg layers of the skins, honeycomb, MAT8 cards are prepared, individually. The stress-strain relation for MAT8 can be given via the following equation ( 17):

$$\begin{Bmatrix} \varepsilon_1 \\ \varepsilon_2 \\ \gamma_{12} \\ \gamma_{1z} \\ \gamma_{2z} \end{Bmatrix} = \begin{bmatrix} \frac{1}{E_1} & \frac{-\nu_{21}}{E_2} & 0 & 0 & 0 \\ \frac{-\nu_{12}}{E_1} & \frac{1}{E_2} & 0 & 0 & 0 \\ 0 & 0 & \frac{1}{G_{12}} & 0 & 0 \\ 0 & 0 & 0 & \frac{1}{G_{1z}} & 0 \\ 0 & 0 & 0 & 0 & \frac{1}{G_{2z}} \end{bmatrix} \begin{Bmatrix} \sigma_1 \\ \sigma_2 \\ \tau_{12} \\ \tau_{1z} \\ \tau_{2z} \end{Bmatrix} + (T - T_{ref}) \begin{Bmatrix} A_1 \\ A_2 \\ 0 \\ 0 \\ 0 \end{Bmatrix} \quad (17)$$

Then, PCOMP defines the layered sandwich structures by combining layers' material properties (MAT8), thicknesses, orientation and number of layers. It should be remembered that the sandwich composite consists of carbon honeycomb core between two skins (each has 4 layers of pre-preg); in other words for each composite structure has 9 layers in total. The directions of the pre-pregs are  $0^0/45^0/-45^0/0^0$  where  $0^0$  shows the principal or longitudinal direction while its thickness is  $2E-4$  m. PCOMP card is presented via Figure 2.11 with Tsai-Wu failure criterion (F.T.) as given in the equation ( 25 ) in the Appendix A,  $20^0C$  reference temperature (TREF), structural element damping ( $GE=2E7$ ), orthotropic materials with their IDs, thicknesses, orientations, stress/strain output requests.

PCOMP	PID	ZO	NSM	SB	F.T.	TREF	GE	LAM
\$	MID1	T1	THETA1	SOUT1	MID2	T2	THETA2	SOUT2
\$	MID3	T3	THETA3	SOUT3	MID4	T4	THETA4	SOUT4
PCOMP	200000		-.011075		TSAI	20.	2.7	9+7
	5	2.-4	0.	YES	5	2.-4	45.	YES
	5	2.-4	-45.	YES	5	2.-4	0.	YES
	6	.02055	0.	YES	5	2.-4	0.	YES
	5	2.-4	-45.	YES	5	2.-4	45.	YES
	5	2.-4	0.	YES				

Figure 2.11. PCOMP Card constructing the sandwich composite structure

CBUSH and PBUSH cards are used to add spring/stiffness between two grid points. These cards are one of the most critical CARDS because determining natural frequencies is directly depends on the stiffness. The selection of these stiffness values is an iterative process and required validation with test data. PBUSH requires 6 stiffness values that are translational and rotational about the principal directions.

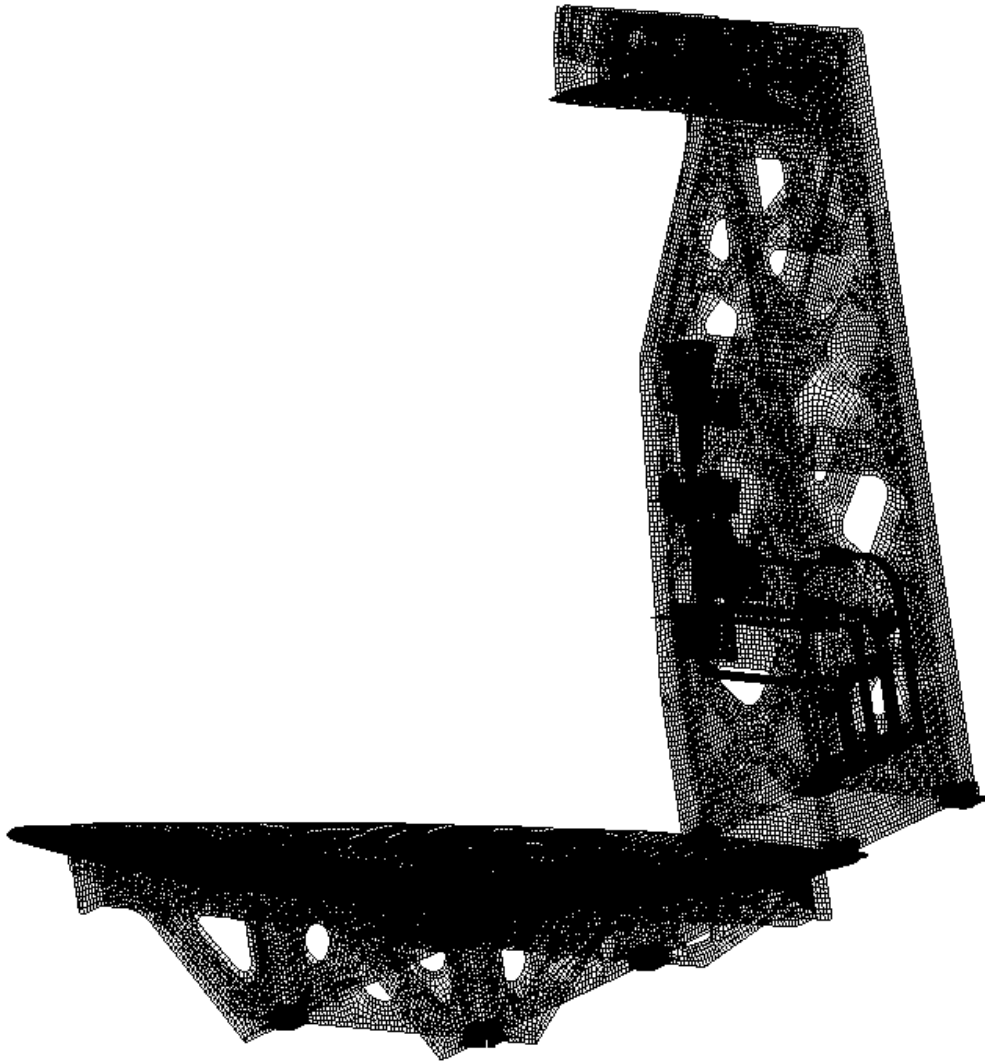
NSML1 is used to add mass to the elements of each part which are measured and recorded during the manufacturing process instead of using density values [23]. The core and sandwich thicknesses and masses of each independent composite parts are individually modeled. Similarly, the material type and masses for the metallic parts are the other inputs for the finite element model. The details of finite element modeling are summarized via Table 2.6.

Table 2.6. *Finite Element Model Details*

<b>CARD</b>	<b>Tower Sub-Assembly</b>	<b>Main Reflector Sub-Assembly</b>
Nodes	50027	36782
Elements	49080	37248
Coordinate Frames	5	5
Material Properties	10	6
Element Properties	78	28
MPC Data	263	10
PBAR	1	1
CBAR	400	510
PCOMP	28	21
CQUAD4	47495	35760
CTRIA3	1020	914
PLOTEL	60	53
PBUSH	5	1
CBUSH	106	10
GRID	50027	36783

<b>CARD</b>	<b>Tower Sub-Assembly</b>	<b>Main Reflector Sub-Assembly</b>
CORD2R	5	6
NSML1	49	49

Finally, the model is exported in “.bdf” format to be used in the modal, frequency response dynamic and vibro-acoustic analyses throughout the thesis. Figure 2.12 displays the mesh of the FEM of the antenna shown in MSC. PATRAN.



*Figure 2.12. FEM Mesh of the Antenna via PATRAN*

### 2.2.2. Modal Analysis of the Antenna

The mode shapes and natural frequencies are determined by using MSC Nastran 2016.1 through SOL103 (SEMODES) “Real Eigenvalue Analysis”, Modal Analysis. The reference model which is prepared in section 2.2.1. FEM Model of the Antenna is included to the new ‘.bdf’ file which is used to obtain solutions. The boundary conditions which are shown at Figure 2.2 are given to the nodes that specify the fastening holes as “SPC (Single Point Constraint)” card by corresponding stiffness values. Four nodes construct each mounting hole. The eigenvalues are determined via “EIGRL” card up to 2000Hz which is the upper limit of the sine sweep test. Displacements and accelerations are selected as output in ‘.op2’ format which is an output format of NASTRAN for all nodes to see the mode shapes.

Firstly, the tower subassembly is analyzed. The modal solver outcomes 273 mode shapes and first five natural frequencies are 91Hz, 96Hz, 167Hz, 177Hz and 179Hz for the tower. Similar to tower, main reflector subassembly also is solved by modal analysis. Here, there are 250 mode shapes in total. The first five natural frequencies are 199Hz, 216Hz, 243Hz, 244Hz, 257Hz. The all computed natural frequencies for both tower and main reflector are given in the Appendix.

Moreover, the modal effective mass fractions dependent on the natural frequencies for each subassembly are computed. “Modal Effective Mass Output Request’ ‘MEFFMASS’ card of the NASTRAN is used to evaluate the modal effective mass fraction in the normal modes analysis” [45]. The formulation of the effective mass matrix is given by the user manual [45] by equation ( 19 ) and Table 2.7.

$$\text{Modal Effective Mass Matrix} = [\varepsilon^T][m][\varepsilon] \quad ( 18 )$$

Table 2.7 Properties of the MEFFMASS Card

$\varepsilon$	Modal Participation Factors : $[m^{-1}][\Phi^T][M_{aa}][D_{ar}]$
m	Generalized Mass Matrix
$\Phi$	Eigenvectors
$[M_{aa}]$	Mass Matrix Reduced to the a-set
$[D_{ar}]$	Rigid Body Transformation Matrix with respect to the a-set
$[D_{ar}^T][M_{aa}][D_{ar}]$	A-set rigid body mass matrix

Mass fractions can be thought of as how much of the structure joins to the corresponding mode shape. Table 2.8 displays this calculation that takes the mass fractions directly from the result file (.f06) and highlights the values which are higher than 5% for the tower. In the table  $T_i$  and  $R_i$  are translational and rotational mass fraction in the direction of i, respectively. By this table, it is concluded that only first 4 modes are structurally critical for the tower. Even the first two modes (91.7Hz and 96.9Hz) are the most important ones since the fractions are larger than 50% while the other two have around 10% mass fractions. This can be proved via the sine-sweep test. Remember that most of the maximum responses of the tower's sine sweep tests are seen at these two natural frequencies.

Table 2.8 Effective Mass Fractions for Tower

Mode Number	Frequency [Hz]	Fraction		$\geq 5\%$			
		Effective Mass Fractions					
		$T_x$	$T_y$	$T_z$	$R_x$	$R_y$	$R_z$
1	91.7	54.1894	1.4368	0.0031	0.7652	85.3846	53.6725
2	96.9	1.5706	51.1267	0.8767	21.9378	1.6995	0.0311
3	167.4	0.0033	10.6165	8.7848	15.3943	0.6126	0.4664
4	177.5	6.0284	0.0167	0.2245	0.1848	2.3076	7.8832

Effective mass fraction table for main reflector (Table 2.9) is also provided like tower. On the other hand, main reflector's case is more complicated than the tower's, since it has 14 modes with more than 5% effective mass fraction. It can be interpreted that 1<sup>st</sup> (199Hz), 2<sup>nd</sup> (216Hz) and 8<sup>th</sup> (317Hz) modes are the most critical since their fractions are larger than 30% while the others have around 10%.

Table 2.9 Effective Mass Fractions for Main Reflector

Mode Number	Frequency [Hz]	Fraction		≥ 5 %			
		Effective Mass Fractions					
		$T_x$	$T_y$	$T_z$	$R_x$	$R_y$	$R_z$
1	199.0	0.0038	16.1076	0.1030	65.8906	0.0004	2.9263
2	216.4	16.9288	0.0043	0.0004	0.0111	52.5999	1.2676
4	244.3	0.0140	0.0055	0.0011	0.1831	1.2528	18.7344
5	257.3	3.2903	0.0017	0.0024	0.1056	11.3845	10.6786
7	297.2	0.0369	0.4032	9.8042	6.3839	3.3661	0.0028
8	317.3	0.0147	1.2733	35.4401	7.5112	8.0213	0.5460
9	361.2	0.1885	0.4973	7.4536	0.1825	1.8340	0.1377
11	431.5	1.8599	0.0041	0.0225	0.0081	1.4022	6.3582
14	495.5	1.1298	5.5977	0.1904	0.4854	0.0074	0.0006
17	525.5	2.3814	10.6196	1.5487	1.8130	1.1973	0.0834
19	536.5	8.2155	6.8180	0.4261	0.7703	0.1627	8.9993
20	571.9	0.0818	8.5717	1.7912	0.4046	0.3501	1.3489
21	578.7	0.4462	11.3047	0.0271	0.1200	0.0116	3.8698
25	611.3	12.5044	0.1642	2.2202	0.7010	1.0748	4.2828
26	639.7	6.4577	2.3148	0.0436	0.1513	0.0088	1.4609
27	642.0	1.2856	5.9445	0.0561	0.2924	0.0742	3.8186
28	657.8	0.4353	6.0083	8.8756	1.3371	2.4973	1.8564
29	674.1	8.7041	0.7565	0.3456	0.1049	0.0072	4.2097

The most critical mode shapes which are 1<sup>st</sup> and 2<sup>nd</sup> for tower while 1<sup>st</sup>, 2<sup>nd</sup>, 4<sup>th</sup> and 8<sup>th</sup> for the main reflector assemblies will be shown in Figure 2.13 and Figure 2.14.

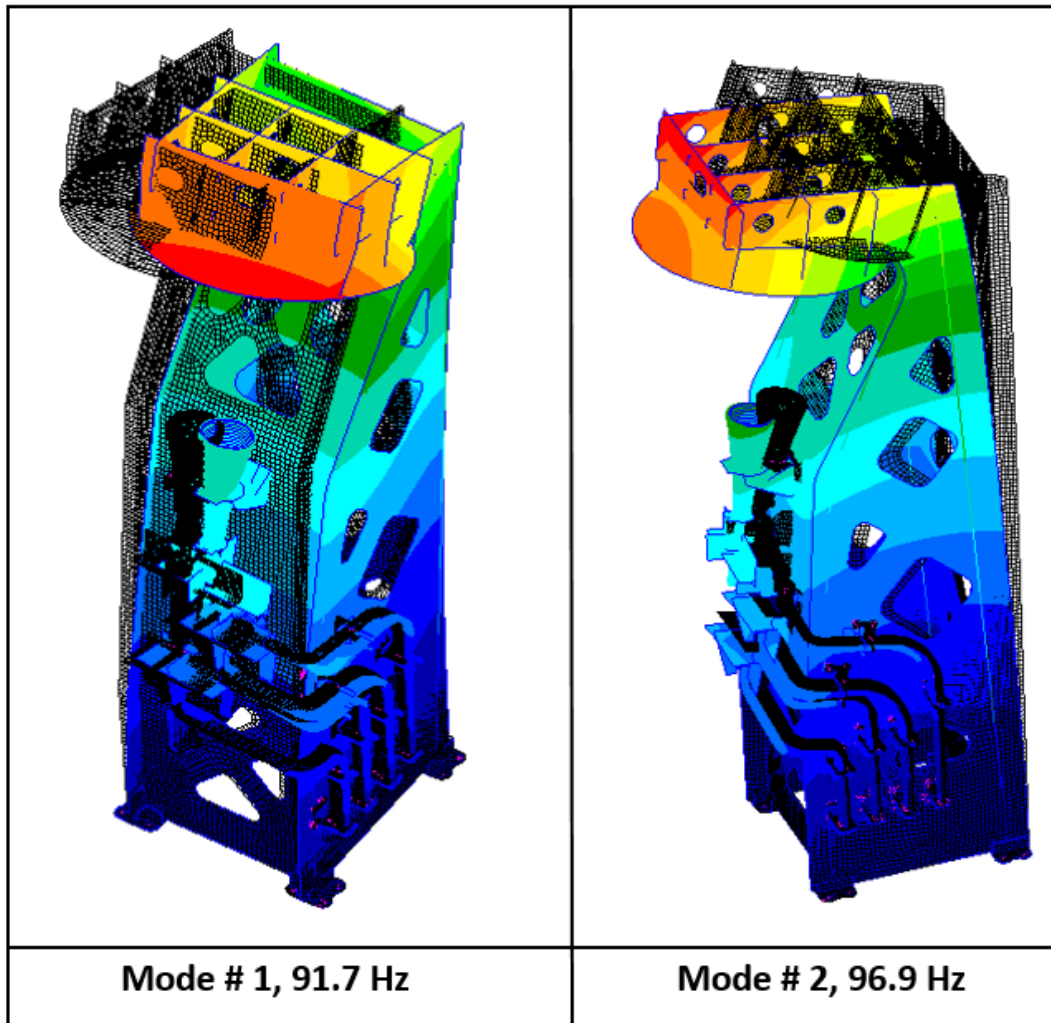


*Figure 2.13. Tower's 1<sup>st</sup> and 2<sup>nd</sup> Mode Shapes*

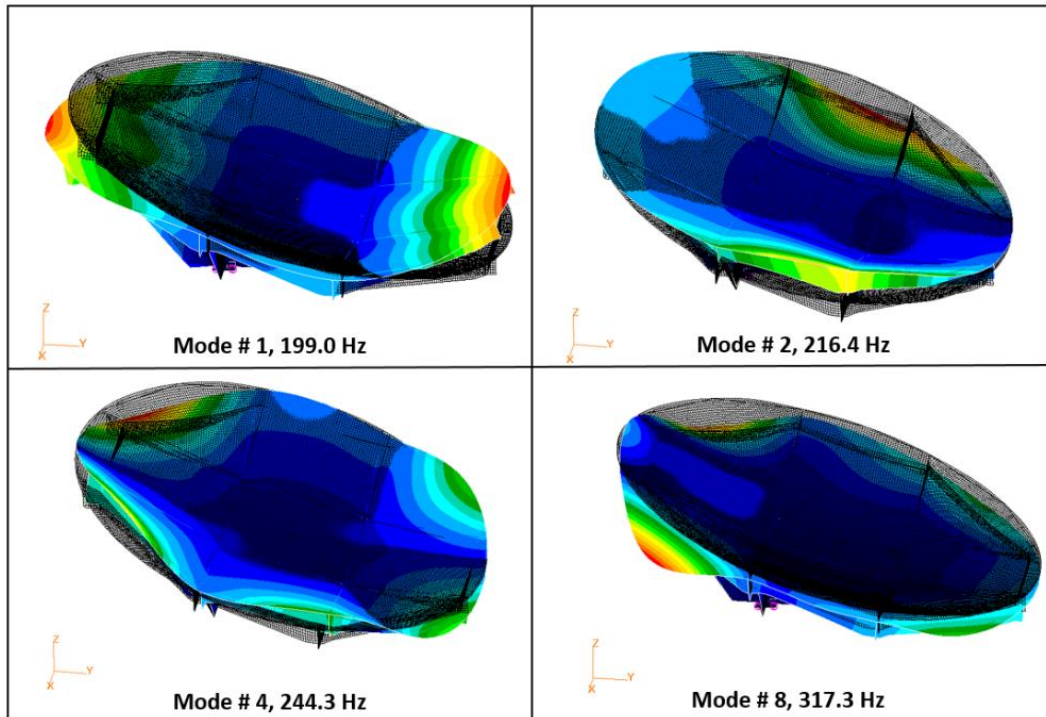


Figure 2.14. Main Reflector's 1<sup>st</sup>, 2<sup>nd</sup>, 4<sup>th</sup> and 8<sup>th</sup> Mode Shapes

### 2.2.3. Frequency Response Analysis of the Antenna

The sine sweep test is simulated via 'Modal Frequency Response' analysis (SOL 111-SEMFREQ) through MSC Nastran 2016. This solver uses modal formulation rather than direct one to shorten the solution time and decreases the required memory requirement.

For the frequency response analysis, the model which was prepared at the Section 2.2.1 was directly used by "INCLUDE" card. Although frequency range for the analysis is chosen as until 2000Hz with 0.25Hz resolution with "FREQ1" card, the main focus is solutions at up to 750Hz. In order to specify boundary conditions; all the mounting holes are modelled by 'CBUSH' and 'PBUSH' cards as in the modal analysis. All of these CBUSH elements are connected to a single grid which is used to give the excitation to the systems via 'RBE2' elements. The excitation with magnitude "0.25g" is applied to this common point with "DLOAD" and "RLOAD" cards. The shaker is simulated in this way.

### 2.2.3.1. Damping and Half-Power Bandwidth Method

Damping is one of the most important phenomena for structural problems. Determination damping is a challenging problem since it depends on the various concepts such as the geometry of the structure, temperature of the environment, molecular effects of materials such as porosity or sizes of the grains, the life-time of the structures and stress [40]. Nanda's articles emphasize the difficulty of the damping specification for the composite and jointed materials. For such systems, damping depends on the design of the composites like the number of layers, size of the cores, thicknesses, sizes and torque values of the fasteners, friction coefficient at the mountings, frequency and excitation level [41,42].

During this thesis three different methods are followed to determine the damping ratios. Firstly, the values of similar structures found in the literature are used. For example, Viscardi and his team takes the damping ratio as 1.73% for carbon fiber epoxy according to study done in their laboratory in Universita Degli Studi di Napoli [43]. Similarly, in his book Wijker suggests a frequency dependent damping table as the damping ratios changes between 1-5% [27]. Another research also accepts the damping ratio as 4% for composite structures [36]. Hence, although different values are used for composites' damping ratio, generally it is accepted between 1% and 10%.

The second approach is the Half-power bandwidth method which suggests a practical method to determine the damping ratios. The resonant peaks are focused and amplitude value at resonance ( $\omega_0$ ) is extracted. This response peak value is divided by  $\sqrt{2}$ (=0.707) which is called as half-power value. The intersection points of the half-power values and the response curve are named as half-power points. The difference between frequencies of the intersection points is calculated and called a frequency difference ( $\Delta\omega$ ). Mangal and Gupta present a graph of this phenomenon which is given in Figure 2.15 [20]. Finally, the damping ratio ( $\xi$ ) is calculated by using ( 19 ). Some of the damping ratios are specified by using this method.

$$\xi = \frac{\Delta\omega}{2\omega_0} \quad (19)$$

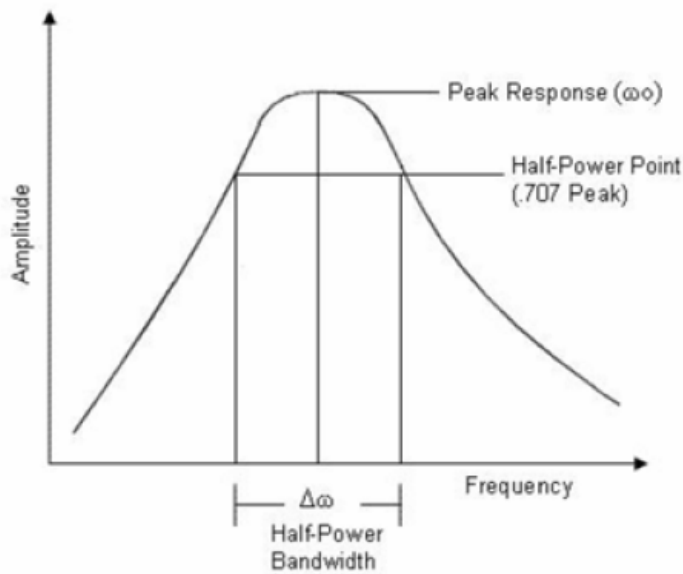


Figure 2.15. Half-Power Bandwidth Method Schematic [20]

The final method is the iteration process. If the results of the frequency response analysis with damping ratios determined by the specified two methods do not match with the test results, those values are iteratively changed until to reach the test result peaks.

These damping ratios are implemented to the FEM by using “SDAMPING”, “TABDMP1” and “TABLED1” cards. As a result of these three processes, Figure 2.16 shows the damping card of FEM of the tower subassembly in -X direction.

TABDMP1	200	CRIT						
5.	.01800	135.	.01800	136.	.0120	160.	.0120	
161.	.0002	170.	.0002	171.	.015	275.	.015	
276.	.01000	480.	.01000	481.	.04000	550.	.04000	
551.	.004	675.	.004	676.	.0002	677.	.0002	
678.	.00400	700.	.00400	701.	.0009	715.	.0009	
716.	.010	725.	.010	726.	.0008	750.	.0008	
751.	.0011	775.	.0011	776.	.0007	800.	.0007	
801.	.00001	810.	.00001	811.	.02	830.	.02	
831.	.0104	1115.	.0104	1116.	.000060	1130.	.000060	
1131.	.01290	1200.	.01290	1201.	.01290	1700.	.01290	
1701.	.014	1740.	.014	1741.	.00050	1800.	.00050	
1801.	.014	1860.	.014	1861.	.00010	1880.	.00010	
1881.	.014	2000.	.014	ENDT				

Figure 2.16. TABDMP1 Card, Damping Ratios of Tower

### 2.2.3.2. Frequency Response Analysis Results

In this section the results of the frequency response analysis will be provided. Although the analysis was performed until 2000Hz, the examination of this analysis includes the results up to 750 Hz. To begin with, acceleration results for the tower X-axis analysis (at the accelerometer locations) will be shown in a single figure (Figure 2.17). Although only the tower's plot outputs will be presented, all four of the analyses will be discussed. It is important to note that not only results up to 750Hz as explained before acoustic loading decreases as the frequency increases. The main motivation and the tool of these curves are the test data. The damping ratios are iterated until the peak values of the test data are obtained. In order to satisfy these peak values, around 50 different damping ratios are tried.

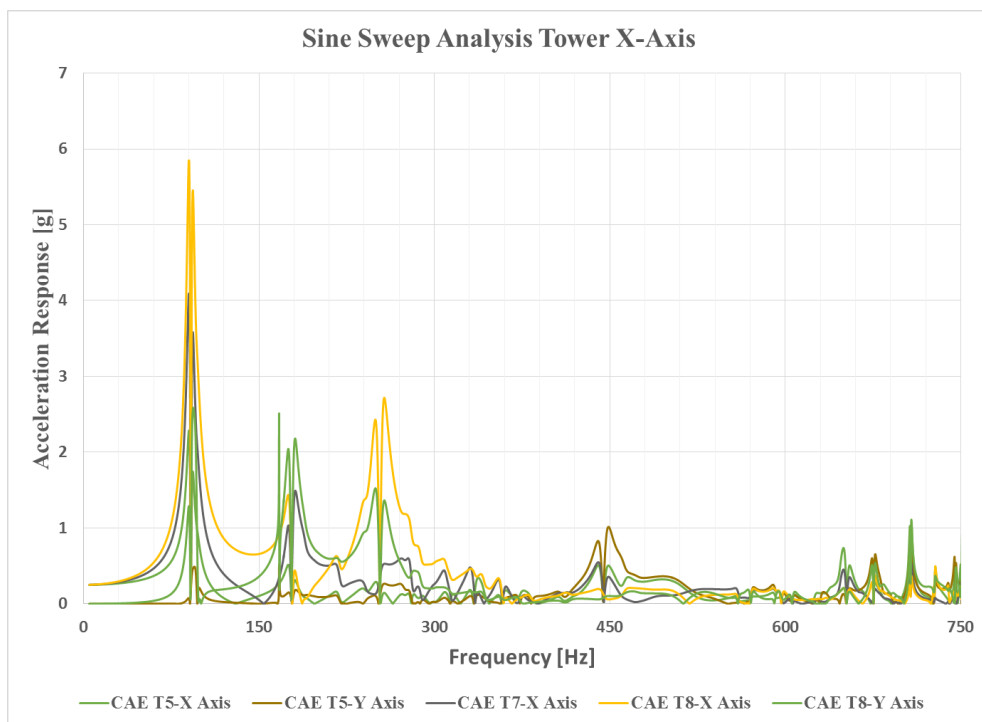


Figure 2.17. Frequency Response Analysis Results for Tower in X-axis (to 750Hz)

In addition to the figures presented above, Table 2.10 and Table 2.11 shows the maximum peak values, corresponding natural frequencies and the amplification ratio which is

the ratio of the response over the excitation input (0.25g) for the tower and main reflector of the both of X- and Y- axes, respectively.

Table 2.10. *Tower's Frequency Response Analysis Maximum Values*

	Accelerometer	T5-X	T5-Y	T7-X	T8-X	T8-Y
X-Axis Excitation	Natural Frequency [Hz]	90.75	448	90.75	90.75	97
	Maximum Peak [g]	2.285	1.016	4.092	5.848	2.585
	Amplification Factor	9.14	4.06	16.36	23.39	10.34
Y-Axis Excitation	Natural Frequency [Hz]	97	97	97	97	98
	Maximum Peak [g]	0.735	2.373	1.221	1.917	6.570
	Amplification Factor	2.94	9.49	4.88	7.67	26.28

From the Table 2.10 it can be concluded that three of five maximum responses of the structure occur at 90.75Hz which is very close to the fundamental natural frequency of the tower while the other two are at 97Hz and 448Hz. As it is expected the responses of the nodes at X-axis are larger than the responses of the same nodes' Y-axis. The largest amplification factor is seen as 23.39 at the T8 (X-axis) node which is the upper side of the tower. Moreover, the results of Y-axis excitation analysis illustrates that four of the maximum responses are seen at 97Hz while the other one is at 98Hz. It can be accepted as these values are the second natural frequency of the tower and the difference can be because of uncertainties of the numerical analysis. Additionally, the Y-axis maximum responses of the accelerations are larger than the X-axis ones as is expected. The maximum amplification factor is 26.28 at the T8 (Y-axis) node. The point is the same as the previous case. It can be concluded that the most affected point of the tower can be accepted as T8 (the top point of the tower) from both of the X- and Y-axis excited analyses. In addition to the tower, a similar study is performed for the main reflector as presented in Table 2.11.

Table 2.11. Main Reflector's Frequency Response Analysis Maximum Values

	Accelerometer	MR1- N	MR3- N	MR4- N	MR5- X	MR5- Y	MR5- Z
X-Axis Excitation	Natural Frequency [Hz]	658	658	658	658	658	658
	Maximum Peak [g]	16.229	21.029	11.996	1.731	2.351	9.390
	Amplification Factor	64.92	84.12	47.98	6.92	9.40	37.56
Y-Axis Excitation	Natural Frequency [Hz]	606	581	598	606	570	606
	Maximum Peak [g]	50.331	22.888	15.821	4.507	1.965	14.003
	Amplification Factor	201.32	91.55	63.28	18.03	7.86	56.01

The main reflector's maximum responses at both of X- and Y-axis excited analyses are examined thanks to Table 2.11. The table shows that all of the maximum peaks are focused on the 658Hz for the X-axis analysis. The maximum response is 21.029g with an amplification factor of 84.12. Moreover, three of the responses are seen at 606Hz while the others are at 570Hz, 581Hz and 598Hz. The maximum response of the Y-axis analysis is 50.331g with an amplification factor of 201.32. From the values at the table, it can be concluded that the maximum values are abnormally large for both axes. Probably, the model of the main reflector may be incapable.

Furthermore, the stress outputs are obtained in addition to displacement and the stress results will be presented for the tower at 90.75Hz and 97Hz, for the main reflector at 216.5Hz and 658Hz. These frequencies are the critical frequencies that the structure responds the most. First of all, Figure 2.18 illustrates the displacement (left) and stress (right) outputs at 90.75Hz which is the first natural frequency of the tower. The maximum displacement whose amount is 0.177mm is seen at the top free edge of the tower. In addition to displacement, the stress graph can be seen at the right of the same figure. The maximum stress is 300 kPa at the interface brackets of the tower. Again this is an expected case since the fixed boundary condition is there. Although the maximum stress is seen as 300kPa at the brackets, the composite structure sees around 170kPa stress. Moreover, the results of the tower for its second natural frequency

which is 97Hz are examined in terms of displacement and stress. In this case, the maximum displacement is 0.102mm while the maximum stress is seen around 200kPa. Again the maximum response locations are the same with the previous case which are the top of the tower for the displacement and bottom brackets for the stress. The composite faces with stress around 85kPa.

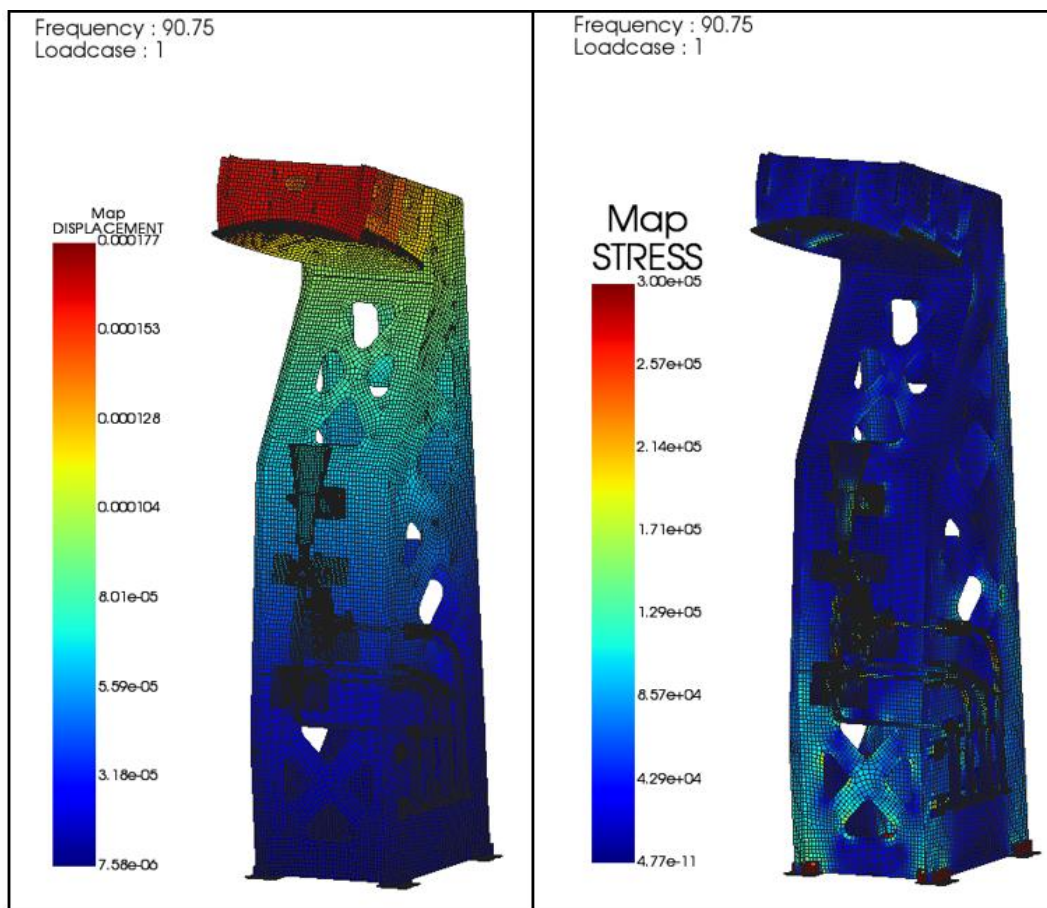
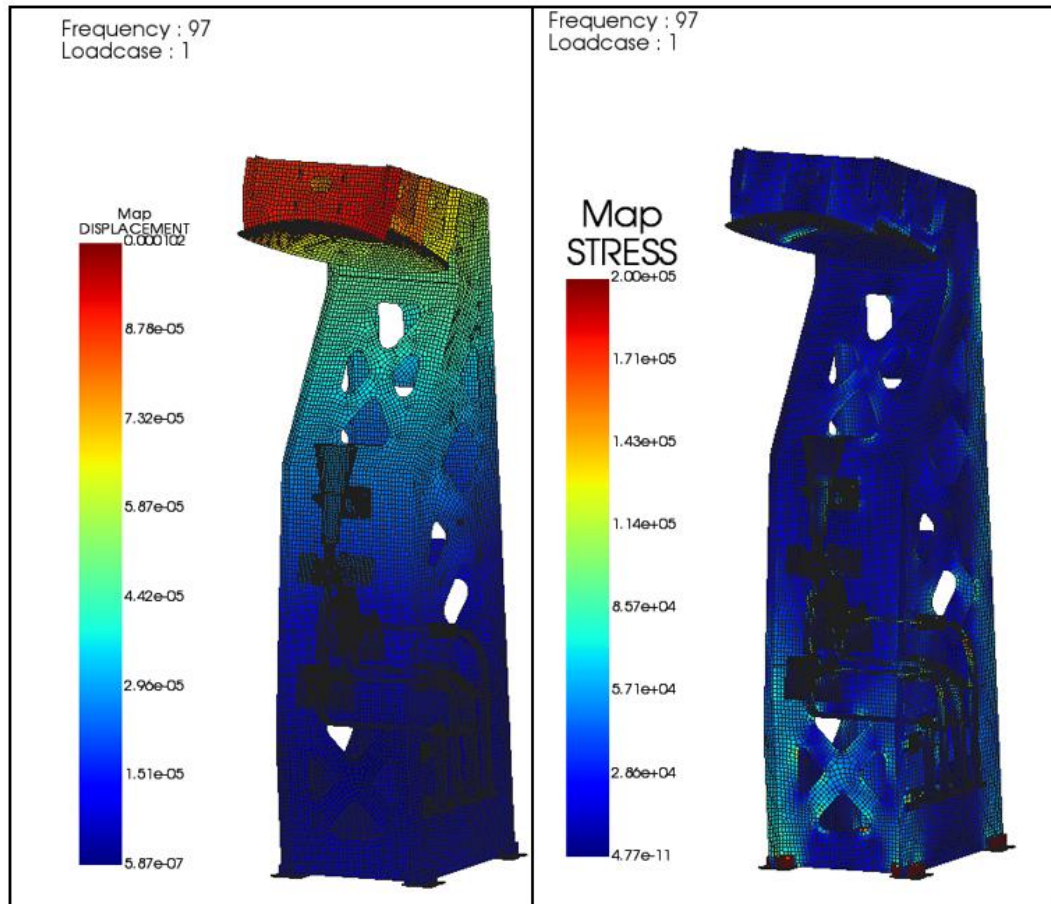


Figure 2.18. Displacement and Stress Output of Tower at 90.75 Hz



*Figure 2.19.* Displacement and Stress Output of Tower at 97 Hz

Then, the main reflector is examined in a similar manner at the frequency 216.5Hz and 658Hz. The maximum displacements of the main reflector are seen as 0.0069mm and 0.0168mm at the right and left edges of the reflector at 216.5Hz and 658Hz, respectively. The reason for this movement of the reflector is because of its mode shape at this frequency. The maximum stresses are seen as 100kPa and 700kPa at the titanium brackets and peripheral ribs under the main reflector. Especially, the peripheral ribs are seen as weak under these conditions. The possible reason for this is that the thickness of these ribs is 10mm while the others are 20mm.

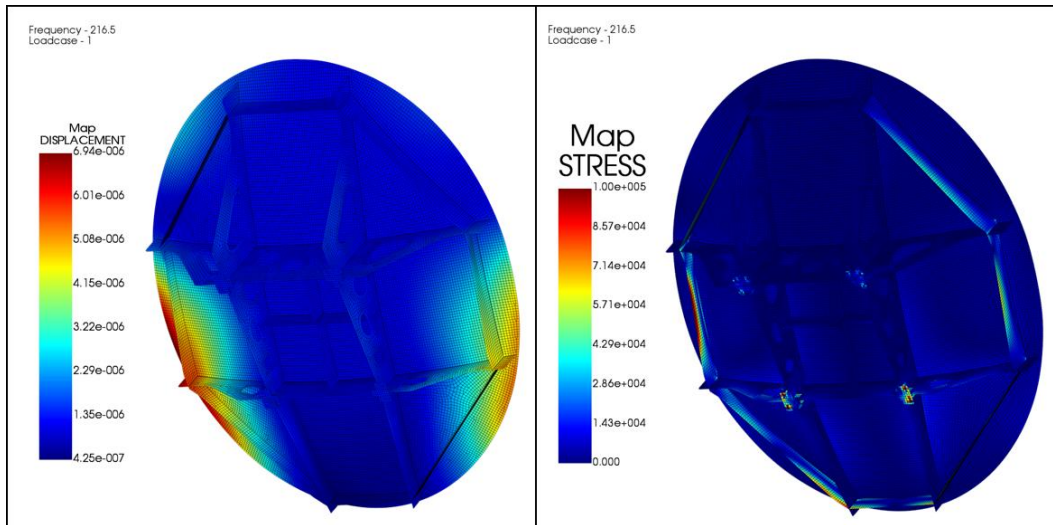


Figure 2.20. Displacement and Stress Output of Main Reflector at 216.5 Hz

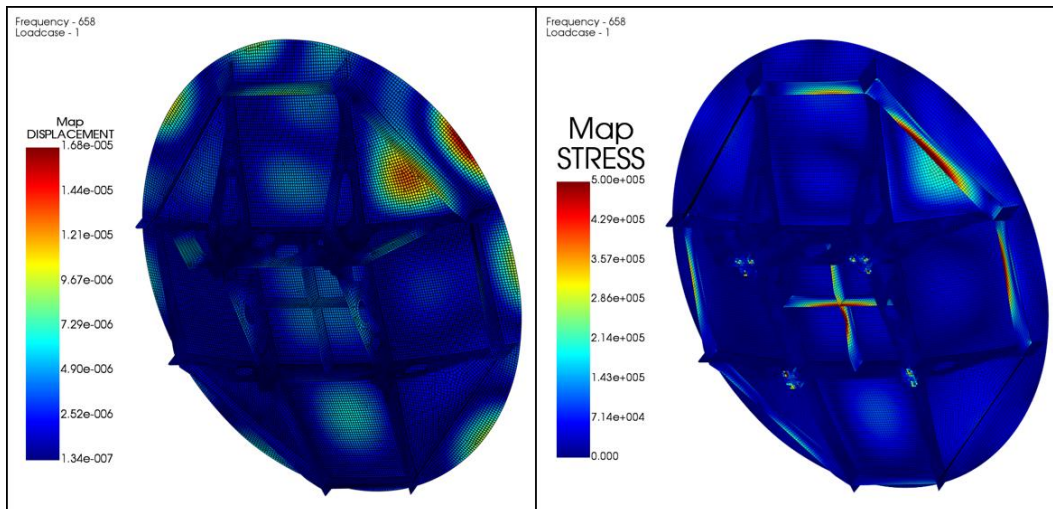


Figure 2.21. Displacement and Stress Output of Main Reflector at 658 Hz

It can be concluded that from the figures, the maximum stresses are seen at the first two natural frequencies for the tower at the interface brackets. Then, the maximum displacements are seen around the top proportion of the tower at the free edges. The stress and displacement values are small as it is expected. Since the small excitation input (0.25g) is large enough to excite the structure; however, it is small to obtain large stress or displacements. In addition to this, these analyses give information about that

the peripheral ribs with 10mm thickness under main reflector are the weakest parts of this sub-assembly since they have the largest stress at the composite parts.

### **2.3. Comparisons of the Vibration Tests and FEM Analysis of the Antenna**

In this section, the comparisons with upper frequency limit of 750 Hz of the finite element analysis and the sine sweep test will be presented. The modal analysis then frequency response analysis results will be compared the sine sweep vibration test data.

The modal analysis results and the natural frequencies obtained from the sine sweep test are considered. Sine sweep test results were presented at the Section 2.1.3. and the natural frequencies obtained from that test are listed at the Table 2.3 for both tower and main reflector. The analysis results are compared with the corresponding test results which are listed at Table 2.12. This table includes the natural frequencies obtained from the sine sweep vibration test and modal analysis in addition to their percentage difference symbolizing absolute error by calculating the ratio of the absolute difference over the test data. As it can be seen from the table the natural frequencies by FEM are so close to the real values. On the other hand, although FEM is seen that it almost perfectly matches the test results, an uncertainty because of the lack of modal test appears. The proper way of this comparison would be that firstly the mode shapes are obtained then corresponding natural frequencies should be compared. So, this comparison unfortunately has some doubts because the mode shapes are not seen by the modal test.

Table 2.12. Comparison of the Natural Frequencies Obtained From Test and Modal Analysis Results up to 750 Hz

Tower				Main Reflector			
Mode Number	Analysis [Hz]	Test [Hz]	Difference %	Mode Number	Analysis [Hz]	Test [Hz]	Difference %
1	91.7	91	0.80	1	199.0	191	4.00
2	96.9	96	0.91	2	216.4	214	1.10
3	167.4	167	0.21	3	243.0	244	0.40
11	237.0	233	1.69	6	283.9	287	1.08
16	260.9	265	1.56	8	317.3	319	0.53
18	280.1	280	0.05	9	361.2	339	6.15
21	299.9	300	0.04	10	414.4	424	2.32
23	313.4	318	1.47	11	431.5	439	1.75
28	357.8	353	1.35	13	476.2	481	1.02
30	382.6	382	0.16	18	528.7	525	0.71
33	421.0	425	0.95	20	571.9	569	0.50
37	462.1	461	0.25	22	584.5	585	0.08
42	499.3	503	0.75	26	639.7	630	1.52
46	523.5	525	0.28	28	657.8	658	0.03
49	559.7	561	0.22	29	674.1	665	1.35
Tower				Main Reflector			
Mode Number	Analysis [Hz]	Test [Hz]	Difference %	Mode Number	Analysis [Hz]	Test [Hz]	Difference %
51	570.6	577	1.13	33	738.3	742	0.50
54	605.8	605	0.14				
62	663.9	668	0.61				
63	675.5	676	0.07				
67	707.2	705	0.31				
71	739.8	737	0.38				

Lastly, the frequency response and test data will be illustrated on the same plot in the Figure 2.22, Figure 2.23 and Figure 2.24.

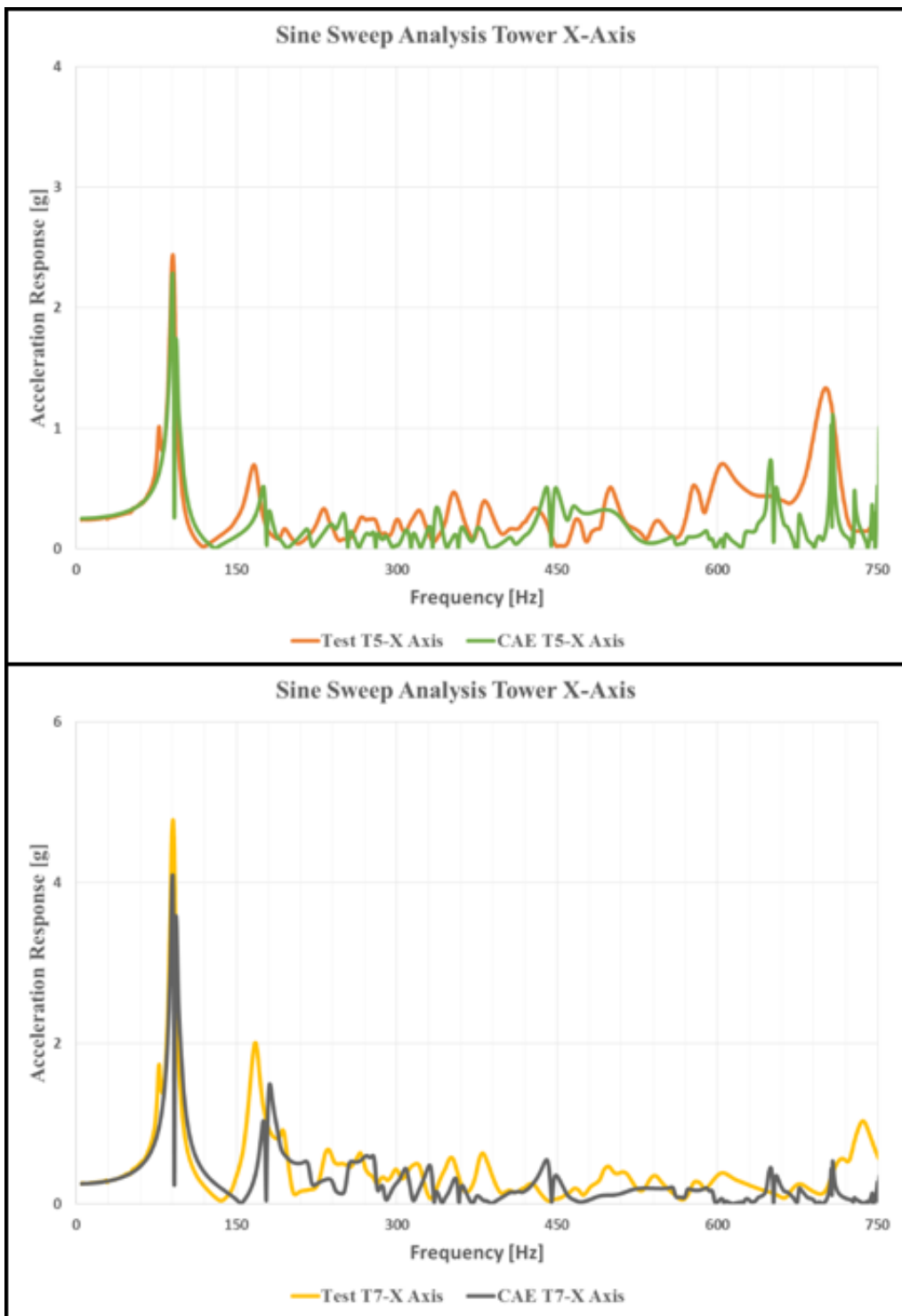


Figure 2.22. Comparison Plot of T5-X and T7-X accelerometers for Tower X-axis excitation

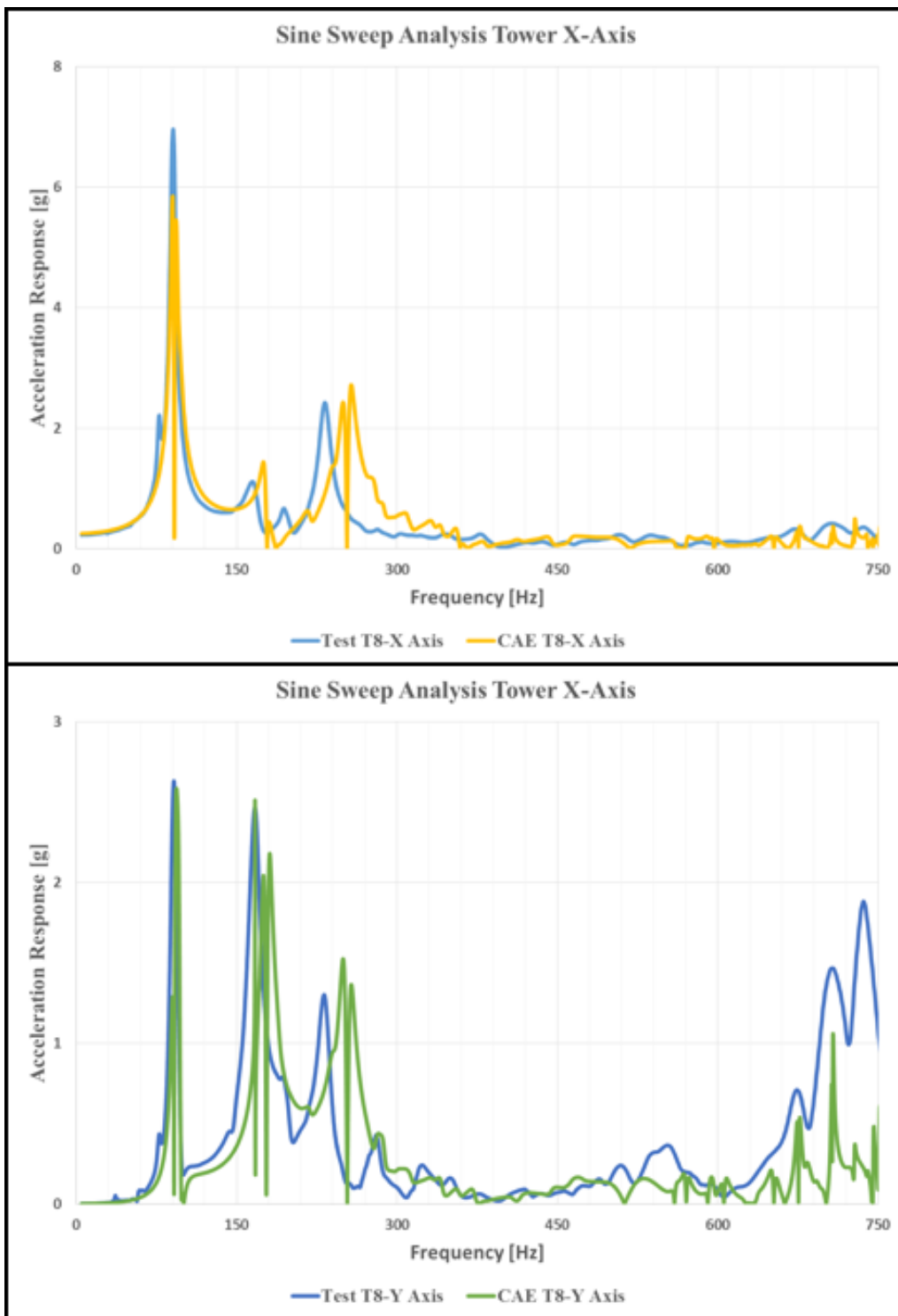


Figure 2.23. Comparison Plot of T8-X and T8-Y accelerometers for Tower X-axis excitation

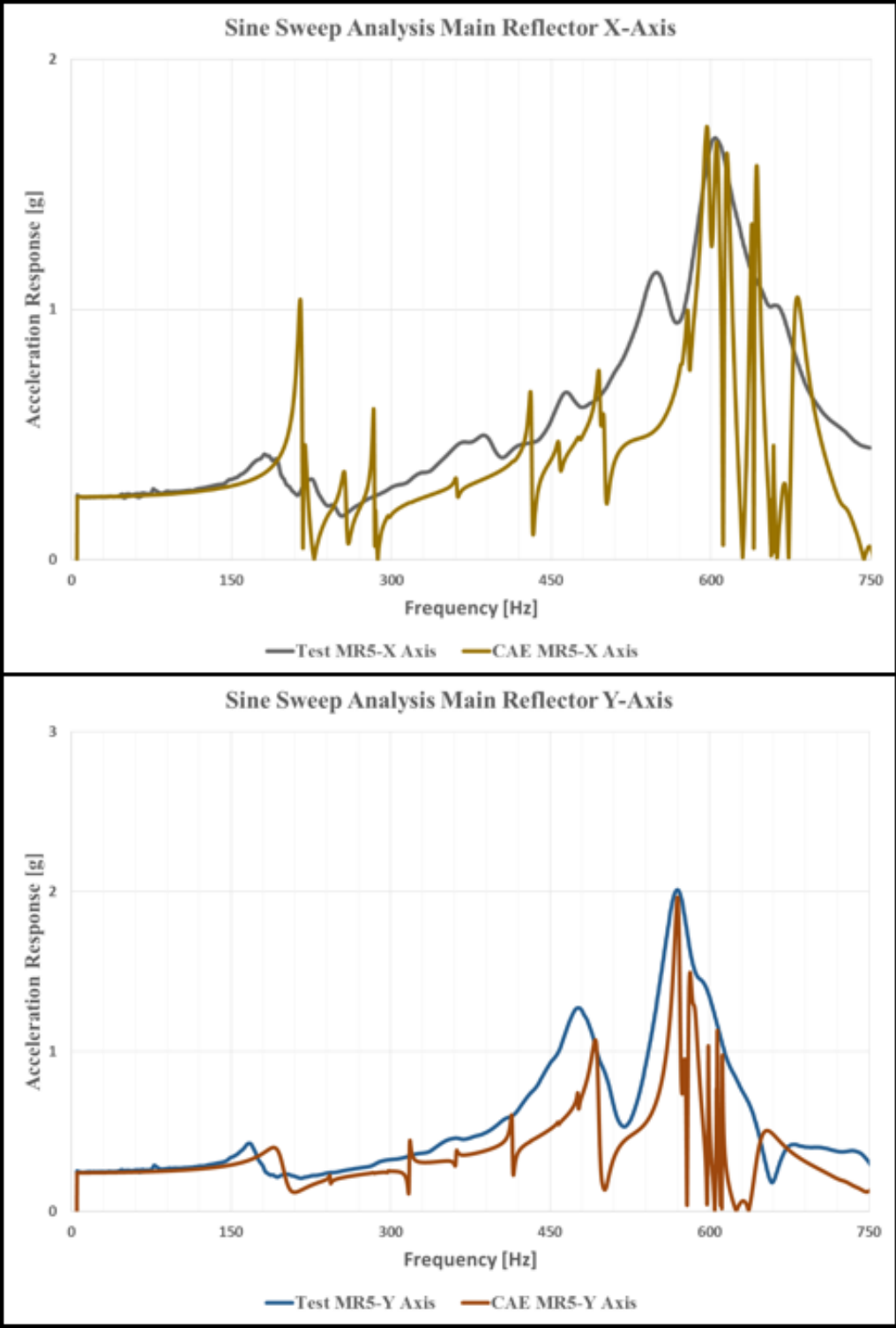


Figure 2.24. Comparison Plot of MR5-X in X-excitation and MR5-Y in Y-excitation for Main Reflector

In conclusion, as it is shown above, most of the natural frequencies determined by the modal analysis match with those found by the test. The errors of these natural frequencies are small. On the other hand, it is critical to note that these comparisons have uncertainty because the lack of modal tests prevents the comparisons of the mode shapes. Thus, in order to make better comparisons not only the natural frequencies are compared, but also corresponding mode shapes. Furthermore, the comparisons of the frequency response analysis and the responses obtained from the sine sweep tests have an acceptable agreement at natural frequency locations. On the other hand, matching the amplitude data as well as matching the widths of the resonance peaks were problematic. The problem seems to be arising from damping ratios and the nature of the damping in the composite material which is likely not suitable for modeling using viscous damping ratios. The second point which should be discussed is related to the step size of the analysis (0.25Hz). In order not to miss the peaks of the tests, 0.25Hz is used as step size of the frequency response analysis. This causes some sharp curves which can be observed from the figures. To sum up, although there are some deficiencies about these comparisons, the modal analysis and frequency response characteristics are somewhat matched. The acoustic test results will help us evaluate if the analysis results are good enough to estimate the structural response due to acoustic loading.

## CHAPTER 3

### VIBRO-ACOUSTIC TESTS AND FEM ANALYSIS OF THE ANTENNA

#### 3.1. Vibro-Acoustic Tests

In this chapter, vibro-acoustic tests and corresponding finite element analysis will be discussed. The main reasons and the importance of these tests were introduced at the Section 1.4. In summary of the related chapter, one of the main aim of the acoustic test is to make sure that the space structure can withstand acoustic loading which will be endured during lift-off. The test is applied in the broadband frequency range as it is mentioned in the book “*Handbook of Space Technology*” [26], which is similar to the frequency distribution of the actual acoustic loading during lift-off.

##### 3.1.1. Background Information about the Vibro-Acoustic Tests

Background information about the vibro-acoustic tests will be introduced in this section. The test procedure consists of two principal parts. Firstly, the fixture of the antenna with the spacer of the acoustic room is tested by itself in order to prove the pressure level homogeneity of the chamber over the domain within the tolerance limits. It is aimed that the antenna has to be protected from the undesired and uncontrolled sound pressure levels (SPL) especially from pressures higher than the tolerance limits. After the verification of the SPL profile in the empty reverberation chamber, the acoustic tests with the antenna is performed. The target SPLs are given via Table 3.1 where frequency means the center frequency of the corresponding octave band.

Table 3.1. Acoustic Loading

Frequency [Hz]	31.5	63	125	250	500	1000	2000	4000	8000	OASPL
SPL [dB]	133	137	139	141.1	137.1	130.8	126.8	123.3	119.3	145.6

As it was expressed in related sections, the sound pressure levels are determined by the launcher of the satellite, therefore, the test levels depend on the launcher's companies. The requirements of the project's antenna's qualification level SPL at octave band are listed in Table 3.1. In the world, there is a limited number of space rockets like ATLAS V, DELTA IV, FALCON 9 and ARIANE 5 from different countries. The test profiles for each of the rocket are different. Turkish space program uses an acoustic test profile enveloping all of these launchers in order to qualify the antenna in case of usage of any launcher. The SPL profiles of these rockets are obtained from their user manuals and compared to the current profile as it can be shown in Figure 3.1[18, 37, 38, 39]. It is obviously seen from the figure that considered test levels are much higher than the others. This conservative approach in the project makes the acoustic tests be more complicated and possibly more destructive. In other words, any specimen tested under this project's acoustic test conditions is qualified for use in any launcher.

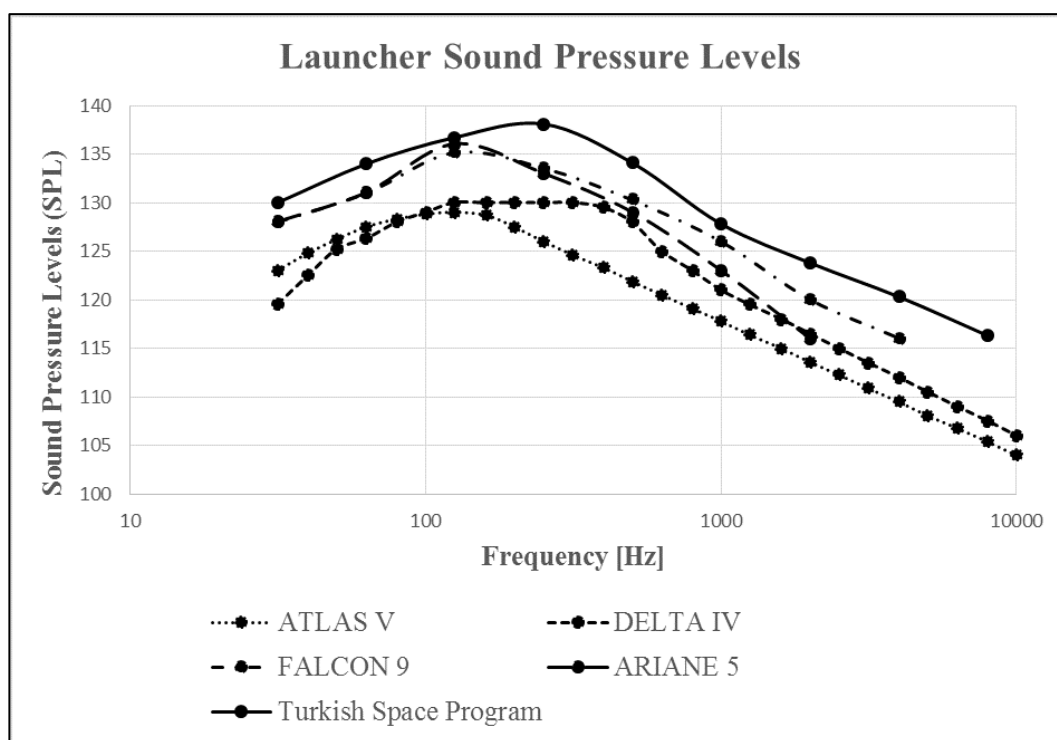


Figure 3.1. SPL Comparisons of Different Launchers with the Turkish Space Program [18, 37, 38, 39]

Test durations depend on the type of the test which is qualification level or flight level. It is accepted by the handbook of the ECSS, the test duration is 120s for the qualification level while it is 60s for the flight/acceptance level [18].

As it is explicitly stated in the handbook [18], the sequence of the acoustic tests is composed of low level, intermediate (acceptance/flight) level, qualification level and finally low level tests again. So three acoustic tests with different levels (low, medium and qualification) are performed to the only fixture and spacer without an antenna. After these tests, the antenna is placed to the fixture on the floor of the chamber and four levels of acoustic tests are performed. These levels are first (pre) low, medium, qualification and second (post) low level. The test sequences with time durations are summarized in Table 3.2. Although the low level test can be seen as unnecessary since they seem as non-destructive, they are critical to show the damages or deficits on the test specimen.

Table 3.2. Vibro-Acoustic Test Sequence

Test	Test Level	Duration of Test [s]
Only Fixture	Low Level (LL) (-8dB)	120
Only Fixture	Medium Level (ML) (-3dB)	30
Only Fixture	Qualification Level (QL) (0dB)	60
Antenna	Pre Low Level (Pre-LL) (-8dB)	120
Antenna	Medium Level (ML) (-3dB)	30
Antenna	Qualification Level (QL) (0dB)	60
Antenna	Post Low Level (Post-LL) (-8dB)	120

### 3.1.1.1. Reverberant Chamber and Test Set-Up

The vibro-acoustic tests were performed in the reverberant chamber of Turkish Aerospace Industry (TAI)'s Space System Assembly Integration and Test Center (AIT). The reverberant chamber is able to reach a maximum overall sound pressure level of 156dB over the frequency range of 25-10000 Hz. The dimensions of the

chamber are the width of 9.5m, depth of 7.9m and height of 12.6m [43]. The excitation is provided by converting the liquid nitrogen into gaseous form by using an electronic controller. The chamber is isolated from the building and floor by using spring-damper systems against any vibrations or disturbances coming from outside.

Since the chamber's walls are highly reflective, the test levels cannot be easily controlled near the walls, floor or ceiling. Due to incident and reflected sound waves, near the walls the sound pressures are generally doubled. To prevent floor effects the test specimen is above from the floor level by 2m with a spacer and whole testing fixtures and set-up are positioned exactly at the center of the room during the tests. By this spacer, it is guaranteed that the test specimen is positioned at a location where the sound field is diffuse. The spacer is positioned on the center of the chamber's floor with pneumatic isolators. ECSS standard [15] puts a regulation about decoupling the test sample from the floor like Wickramasinghe and his colleagues draw attention to this issue in his article [17]. During the tests, these regulations and cautions are carefully considered.

Usage and positioning of microphones is another critical issue at acoustic tests since they are used as the feedback system of the chamber. The input of the sound pressure sources is controlled by this feedback from the microphones. If the pressure level drops to a value near to a lower tolerance limit inside the chamber, the horns increase the sound pressure inside the room, or vice versa. The numbers of the microphones are also critical as well as their positions. Different numbers of them are preferred for different tests. To begin with Ley and his team suggests that 4-12 microphones are acceptable for the acoustic tests [26]. Hughes shows that NASA uses 8 microphones while Wickramasinghe uses 6 microphones 0.6m away from the test specimen [16, 17]. According to the usage of microphones ECSS's handbook suggests that "*Control microphones are placed around (above and below) and with sufficient distance of the test item.*" ... "*The applied levels are defined as the mean of the control microphones SPL's. (min 6). The minimum distance of the microphones from the test articles is 1 meter.*" [18]. Therefore, for the antenna's acoustic tests considered in this thesis, this

rule is exactly followed similar to the literature studies. During the acoustic tests, 8 microphones away 1m from the antenna are used. 4 of them are put at height of 2m which is the level of bottom of antenna. The rest of the microphones are placed at the 4m which is the top level of the antenna. Feedback system uses the averaging of the 8 microphones data computed according to the following equation provided by Wijker [27]:

$$SPL_{avg} = 10 \log \left( \frac{1}{n} \sum_{k=1}^n 10^{\frac{SPL_k}{10}} \right) \quad (20)$$

Furthermore, the dimensions of the reverberant chamber are another important issue and should be checked and compared to similar studies. So, the AIT's reverberant chamber dimension is compared other's in the literature. 6.9mX9.75mX8.0m and 11.4mX14.5mX17.4m are two important examples provided in [16, 17] while AIT's chamber's dimensions are 9.5mX7.9mX12.6m. Thus, AIT's chamber might be accepted as valid since their dimension are close to others. The sound pressure is provided via 3 different horns and speakers. Up to 10 kHz the horns whose cut-off frequencies are 25 Hz, 40 Hz and 50 Hz. The acoustic excitation is provided by directly these horn below 750Hz; on the other hand, above this frequency, the excitation (SPL) is obtained by the speakers and the gaseous nitrogen inside the chamber. Controlling the sound pressure level above 750Hz has troubles because of lack of control in gas and speakers.

A 100kg rigid fixture is used to connect the antenna and the spacer of the chamber. The fixture (orange) is designed such that it is not affected by the acoustic loads. Figure 3.2 shows the reverberant chamber with microphones, speakers, horns and test specimens with spacer and fixture.

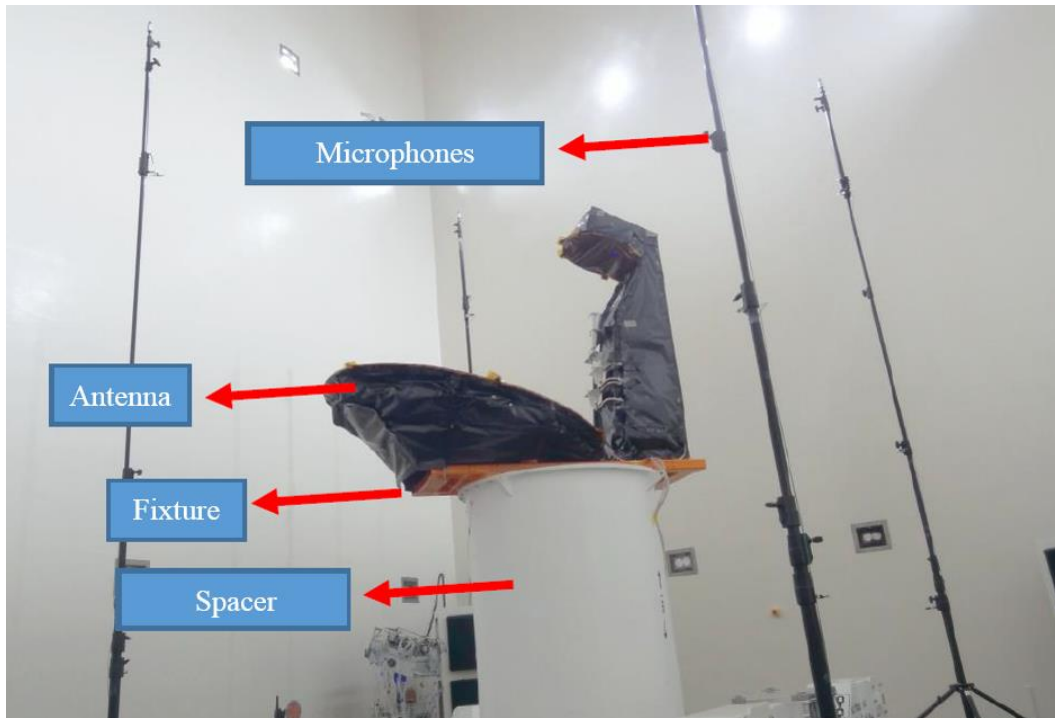


Figure 3.2. Reverberation Chamber and Test Setup

Acceleration responses of the antenna and the fixture are measured by 35 accelerometers. Although the accelerometers can take 3-axis measurements, at some large surfaces mono-axis measurements are taken as Hughes suggests [16]. Two 3-axis accelerometers are used to collect the structural responses of the test fixture under the acoustic loading. They are positioned at the edges of the fixture aligned with the tower and main reflector, as shown in Figure 3.3. Eight and nine of them are peripherally used for small and large reflectors, respectively. In addition to accelerometers on the main reflector, five are put to the ribs under the reflector in order to obtain results from flat surfaces. Finally, nine accelerometers are positioned over the tower's critical points while two of them are used on the feed chain (Figure 3.4).

Furthermore, the measurement of the responses is collected at the time domain and simultaneously converted to spectral domain. 4340 data points are recorded at every 2.95 Hz. The frequency range is 20-8000 Hz. Table 3.3 overviews the data acquisition terms of the acoustic test.

Table 3.3. Overview of the Data Acquisition of Acoustic Test

Frequency Range	20-8000 [Hz]
Frequency Resolution	2.95 [Hz]
Total Number of Data Points	4340
Number of Microphones	8
Height of the Microphones	2 m (4 mics) , 4m (4 mics)

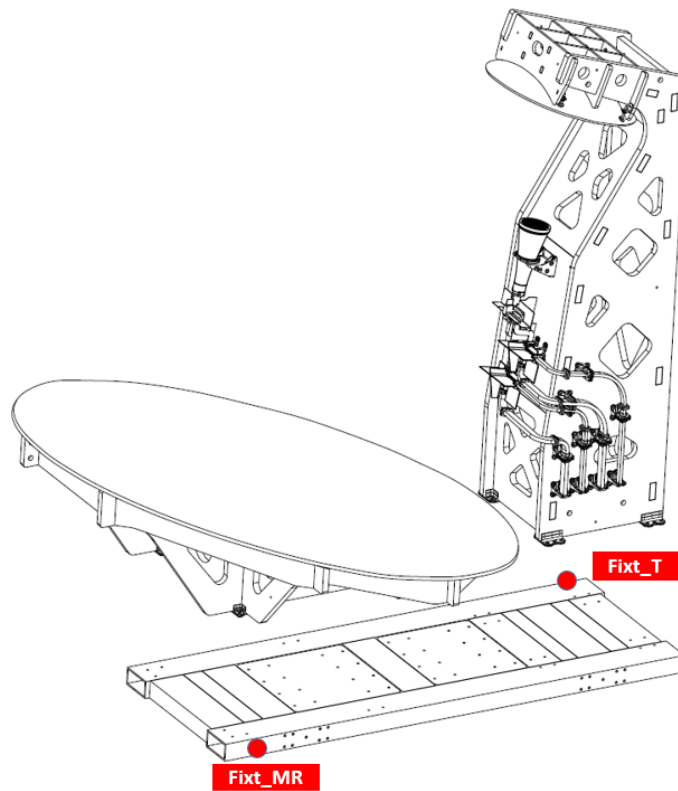


Figure 3.3. Accelerometers on the Acoustic Test Fixture

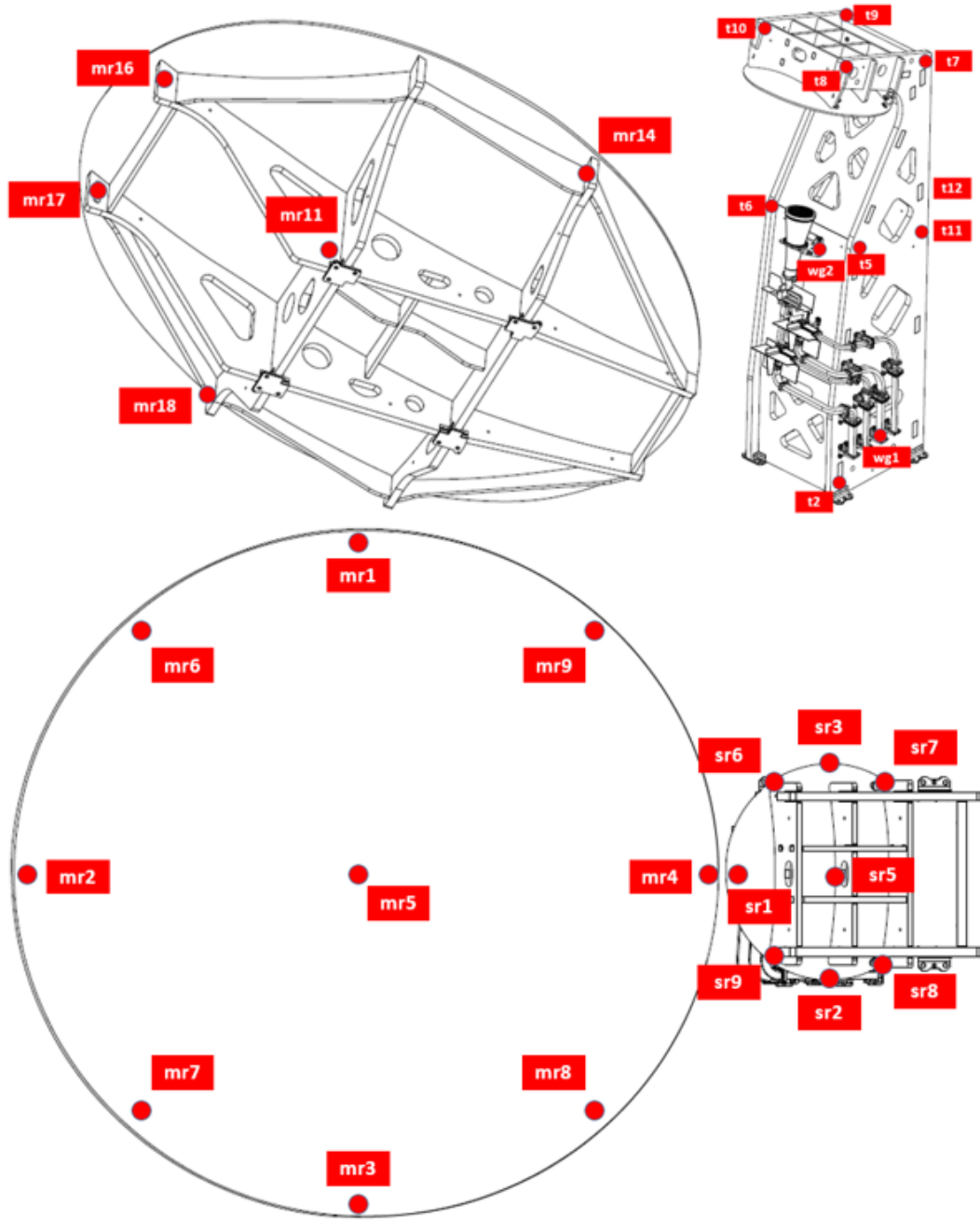


Figure 3.4. Accelerometers of the Acoustic Test

### 3.1.2. Vibro-Acoustic Tests of the Fixture

In this subsection the tests of fixture placed on the spacer, without antenna, of the room will be presented with their results of microphones and structural responses. The fixture is torqued to the spacer by using 12 bolts (M12) on the periphery of the spacer. ECSS' handbook summarizes the importance of the empty room acoustic tests as “Prior to the test of the article, empty chamber runs are performed (without the test article), in order to establish the settings of the control equipment and to achieve the levels.” [18]. Low, medium and qualification level tests run for this sequence. Post low level test is not seen as necessary since it is assumed that the fixture would not be affected by the acoustic loading. The sound pressure levels at the octave band are given as in Table 3.1. In addition to this table, the upper and lower tolerances were presented via Table 1.4. Figure 3.5, Figure 3.6 and Figure 3.7 show the obtained test levels with corresponding reference level and the limits.

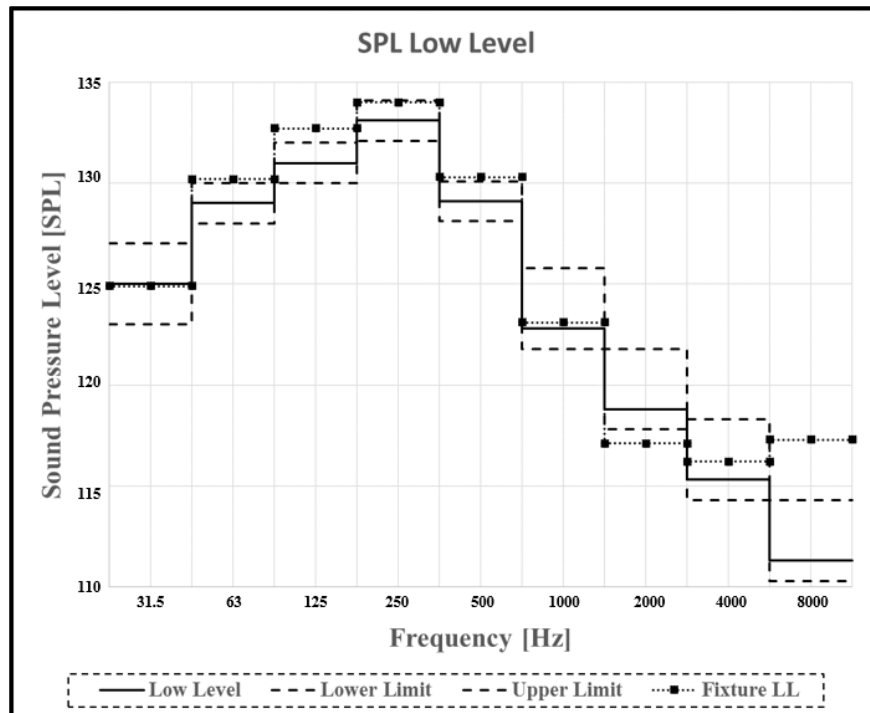


Figure 3.5. SPL of Low Level Acoustic Test of Fixture

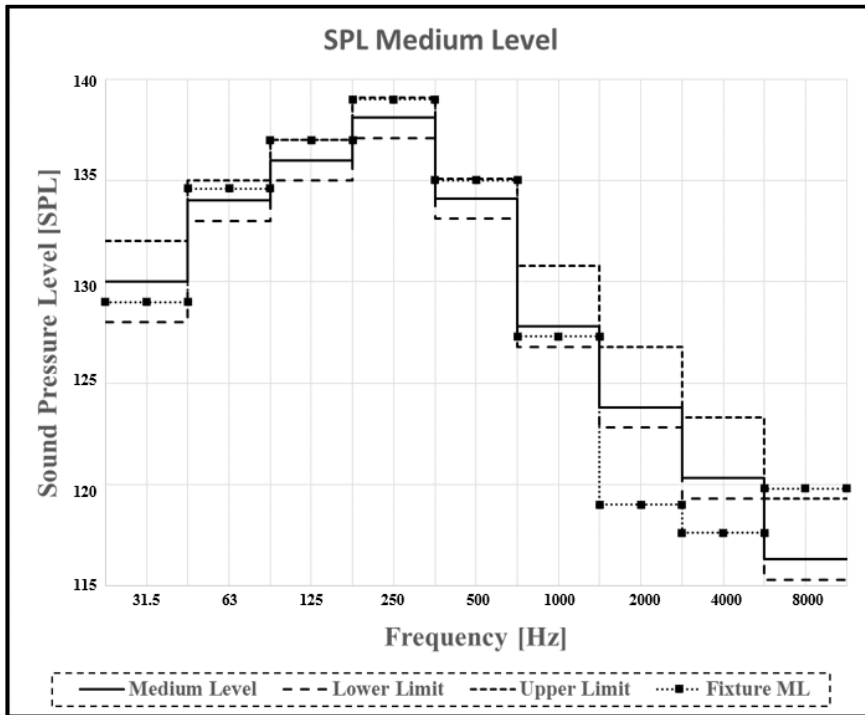


Figure 3.6. SPL of Medium Level Acoustic Test of Fixture

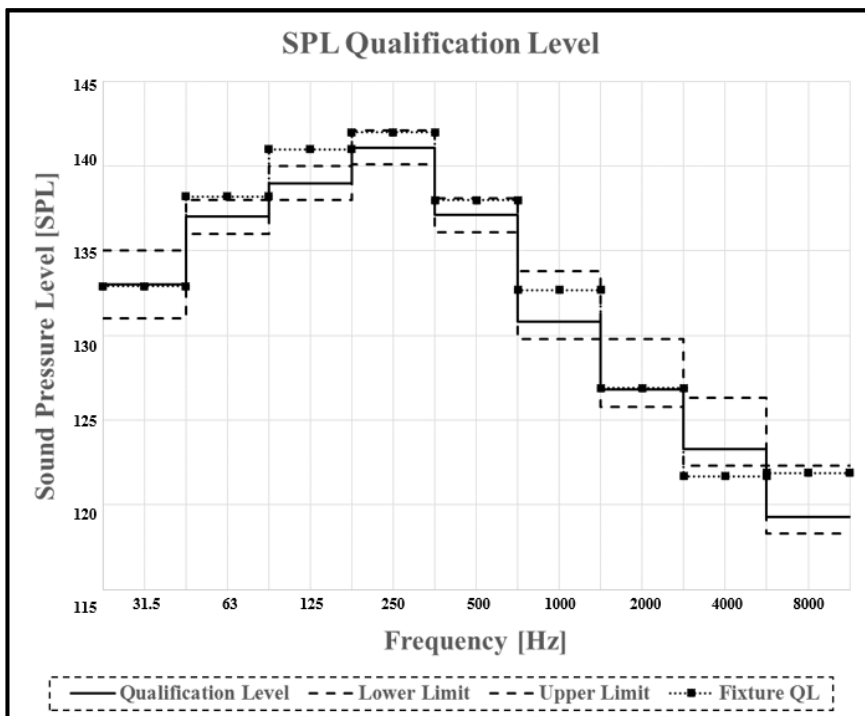


Figure 3.7. SPL of Qualification Level Acoustic Test of Fixture

According to figures, it can be interpreted that at medium and especially low level acoustic tests, it is difficult to keep the sound pressure inside the tolerance limits at the low frequency values. Hughes explains the possible challenges to get desired SPLs at low level acoustic tests. According to him, background noise and non-linearity of the noise reduction probably distort the test level [16]. Since the test levels are small for the low level tests and at the low or very high frequencies, the environment is very sensitive to these noises and reductions of noise.

Another interpretation of these tests is related to the responses of the fixture. Figure 3.8 illustrates the fixture's response under the qualification level test without the antenna along 3-axes. Since the other test levels (intermediate and low) cause much smaller responses than these, those are not presented. From the figure, both of the plots show that maximum responses of the fixture are seen at the low and especially mid-levels. For example, while there are specific peaks between 40Hz and 100Hz, the maximum responses are seen between 100Hz and 400Hz. These high response frequencies depend on several aspects such as the natural frequencies of the fixture-spacer assembly, their boundary conditions, the acoustic domain and the SPL at the corresponding frequencies. According to acoustic test results, maximum peaks occur at 26Hz, 29Hz, 42Hz, 56Hz, 88Hz and 117 Hz, so on. The frequency change of the maximum responses should be considered carefully, because the improper selection of the test fixture may cause over-testing of the specimen as Calvi et. al. states [18]. On the other hand, the fixture is thought to be not responsible for this change since it is stiff and does not have large surfaces. Probably the spacer and its boundary condition which is the pneumatic isolators are responsible for this change and this difference has to be carefully considered, especially in the antenna's test.

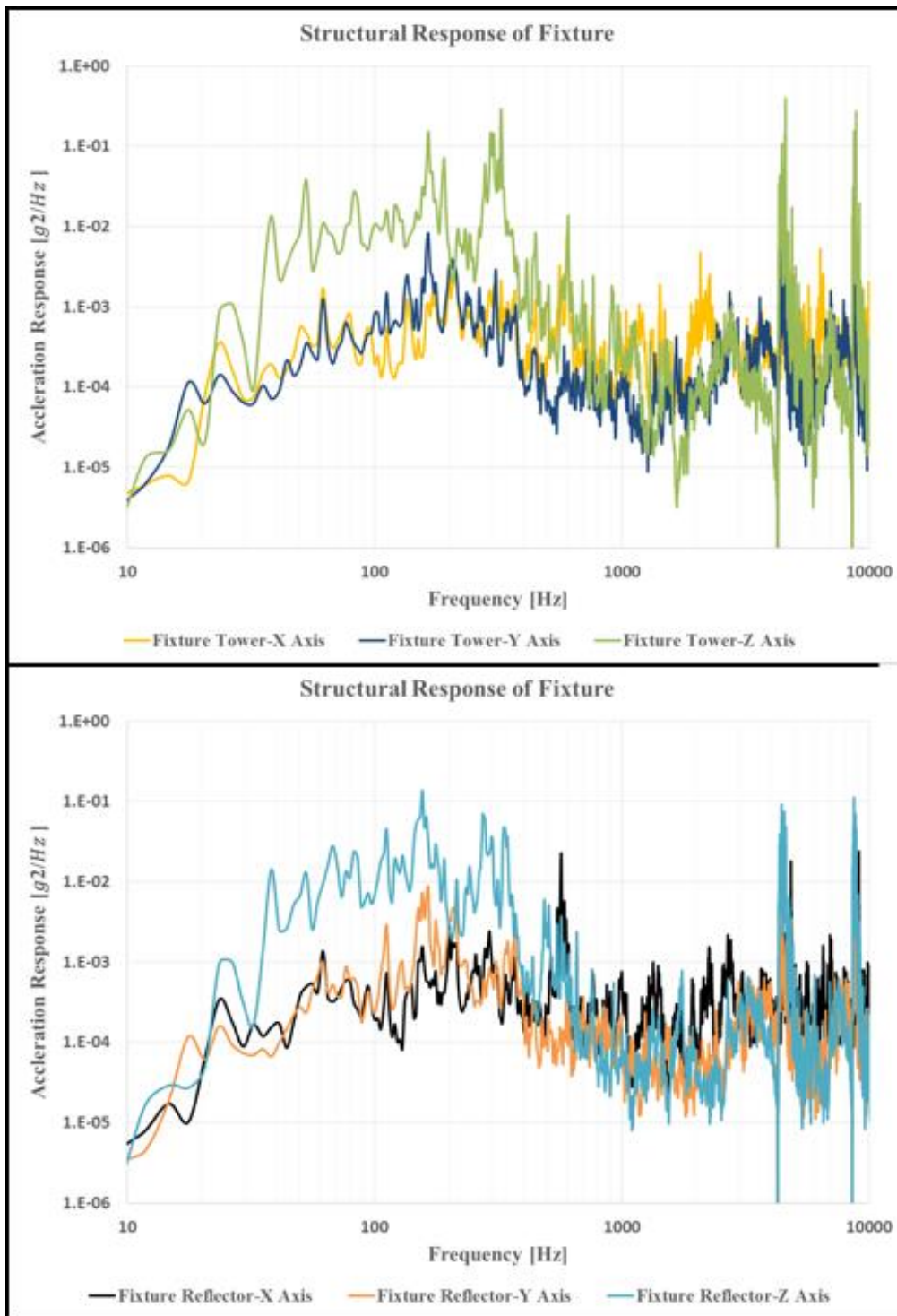


Figure 3.8. Structural Responses of the Fixture Under Acoustic Loading

Furthermore, the magnitudes of the responses could be considered. It can be concluded that although the responses of fixture are so small especially in X and Y axes with magnitude  $0.001g^2/Hz$ , the responses at Z-axis is a little bit higher at maximum  $0.2 g^2/Hz$ . Although these results seem small, they may cause some problems for the tests because it is the fixture and should be as rigid as possible; in other words, it should be so stiff and the structure should not be affected by it. Responses at the other two axis are almost one-tenth of Z-axis. The possible reason for the high response of the Z-axis may be the position of the horns. The horns are at the ceiling of the chamber and vibrate the nitrogen directly in the Z-axis. Another possible output of this test is that after 400Hz, the structural responses dramatically drop and the analysis up to this limit may be enough. Additionally, the peaks around 4500Hz and 8500Hz should be carefully examined for the antenna tests, but it is evaluated that it is measurement or post-processing error.

### **3.1.3. Vibro-Acoustic Tests of the Antenna**

In this subsection, acoustic tests process for the antenna and the test results will be presented. The acoustic test series of the antenna is composed of four tests, e.g. pre-low, medium, qualification and post-low level. For the medium level (-3dB), acoustic environment of the launcher is simulated although the requirement of this antenna is 3dB more than medium level called as qualification level (0dB) which is a reference of the test series. In addition to these, low level (-8dB) tests are performed. Although qualification and medium levels are specified, some different approaches exist for selection of low level tests. For low level tests; literature suggests -6dB or -8dB [15], Wickramasinghe takes -10dB [17]. Hence, -8dB is accepted as a low level for the acoustic test series.

After the fixture's acoustic tests, the antenna is bolted to the fixture via 26 bolts by using the torque value used in the vibration tests. Using the same torque value is important in order to obtain the same stiffness value since different torque value may

change the behavior of the structure. After checking all the criteria, the tests are performed.

It is important to provide the required and obtained sound pressure levels in order to show the validity of the acoustic tests. From Figure 3.9, Figure 3.10 and Figure 3.11 it can be concluded that up to 1000Hz almost all sound pressure levels are inside the tolerance levels at each octave band. On the other hand, after 1000 Hz, the acoustic environment cannot be maintained within the tolerance limits at some octave bands. This phenomenon can be explained that up to 1000Hz, the horns are responsible for the acoustic pressure; however, after this threshold speakers and the gaseous nitrogen provides the pressure level in the experiment. For these tests, this unsatisfactory SPL at high frequencies is accepted since at these octave bands the sound pressure levels are too small. Since the most important frequencies are below 1000Hz, these test profiles are accepted.

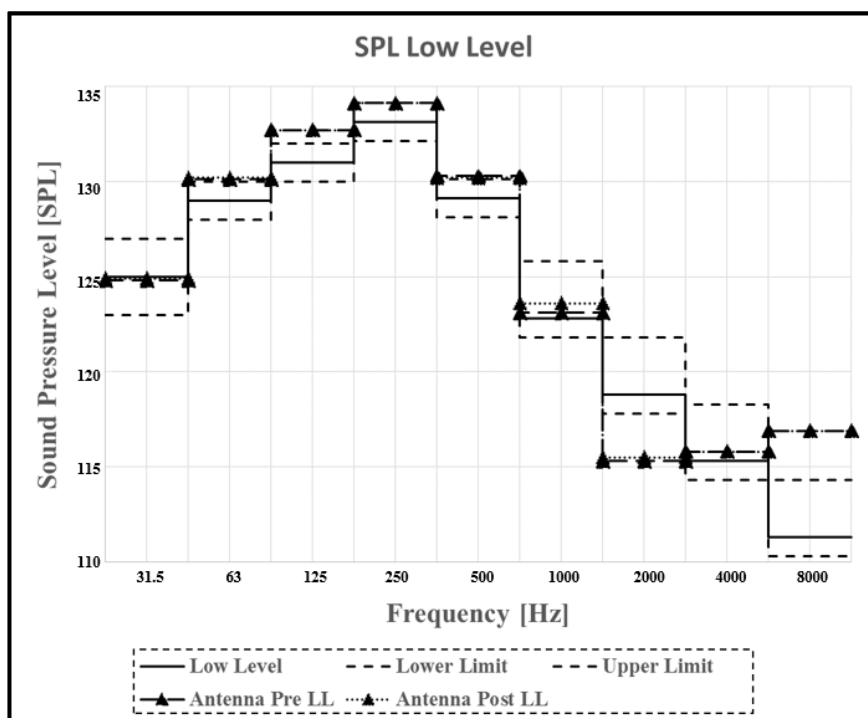


Figure 3.9. SPL of Low Level Acoustic Test of Antenna

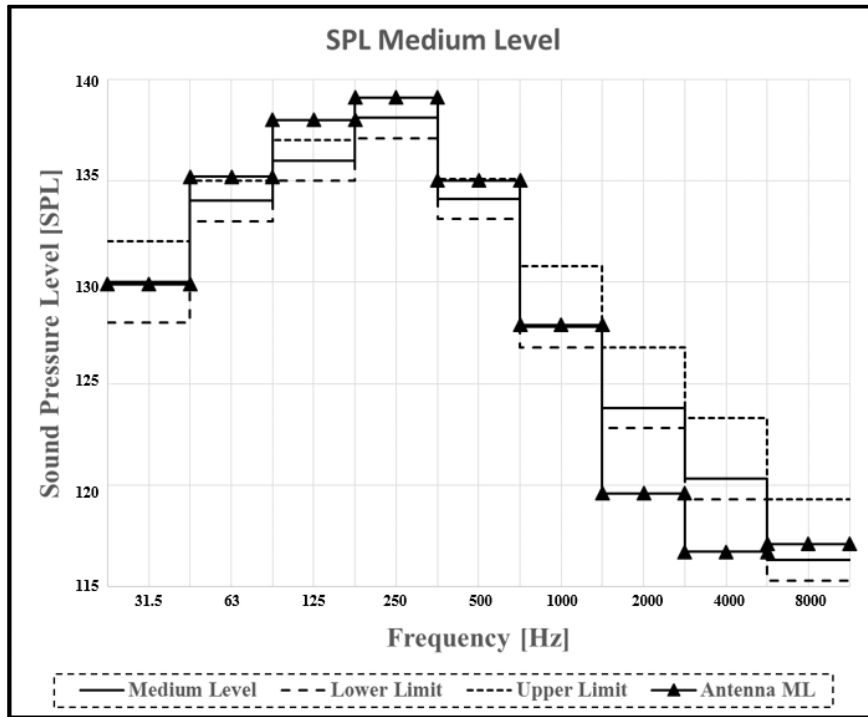


Figure 3.10. SPL of Medium Level Acoustic Test of Antenna

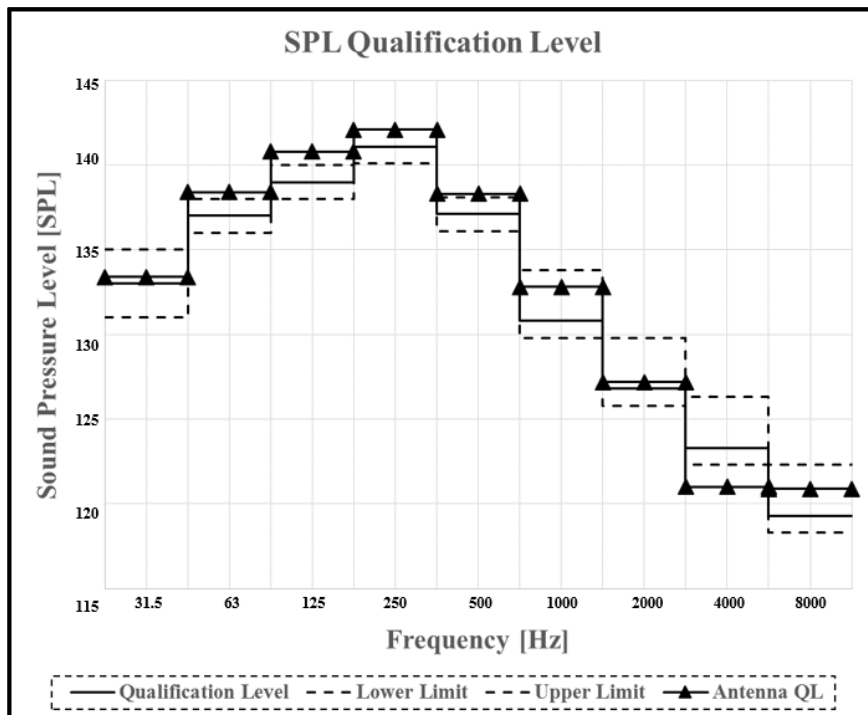


Figure 3.11. SPL of Qualification Level Acoustic Test of Antenna

Moreover, the microphone data present a valuable opportunity to show the absorption effect of the antenna. The only difference between these tests with antenna and the tests presented in the previous section which is the acoustic test without antenna may give information about antenna's effect as shown in Figure 3.12. It is obviously seen that the SPL data of the antenna test symbolized by triangles are smaller than the SPL of the fixture test shown by squares except for the two frequency bands. Despite the equal inputs of two tests, the existence of such difference shows that the antenna has some absorption effect which is more pronounced at the higher frequencies.

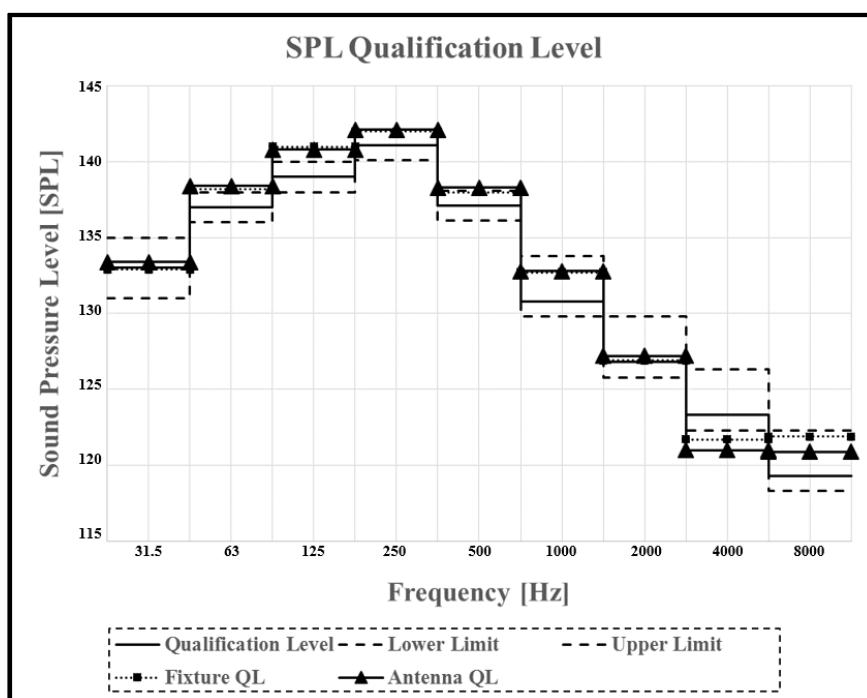


Figure 3.12. Comparison of Fixture and Antenna Tests at Qualification Level

Moreover, interpreting the structural responses of the vibro-acoustic tests is one of the most important issues for this thesis. Since the most destructive load level is qualification level, its results are handled, none of the other tests' structural response results will be provided. The first aim is to determine the part of the antenna with maximum responses which is expected to be the tip of the main reflector because of its large and light structure. In order to show that, the highest ten responses of the

accelerometer results will be presented via Table 3.4 where N is normal direction of the surface and Z is the global Z-axis.

Table 3.4. *Acoustic Test: 10 Maximum Response Values, Corresponding Frequencies and Accelerometer ID's*

<b>Accelerometer</b>	MR2-N	MR6-N	MR14-Z	MR4-N	MR3-N
<b>Frequency [Hz]</b>	268.44	212.39	212.39	212.39	215.34
<b>Response [<math>g^2/Hz</math>]</b>	20.67	16.80	13.35	10.95	10.62
<b>Accelerometer</b>	MR9-N	MR8-N	MR16-Z	SR1-N	MR17-Z
<b>Frequency[Hz]</b>	241.89	283.19	259.59	132.74	268.44
<b>Response [<math>g^2/Hz</math>]</b>	8.30	7.27	5.01	4.48	4.30

The most important interpretation of the table is that the results verify the literature information that the most effected part under acoustic load is the large reflectors. Six and three of the ten results are the points on the main reflector and its supported structure just under of it. Only the last point is on the sub-reflector. The table is used to determine the most critical region or accelerometer point of the main reflector. Hence, the most sensitive point of the main reflector is the MR2 which is the very edge of the main reflector as it is expected. The reason for this is that point is at the edge of large and light reflectors. In addition to this, the edge is not supported by the support structure and it is accepted as the most critical point of the main reflector. The amount and corresponding frequency of the maximum response are 20.67  $g^2/Hz$  and 268.44 Hz. Another interpretation from can be taken as all of the main reflector's responses are focused on between 212Hz and 283Hz while the sub-reflector's maximum response is seen at 132.74Hz. Table 3.1 shows the largest two SPL are 141.1dB and 139dB at the frequency bands centered by 250Hz and 125Hz, respectively. The maximum responses of the main reflector can be explained by this maximum SPL and the modes at these frequencies. 141.1dB is applied to the octave frequencies between 177Hz and 355Hz which covers the 212Hz-283Hz. On the other hand, the tower and the sub reflector has the maximum response outside this maximum

input pressure region. Its maximum response occurs at 132.74Hz where it is the second highest input level which is 139dB. It can probably be interpreted that sub-reflector is mostly affected by its mode shapes not the acoustic loading. In order to show this comparison, some of the critical points of the main reflector, sub-reflector and tower are presented in Figure 3.13 where QL means Qualification Level. From the figure, the sub-reflector and tower responses are much smaller than the main reflector over almost the whole frequency band. The sharp peaks of the tower and sub-reflector occur at the same locations.

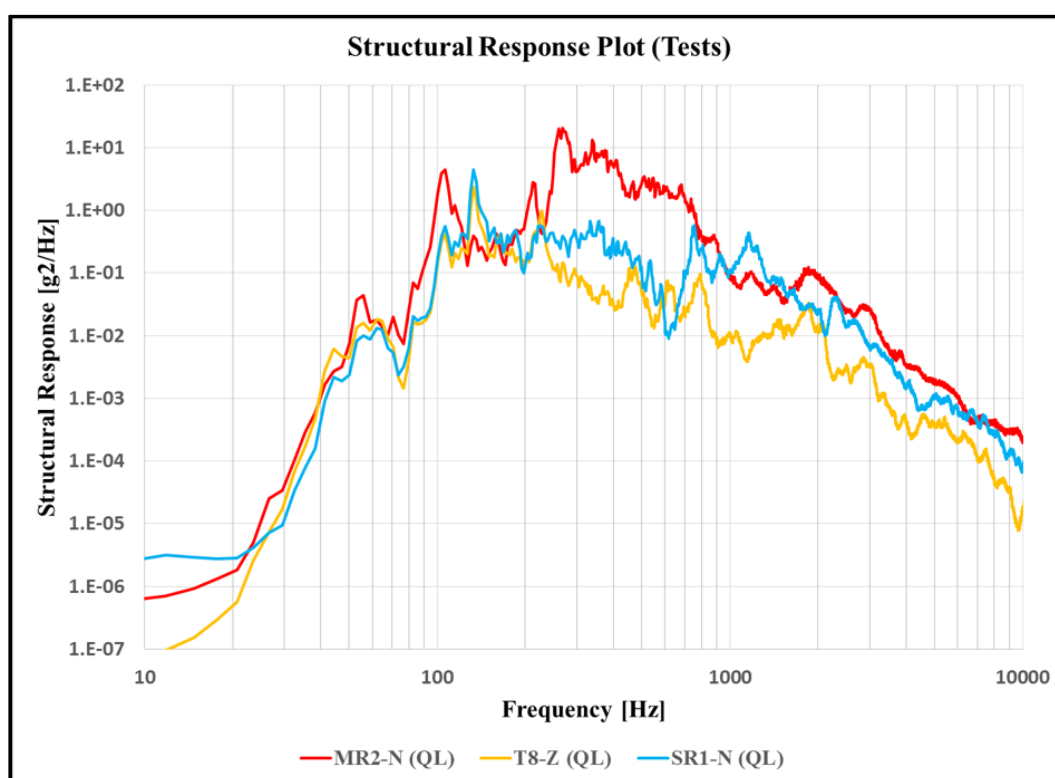


Figure 3.13. Comparisons of Critical Accelerometers of Tower, Main Reflector and Sub Reflector

In addition to these comparisons, the critical locations which are MR2, T8-Z and SR1 of each sub-assemblies should be examined independently. These accelerometers' maximum responses will be presented via Table 3.5. The maximum responses of this accelerometer at 2.54, 8.21, 20.67 and 4.32 g<sup>2</sup>/Hz for the LL01, ML, QL and LL02 tests, respectively.

Table 3.5. Maximum Responses [ $g^2/Hz$ ] of MR2, T8-Z and SR1 Accelerometers at Each Test

	Pre-Low Level (LL01)	Medium Level (ML)	Qualification Level (QL)	Post-Low Level (LL02)
<b>MR2 [<math>g^2/Hz</math>]</b>	2.54	8.21	20.67	4.32
<b>SR1 [<math>g^2/Hz</math>]</b>	0.96	2.44	4.48	0.91
<b>T8-Z [<math>g^2/Hz</math>]</b>	0.75	1.29	2.34	0.72

Focusing on the specific accelerometers results begins with MR2 accelerometer which is the tip of the main reflector. Firstly, Figure 3.14 shows the acceleration response of it throughout the whole frequency domain. This figure includes all results of the pre-low, medium, qualification and post-low level tests. As it is seen from the plot, after 600 Hz, the structural responses drastically drop; therefore, although the vibro-acoustic tests are performed up to 10,000 Hz, the frequency range up to 750Hz for the corresponding analysis is enough for the discussing its effects on the structure.

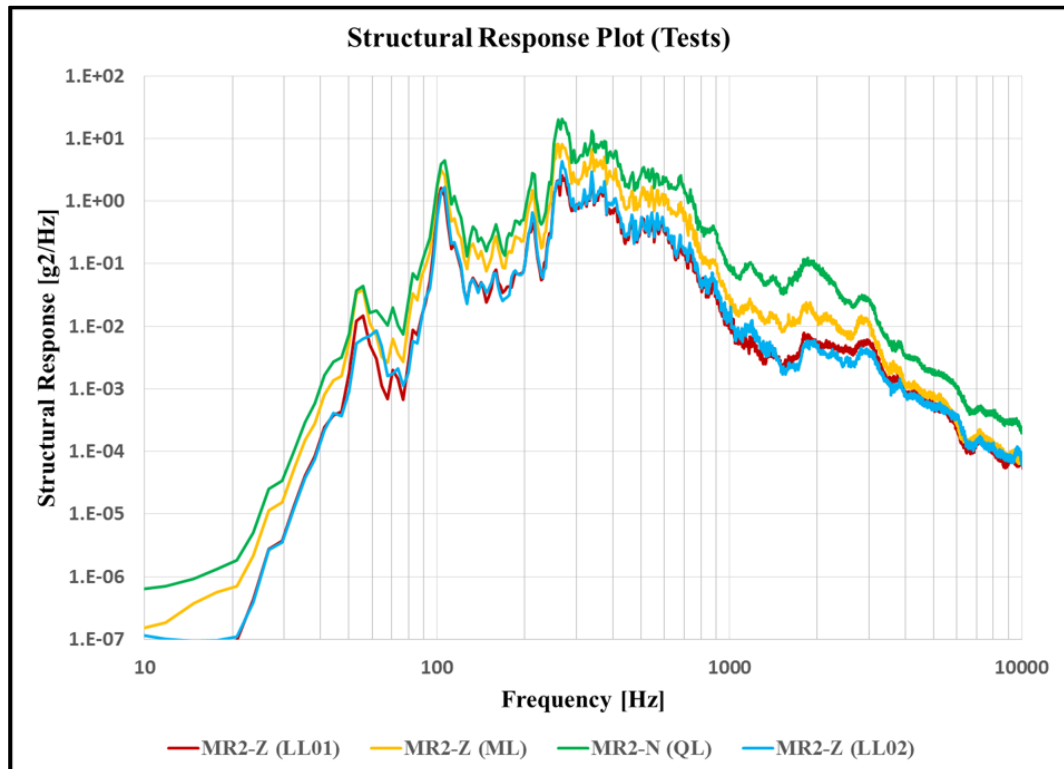


Figure 3.14. PSD Responses of MR2 of Different Tests

Other response comparisons against different test levels are made for tower's and sub-reflector's most significant accelerometers in the critical direction (T8-Z and SR1). On the other hand, Table 3.4 does not contain all the 10 accelerometers with the highest response measurements for these two sub-structures because the main reflector dominates the table. Therefore, since the largest responses of both tower and sub-reflector are smaller than the main reflector and they are not seen in the previous table, their accelerometers' maximum results are presented in another table which is Table 3.6. As it can be from these tables, the values of the tower and sub-reflector are much smaller than the main reflectors'. As it can be seen from this table, the frequency of 132.74Hz dominates the table for both sub-reflector and the tower. Then the second common frequency is 533.93Hz which both are valid for sub-reflector. In addition to these, some peaks are seen at 106.19Hz, 162.24Hz, and 471.98 Hz.

Table 3.6. *Acoustic Test: 10 Maximum Response Values of the Tower and Sub-Reflector, Corresponding Frequencies and Accelerometer ID's*

<b>Accelerometer</b>	SR1-N	SR6-N	SR2-N	SR8-N	SR3-N
<b>Frequency [Hz]</b>	132.74	132.74	533.93	471.98	533.93
<b>Response [<math>g^2/Hz</math>]</b>	4.48	3.93	3.55	2.96	2.59
<b>Accelerometer</b>	T8-Z	SR5-N	SR9-N	T9-Y	T9-X
<b>Frequency[Hz]</b>	132.74	132.74	153.39	106.19	162.24
<b>Response [<math>g^2/Hz</math>]</b>	2.34	1.14	0.70	0.35	0.19

Table 3.6 presents the maximum responses of the tower. So, the most affected accelerometer is SR1-N where is the tip of the sub-reflector. The response is 4.48  $g^2/Hz$  at 132.74Hz. For the tower sub-assembly the most critical sub-component is seen as sub-reflector as it is expected. For the tower structure, the top edge of it has the most response.

The accelerometer responses of SR1-N and T8-Z over the frequency band up to 10kHz are independently examined like MR2. The maximum responses of these accelerometers are taken from Table 3.5. The maximum PSD responses of the sub-

reflector at each test levels are found by  $0.96g^2/Hz.$ ,  $2.44g^2/Hz.$ ,  $4.48g^2/Hz.$  and  $0.91g^2/Hz.$  Similarly, the responses of the tower at T8-Z are determined as  $0.75g^2/Hz.$ ,  $1.29g^2/Hz.$ ,  $2.34g^2/Hz.$  and  $0.72g^2/Hz.$  Although these response values are similar to each other in magnitude and frequency, they are too small compared to main reflector's results. Additionally, the responses of SR1 and T8-Z accelerometer curves are drawn Figure 3.15 and Figure 3.16 corresponding to each test levels, respectively.

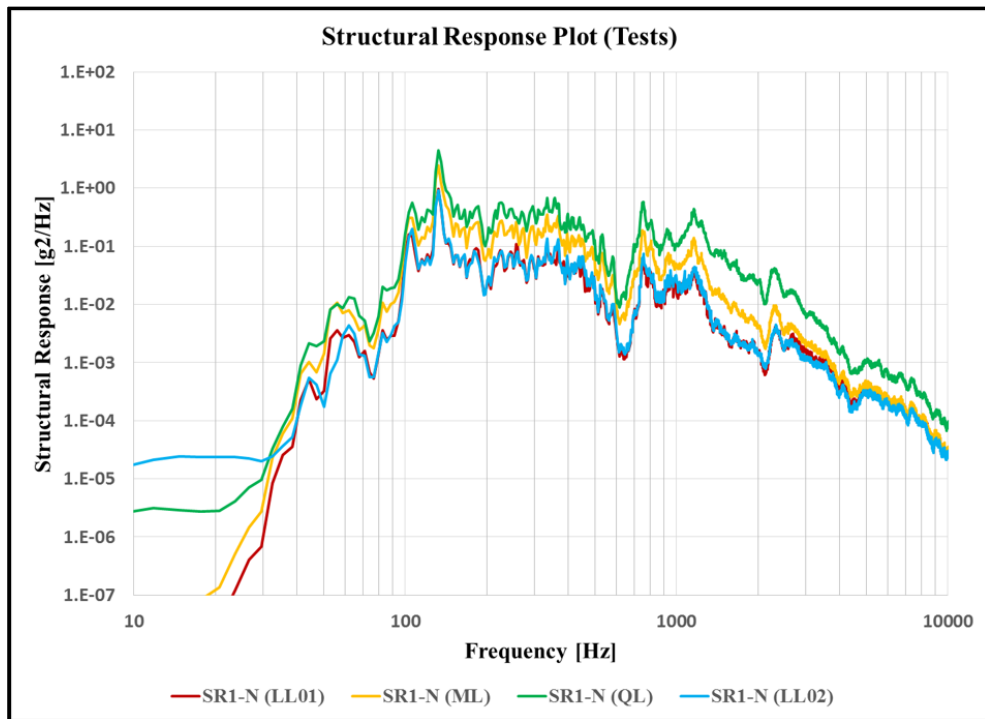


Figure 3.15. PSD Responses of SR1 Under Acoustic Loading

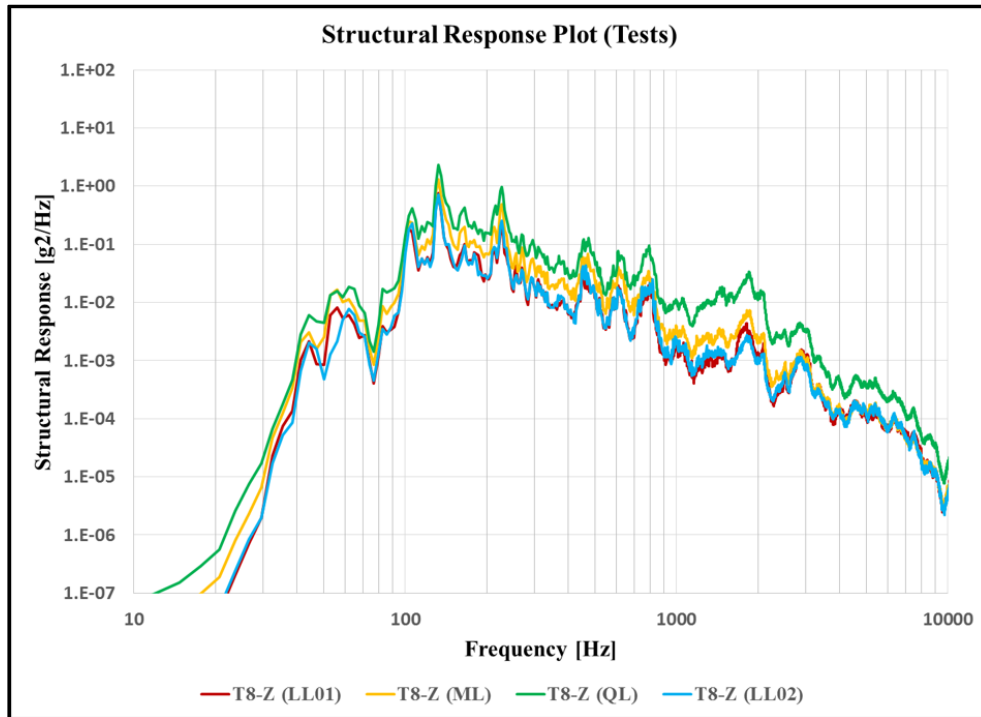


Figure 3.16. PSD Responses of T8-Z Axis Under Acoustic Loading

### 3.1.4. Discussion of the Vibro-Acoustic Tests

In this section, the test results will be discussed. To begin with some of the general knowledge given in literature will be summarized. The test data is highly valuable since it reflects the real situation of the test and the structure. Finally, the effects of the test on the antenna will be shown.

In literature, it is commonly emphasized that the acoustic loading highly affects the large surfaces like reflectors as it was stressed in the Introduction chapter. This statement is verified with the responses shown in Figure 3.17 which includes critical points' structural responses of each subsystem's such as main reflector (MR2), tower (T8), sub-reflector (SR1), fixture (Fixture\_Tower) and feed chain (WG2). The figure clearly illustrates that the highest responses occur at the main reflector (red) throughout the whole frequency range, except a few frequencies. Secondly, the sub-reflector shown with green is more critical compared to the tower or metallic parts.

Then, the tower (orange) is the component with the third highest response. As it is expected the metallic part of the product which is feed chain is the least affected. The reasons of this are their high mass/area ratios. Lastly, the fixture has the minimum responses. Therefore, from this case it can be concluded that the parts with small mass/area ratio are more affected from the acoustic loading as it is explicitly repeated in literature.

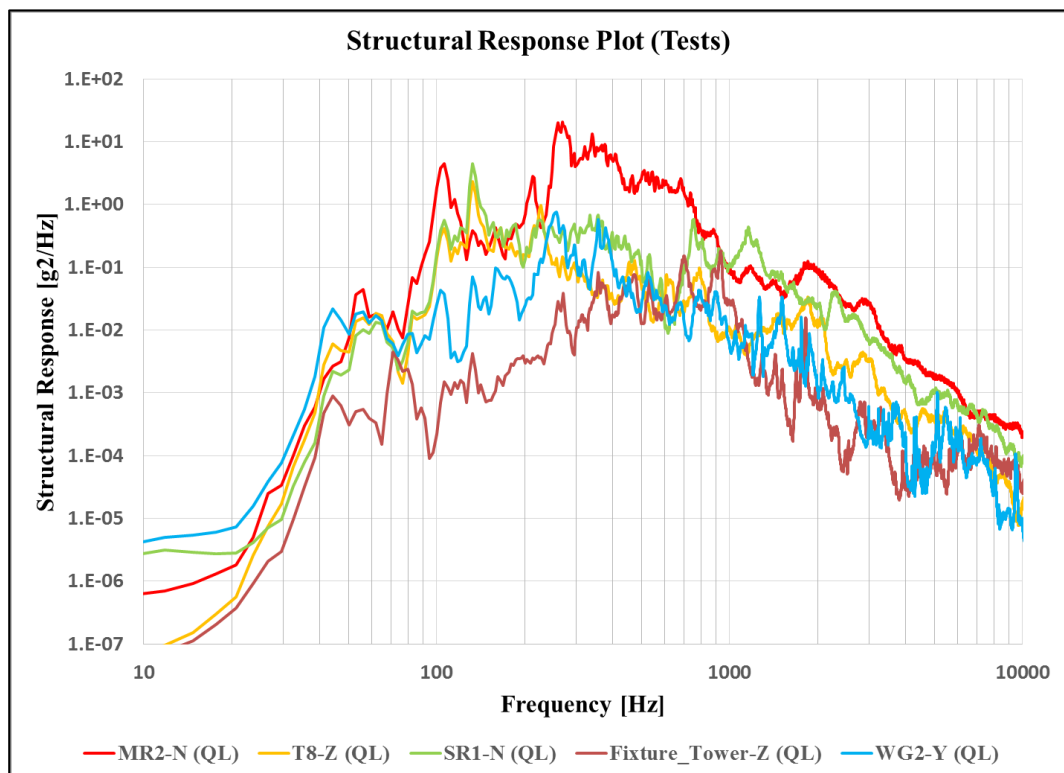


Figure 3.17. Structural Responses of the Accelerometers of MR2, T8, SR2, Fixture and WG2 at the Qualification Test Level

Another output of the acoustic test is that the structural responses of main reflector is maximum between 200-300Hz while sub-reflector and tower have the biggest response between 100-200Hz. Additionally, all curves have common behavior that after 700Hz, the structural responses start to decrease. Most of the 3-axis accelerometers show that the dominant axis against the structural responses is generally Z-axis. The reason of this may be the orientation of the horns which are at the ceiling of the chamber and they are positioned along Z-axis.

The structural response curves under the qualification level test show that the natural frequencies shift (Figure 3.17) compared to sine sweep test results. Although this change is not desired, it is expected because of changing the fixture and boundary conditions. The vibration test results should be reconsidered as presented in the Section 2.1.3. The first three natural frequencies were found as 91Hz, 96Hz and 167Hz for tower while 191Hz, 214Hz and 244Hz for the main reflector sub-assemblies. On the other hand, Figure 3.17 shows the natural frequencies obtained from the acoustic tests as 53Hz, 106Hz and 132Hz for both tower and main reflector.

Table 3.7. Natural Frequency Comparison of the Sine-Sweep and Acoustic Test

		1 <sup>st</sup> natural frequency ( $f_1$ ) [Hz]	2 <sup>nd</sup> natural frequency ( $f_2$ ) [Hz]	3 <sup>rd</sup> natural frequency ( $f_3$ ) [Hz]
Tower	Vibration Test	91	96	167
	Acoustic Test	45	53	106
Main Reflector	Vibration Test	191	214	244
	Acoustic Test	45	53	106

It is important to discuss the change of these natural frequencies. The antenna was bolted directly to the shaker in the sine sweep tests. However, the acoustic test configuration presented in the Figure 3.18 is totally different. At the acoustic tests, the antenna is bolted to the acoustic test fixture and the fixture is connected to a spacer. The assembly is carried to its position on the chamber by using the wheels. After positioned, the assembly is not bolted to the ground or somewhere else, it is placed on the four pneumatic isolators. Therefore, the boundary conditions of the two tests are totally different. The boundary condition was fixed-free for the vibration test while it can be thought of as a very soft spring-damper system for acoustic tests.

In addition to the change of natural frequencies of the tower and main reflector, new natural frequencies are exactly the same for both structures. Although they are different structures and their resonances are expected as different, the possible

explanation about this is again the boundary conditions. It can be concluded that both structures are affected by the spacer. It probably dominates all structural responses.

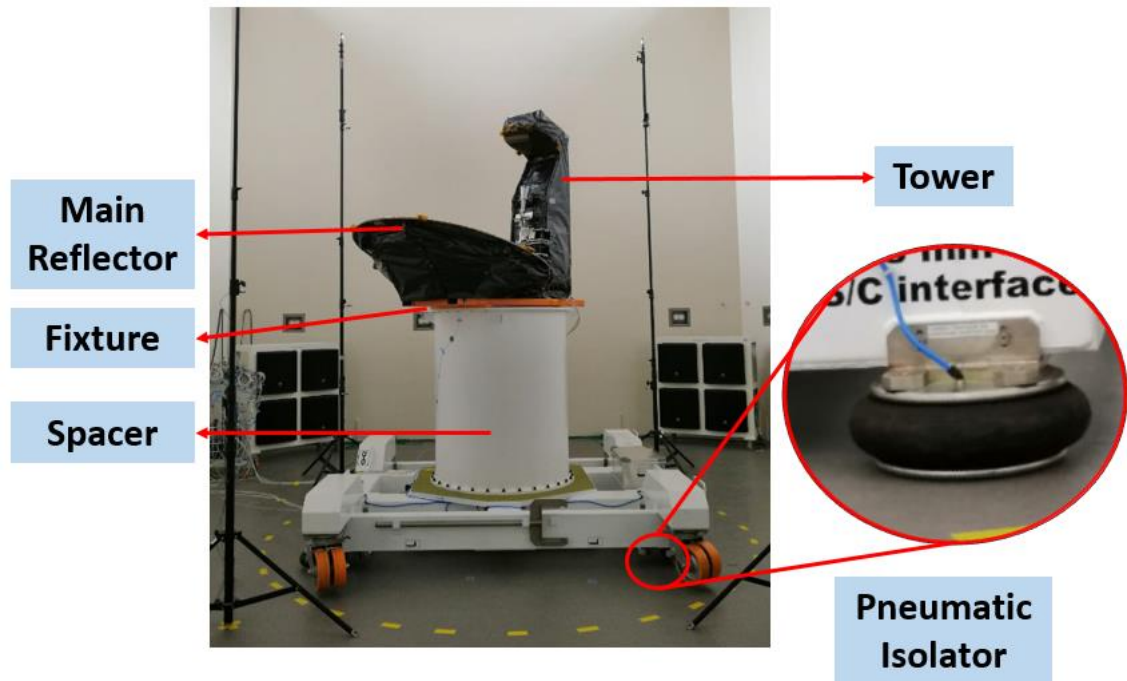


Figure 3.18. Acoustic Test Configuration

### Pre and Post Low Level Tests Comparisons

Comparisons of the low level test responses done before and after the qualification level tests present a valuable opportunity to monitor any destructive effects of the tests on the structures. The failure or damage case of the medium and qualification acoustic tests can be monitoring by the comparison of pre and post low level tests as suggested in [16,27]. If the results of these two tests are at the same or very close to each other especially for the first few natural frequencies, it can be accepted that there is no structural damage on the specimen because of the test. If there were some changes, there are various possible reasons for it, which are loosening torque of assembly bolts, local failure in the joints and fatigue cracks [22]. Also, Sarafin et. al. proposes quantitative comparison criteria between pre and post low level tests by integrating by

threaded fasteners; if change in the first resonance frequency is smaller than 5% and change in peak of acceleration responses of the first mode is smaller than 30% the test is accepted as successful with no important damage on the structure [22]. Pre and post-low level test's accelerometer results named LL01 and LL02 for the pre and post levels, respectively. Figure 3.19 and Figure 3.20 shows the results for the MR2 and MR16 which are the edge the main reflector and at the supporting structure of it. It can be referred from the figures that there are no significant changes on the reflector's structural responses after the qualification level acoustic test since the plots are very close to each other. The figures show that the difference between the resonant frequency is smaller than 5% and amplitude is smaller than 30%. Therefore, it can be said that there is no structural damage to the main reflector.

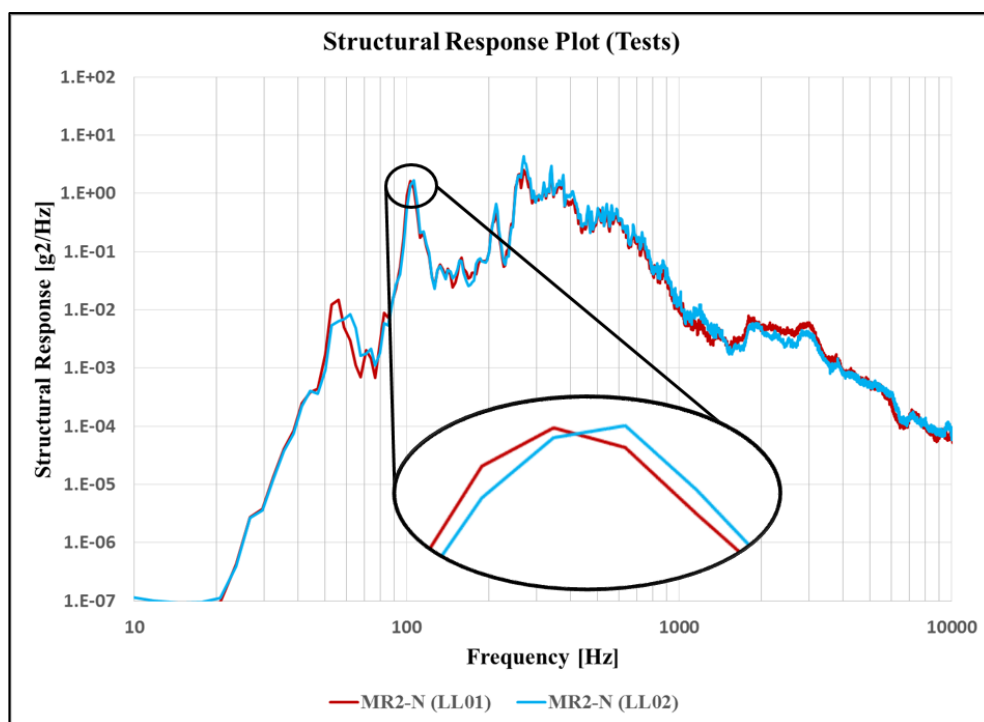


Figure 3.19. Pre and Post Low Level Test Comparison at MR2 Along Normal Axis

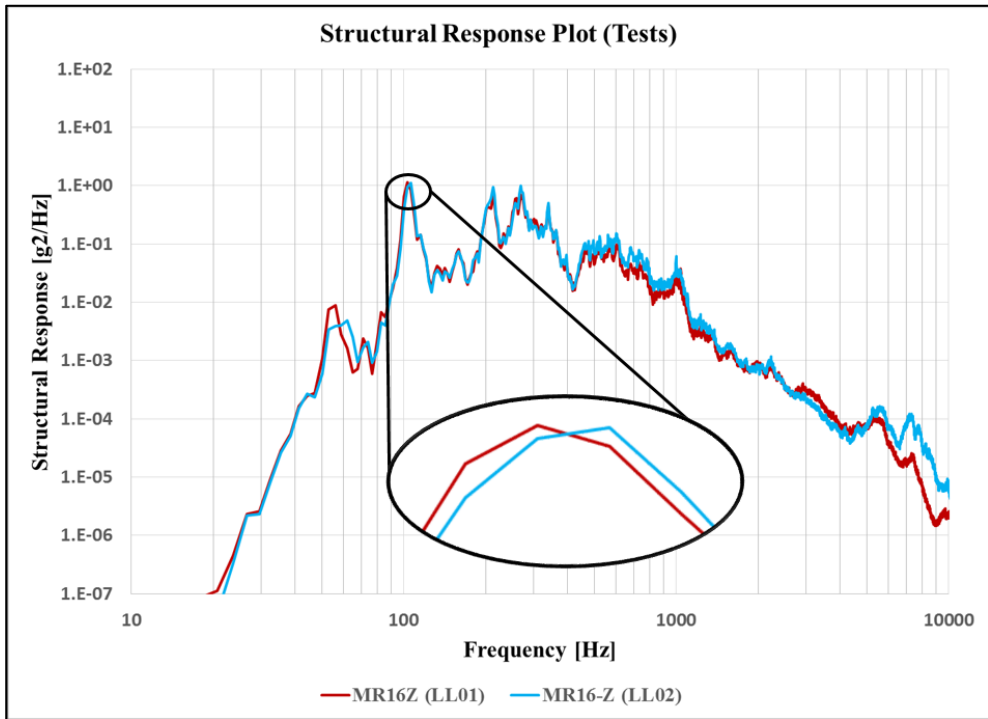


Figure 3.20. Pre and Post Low Level Test Comparison at MR16 Along Z Axis

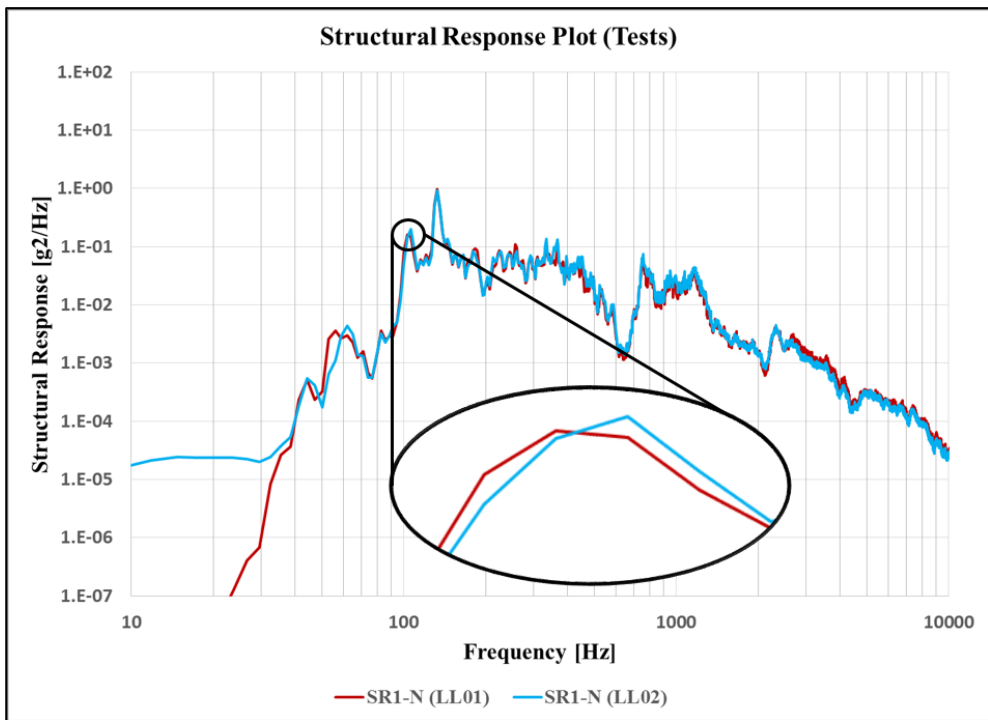


Figure 3.21. Pre and Post Low Level Test Comparison at Along Normal Axis

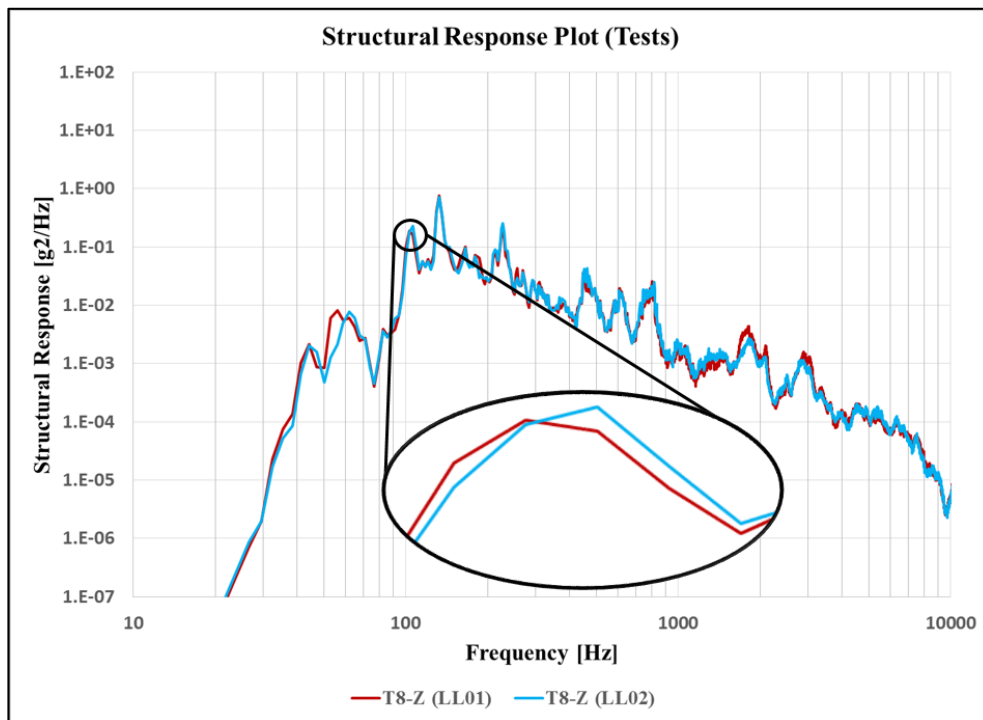


Figure 3.22. Pre and Post Low Level Test Comparison at T8 Along Z Axis

In addition to the main reflector, the condition of the sub-reflector and tower can also be shown from at Figure 3.21 and Figure 3.22. These plots show that there is no structural difference for the sub-reflector and tower. Especially, for the low frequency results are almost identical; on the other hand, the curves separate from each other with the increasing frequency. In addition to these, the situation of no change in the natural frequencies shows that the antenna has not damaged under the acoustic loads. This is verified the Sarafin's criterion that the small changes for the first natural frequency and its amplitude.

Although all the pre tests' structural responses are very close to post ones, they have slight changes. The difference of the sound pressure levels of the tests were presented at Figure 3.9 that there are slight changes at the high frequencies. Here, possible reasons of these small changes will be discussed. First of all, the amount of the nitrogen inside the reverberant chamber directly changes the results because at high frequencies the sound pressure level is provided by the gas inside the room and the speakers.

Moreover, although the tests are performed in the reverberant chamber whose environment temperature is controlled, the nitrogenous gas tanks are positioned outside of the building and those directly face the ambient temperature. The atmospheric temperature difference between these two tests is almost 10°C since the first test was performed at noon; however the second one is at night. This temperature difference may cause the test results at high frequencies.

## **3.2. Vibro-Acoustic FEM Analysis of the Antenna**

### **3.2.1. Vibro-Acoustic FEM Model of the Antenna**

This section gives details and results of vibro-acoustic analysis of the composite antenna. The analysis is used to mimic the vibro-acoustic tests which are not easily performed and repeated due to different reasons. First of all, acoustic tests are highly expensive because of their various requirements such as complicated control systems, specific systems, sensitive measurement devices etc. Moreover, those tests require specialized personal and buildings, reverberant chambers. Then, acoustic loading may be destructive for some structures. As it is stated before, the satellite and space structures have to pass the qualification tests like acoustic. In terms of acoustic, the structural thermal models have to overcome the qualification level tests while the flight model has to be strong enough for the acceptance/flight level. Vibro-acoustic analyses have importance on the determination of the critical components, structures, regions of the systems. By using these analyses, pre-judgements can be gained and some possible precautions may be taken. Therefore, due to these reasons vibro-acoustic analysis should be performed.

These analyses may propose some opportunities such as design improvements, effects of possible changes, responses under different load profiles, etc. without any test repetition. ACTRAN which is a FEM vibro-acoustic analysis package has been chosen for these analyses because of its availability and practicality. Although the general attitude towards this technique directs some doubts about FEM for acoustic analysis, ECSS Handbook suggests FEM for such analysis especially in low frequencies.

Hence, the main aims of the vibro-acoustic analysis are to get analysis results that are close to testing data especially at the low frequencies and, if possible, at mid-frequency ranges.

ACTRAN's working principle and constructing the vibro-acoustic model is introduced. The software needs the structural modal solutions of the system. The output files (.op2) including modal properties that are desired from the vibro-acoustic analysis such as acceleration, displacement, stress, force, etc. constructed at the 2.2.2 Modal Analysis of the Antenna section are used as input to ACTRAN. The accelerometer and microphone nodes are explicitly selected for output request.

The 3D acoustic domain is modelled with 0.4m away from the surfaces of the antenna and with a 2m height from the baffle plane to simulate the real case. As a result of meshing, the figure below displays the final mesh situation for both acoustic and structural domains. Here the acoustic mesh varies shown by soft gray from 13 mm (near the structure) to 82 mm in maximum. The structural mesh is exactly the same as those in the structural analysis. The borders of the acoustic mesh are modeled as 'Infinite Acoustic'. The infinite element boundary condition is used to obtain 'Non-Reflective Boundary Condition'. By using these boundary conditions, the reflected waves from the boundaries are not considered; however, the incident plane waves coming from 160 sources are directly applied to the test specimen. Hence, the sound pressure levels are properly simulated. On the other hand, 'baffle plane' is used to calculate the contribution reflected waves from the floor of the chamber.

Then, acoustic-structure coupling is one of the most important issues for the vibro-acoustic analyses. Although some studies that do not require coupling and acoustic pressure are applied directly to the structures as surface load, Stavrinidis emphasizes the necessity of the coupling especially for the structures with complex geometries and including acoustic cavities [13]. Hence, acoustic-structure coupling is applied to the antenna because of its geometry and cavities like the inner part of the tower. ACTRAN proposes two options for coupling which are node by node coupling

(compatible coupling) and coupling by surfaces (incompatible coupling). Node by node coupling is used for the analyses that acoustic and structure coupling nodes are exactly the same where the preparation is troublesome. On the other hand, coupling by surfaces which is more convenient needs the introduction of the acoustic and structural coupling surfaces directly. As it was emphasized in the vibration analysis part, the antenna's structural model contains 2D shell elements and the thicknesses are not modeled, but the thicknesses of each part is parametrized. The acoustic coupling surfaces should match with this thickness values. Therefore the 3D model surfaces are used for the acoustic coupling surfaces. Figure 3.24 illustrates the coupling surfaces clearly where half of the acoustic coupling surfaces are seen as red color and the rest are the structural part. The acoustic coupling surfaces are the exact surfaces corresponding to the thickness of the parts.

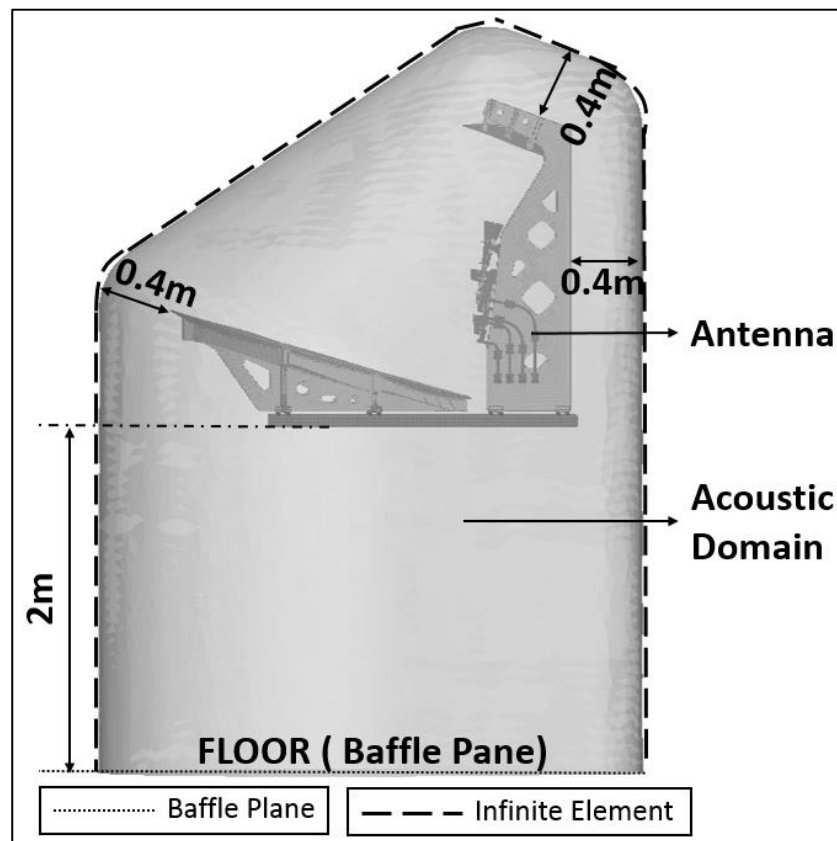


Figure 3.23. Antenna inside the Acoustic Domain

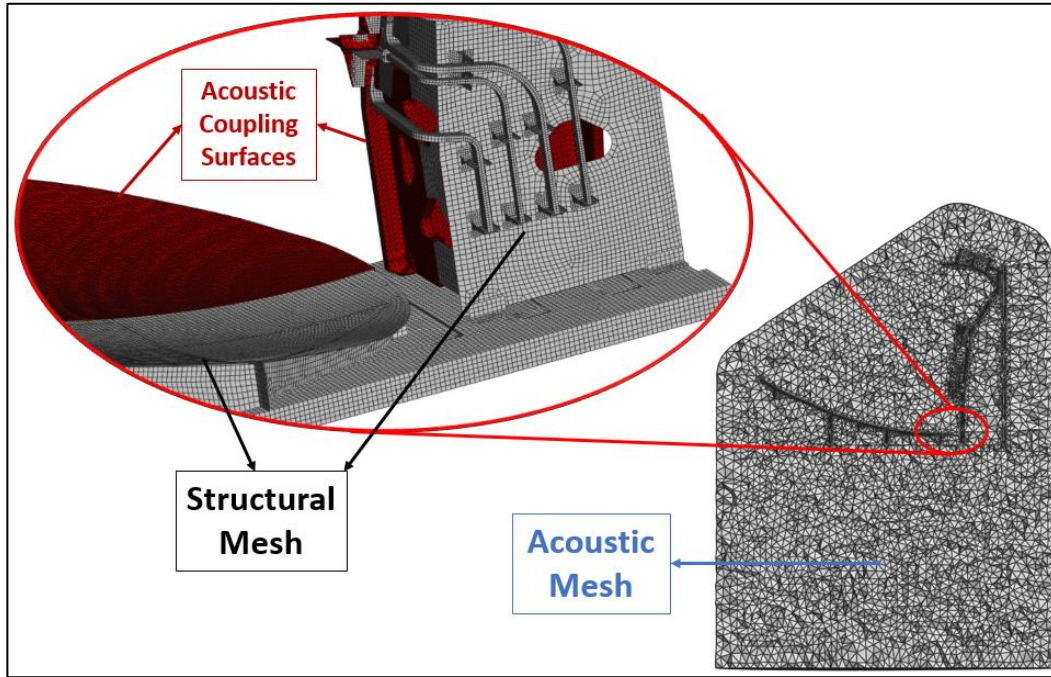


Figure 3.24. Acoustic Mesh and Acoustic-Structure Coupling Surfaces

Determination of the frequency range of the solution depends on various factors such as the necessities of the data, modal density of the structure, total element number, the memory of the computer, mesh size so on. In literature, minimum mesh size should be smaller than the one sixth of the minimum wavelength as specified in ( 21 ) but sometimes forth of the wavelength can be used at some studies [17].

$$\text{minimum element size} < \frac{\lambda_{min}}{6} \quad ( 21 )$$

By using formula ( 21 ), the minimum mesh sizes, total number of elements and corresponding required memories are listed at Table 3.8.

Table 3.8. *Mesh Dimension and Total Acoustic Element Number for Different Frequencies*

Frequency (Hz)	<i>Mesh Size (mm)</i>	<i>Total Element Number</i>	<i>Required Memory (GB)</i>
500	111	709236	17
600	94	788133	19
750	75	1074358	20
1000	56	1547587	>32
1400	40	3285206	>32

The selection of the upper limit of the vibro-acoustic analysis depends on different subjects. From the test results, it should be remembered that after 700Hz, the structural responses start to drop. Above this frequency limit the structural responses become small and negligible. 750Hz is also seen as a limit in terms of computation cost. The analyses above 1000Hz exceed the computer's limits. Therefore, it is decided that the most critical behaviors of the assembly are at the low frequency range and the analysis is performed up to 750Hz by considering this case and the required memory issues.

Modeling of the sound pressure level at the acoustic domain is provided by ACTRAN VI interface by using plane waves around the surfaces of the antenna. 160 of the plane wave sources in 8 parallel levels are used which can be seen via Figure 3.25 as red dots and acoustic domain and antenna are shown as a small white region in the middle of the figure. A similar study is performed by Wickramasinghe by building the diffuse sound field by using 20 planar wave sources rotating with  $45^{\circ}$  angle. These sources are separated uniformly on the surface of a sphere [17]. The sound pressure on the reverberation chamber can be simulated by such a symbolic view.

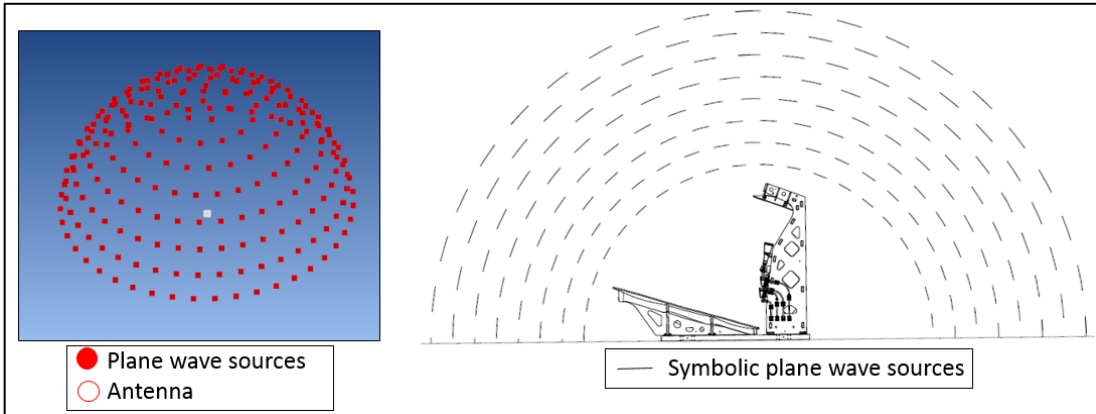


Figure 3.25. Modelling of Diffuse Sound Field

The selection of damping is critical in order to catch the peak values. For damping determination, the same methods with the frequency response analysis are applied as explained in Section 2.2.3.1. Initially, the damping values at literature and estimates from half-power method are applied, then an iterative method is applied to improve the results. At the beginning of the vibro-acoustic analysis numbered as #35, the damping values obtained at the structural frequency response analysis and tabulated at Table 3.9 are directly used. In this analysis, the acoustic test fixture is not modeled.

Table 3.9. Damping Values for the First Vibro-Acoustic Analysis

Frequency [Hz]	20-135	135-180	180-260	260-330	330-500
Damping (%)	1.5	4.0	1.5	1.0	1.5
Frequency [Hz]	500-600	600-640	640-650	650-760	760-800
Damping (%)	1.4	2.0	5.0	0.3	2.0

The results of the first vibro-acoustic analysis performed by using the ‘.op2’ file that obtained and validated by sine-sweep resonance test and tuned by using the damping values are presented in the following figure where MR2 (normal direction), SR1 (normal direction) and T10 (Y-direction) accelerometers results are shown.

Transferring the outputs of the vibro-acoustic analysis is necessary for finding the structural results. Firstly, the acceleration and displacement responses of the

accelerometer points are taken by using ‘Solid GAcceleration’ and ‘Solid Displacement’ commands of ACTRAN. Similarly, the nodal stress is requesting by the ‘Solid Stress (vmises)’ command. On the other hand, the force response is extracted by using the ‘Element Force’, thus the mesh elements are independently selected on the model.

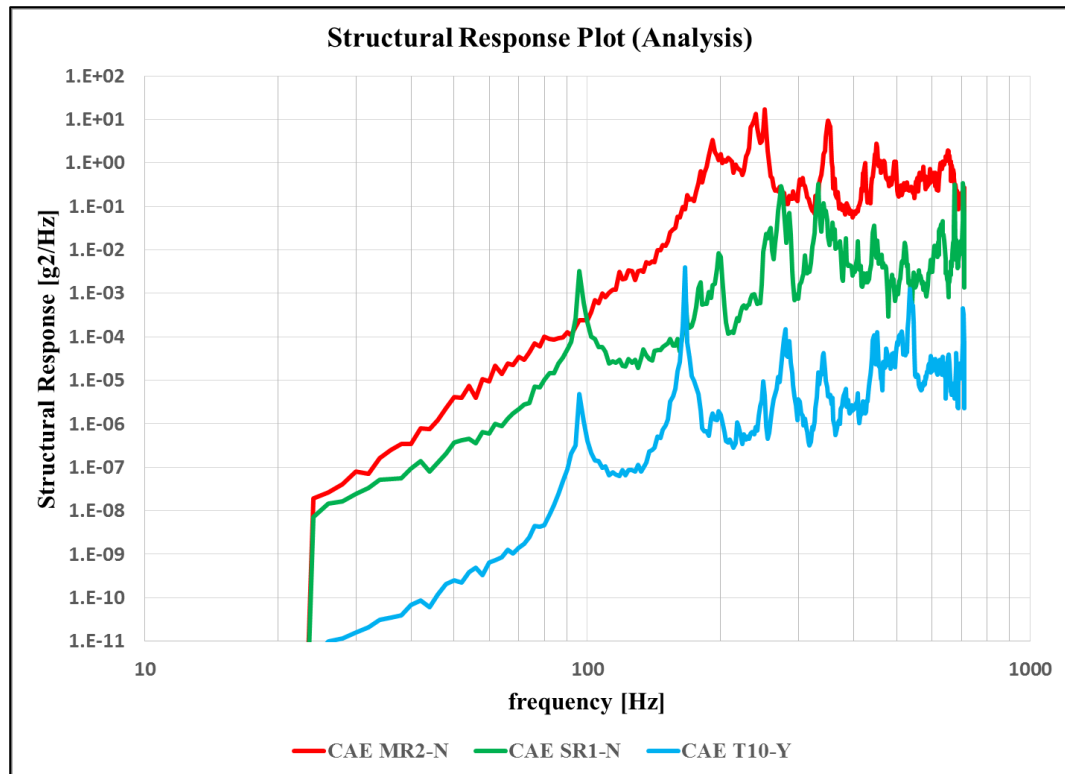


Figure 3.26. Responses of First Vibro-Analysis at MR2, SR1 and T10-Y

The examination of this first vibro-acoustic analysis should start with the natural frequencies. In this analysis, model the tower and main reflector’s interface bracket connections are independently modelled and different stiffness values are used, but the acoustic test fixture is included to the calculations. Figure 3.26 illustrates that first three natural frequencies for the tower are 92Hz, 97Hz, and 166Hz for tower while 192Hz, 238Hz and 252Hz for the main reflector assemblies. These analysis results are obtained by directly using the modal analysis output file tuned by sine-sweep test. The natural frequencies obtained from this analysis are compared with the sine sweep test,

acoustic test and vibration analysis results in the Table 3.10. As a result, the vibro-acoustic test results are far from the other three results. The reason of this is the vibration and vibro-acoustic analysis models are exactly the same and adjusted according to vibration test results. Therefore, these three results are very close to each other. The small differences between those can be ignored. On the other hand, the significant difference of the acoustic test is probably because of the changing boundary conditions resulted from the spacer.

Table 3.10. *Natural Frequency Comparison of the Acoustic/Sine Sweep Tests and Modal/Vibro-Acoustic (1<sup>st</sup>) Analyses*

		1 <sup>st</sup> natural frequency ( $f_1$ ) [Hz]	2 <sup>nd</sup> natural frequency ( $f_2$ ) [Hz]	3 <sup>rd</sup> natural frequency ( $f_3$ ) [Hz]
Tower	Vibration Test	91	96	167
	Vibration Analysis	91.7	96.9	167.4
	Acoustic Test	45	53	106
	Acoustic Analysis	91	96	166
Main Reflector	Vibration Test	191	214	244
	Vibration Analysis	199	216.4	244.3
	Acoustic Test	45	53	106
	Acoustic Analysis	192	240	252

At this point, the acoustic analysis model has to be updated to reach the vibro-acoustic test results. If there is not any limitations, it is required that each components of the assembly consisted of spacer with pneumatic isolators, fixture and antenna should be modelled independently. Then, this analysis model has to be checked and tuned by test. On the other hand, the spacer and the isolators are TAI's components, there is no control on them. None of the CAD model, 2D drawing or material property are known by the author, hence numerical modeling was impossible. Material and geometry information exists for only acoustic test fixture; thus the fixture is included in the vibro-acoustic analysis.

The modal analysis of the acoustic test fixture is included in the thesis since it is possible that low natural frequencies of the test fixture may affect the acoustic tests and analysis. Figure 3.27 illustrates the acoustic test fixture and its finite element model. Mass of the fixture is almost 100kg and it is made of aluminum 6061 rectangular profiles with 5mm thickness.

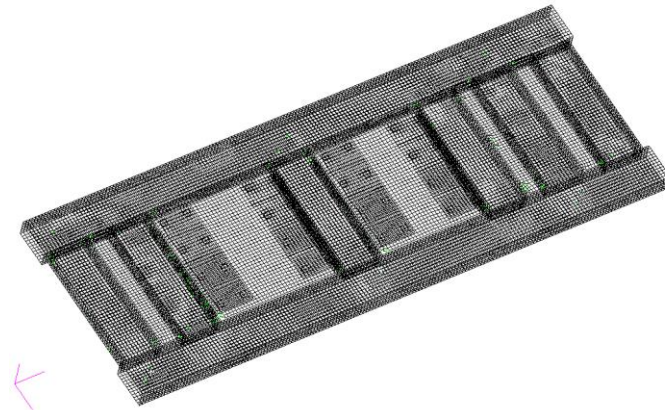


Figure 3.27. Acoustic Test Fixture and its Finite Element Model

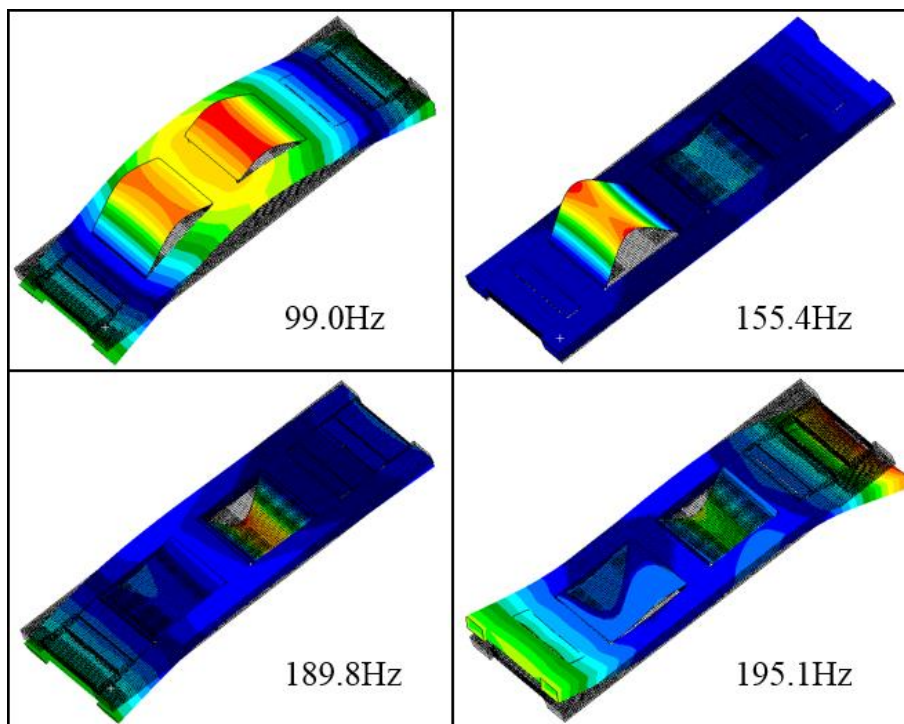
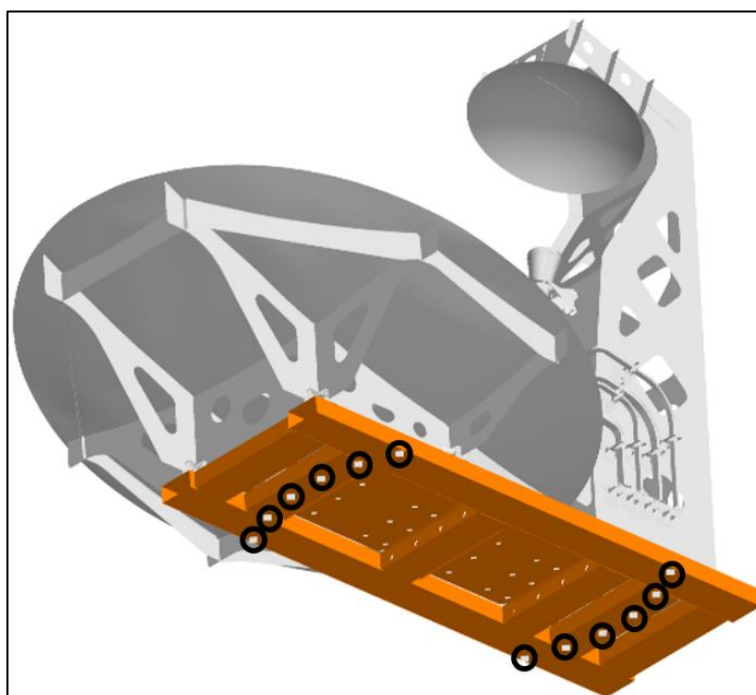


Figure 3.28. Mode Shapes of the Acoustic Test Fixture

The first four natural frequencies of the fixture are 99Hz, 155.4Hz, 189.8Hz, 195.1Hz and corresponding mode shapes are found as shown in Figure 3.28. It is important to note that, these results are obtained in the light of the material properties of aluminum and the general stiffness values, the results are not validated with any test. In conclusion, although the fixture is a rigid structure composed of thick metal rectangular profile, first three modes are due to the thin panels of the structure. The massive part of the fixture is excited at the 195Hz.

Nevertheless, the vibro-acoustic test results are totally different from these values because of the modeling incapability of the pneumatic isolators and spacer. In order to obtain proper natural frequencies close to the acoustic test results, an iterative process is required. This iterative process includes changing the stiffness values of the PBUSH elements of the fixture's boundary conditions shown as dark black circles in Figure 3.29 where the fixture is shown as orange color. By using the acoustic test data, the model is tried to match the test results.



*Figure 3.29. Vibro-Acoustic Model and Boundary Conditions*

As a result of this iterative process, new natural frequencies obtained from updated vibro-acoustic model are obtained as 46Hz, 68Hz and 102Hz. Table 3.11 summarizes the natural frequency comparison of the vibro-acoustic test and analysis with relative error.

Table 3.11. *Natural Frequency Comparisons of the Vibro-Acoustic Test and Analysis*

	1 <sup>st</sup> natural frequency ( $f_1$ ) [Hz]	2 <sup>nd</sup> natural frequency ( $f_2$ ) [Hz]	3 <sup>rd</sup> natural frequency ( $f_3$ ) [Hz]
Test	45	53	106
Analysis	46	68	102
Error (%)	2.22	28.30	3.77

Although 2<sup>nd</sup> natural frequency has 28.30% error, test and analysis results are seen as close to each other. By detailed examination of the vibro-acoustic model by using this updated model will be considered in Section 3.3.

### 3.3. Comparisons of the Vibro-Acoustic Tests and FEM Analysis of the Antenna

In this section, final results of vibro-acoustic analyses are compared with the vibro-acoustic test data. As a result of the changes in the vibro-acoustic finite element model which is explained above, the modal model is finalized. However, in order to obtain the amplitudes of the peaks, the damping selection for the different frequency bands becomes important. Therefore, the damping ratios are determined by using similar structures presented in the literature, half-power bandwidth method and iterations.

Table 3.12. *Damping Values for the Finalized Vibro-Acoustic Analysis*

Frequency Range [Hz]	0-100	100-120	120-200	200-300	300-400	400-750
Damping [%]	3	1	3	1	0.5	1

After updating the finite element model, a new analysis is performed and corresponding plots are obtained. The analysis results are examined to show the

responses of the different components of the antenna. Figure 3.30 shows that the main reflector is the most sensitive component against the acoustic loading. The other reflector has the second affected component while the tower is affected least. The statement “large surfaces are mostly affected” is validated through this figure.

Comparisons of the random vibration responses of the test data and the final analysis of the MR2, MR16 and T10 accelerometers are presented in Figure 3.31, Figure 3.32 and Figure 3.33, respectively. From these figures, it can be concluded that, the analysis results have an agreement with the test data in terms of the general behaviors. In addition to this, the peak values are also very close to each other. On the other hand, the curves are not similar at the low frequencies. The reason for this could probably be the lack of knowledge of the boundary conditions. In order to obtain more proper results, the boundary conditions have to be perfectly satisfied.

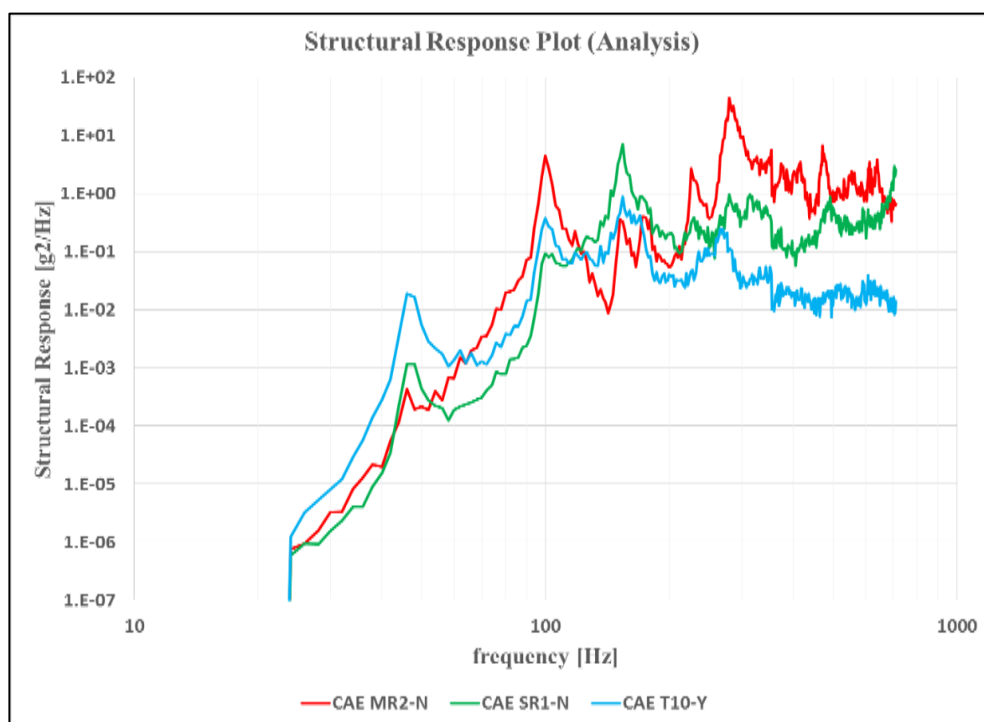


Figure 3.30. Comparison of the Analysis Results of MR2, SR1 and T10-Y

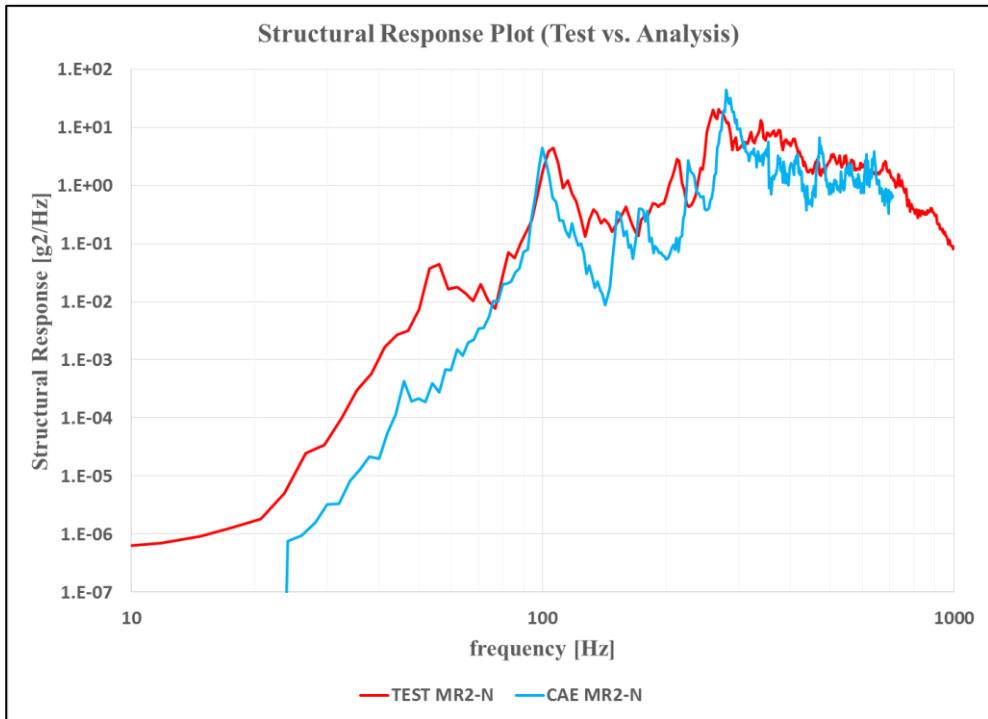


Figure 3.31. Comparison of Analysis Results with Test Data at MR2

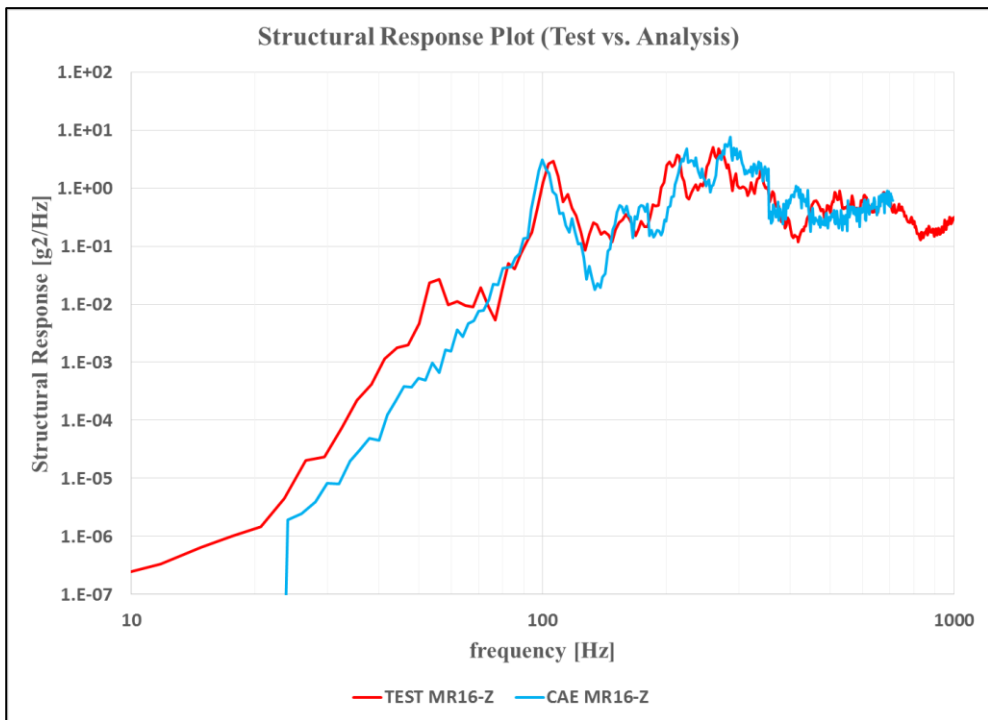


Figure 3.32. Comparison of Analysis Results with Test Data at MR16-Z

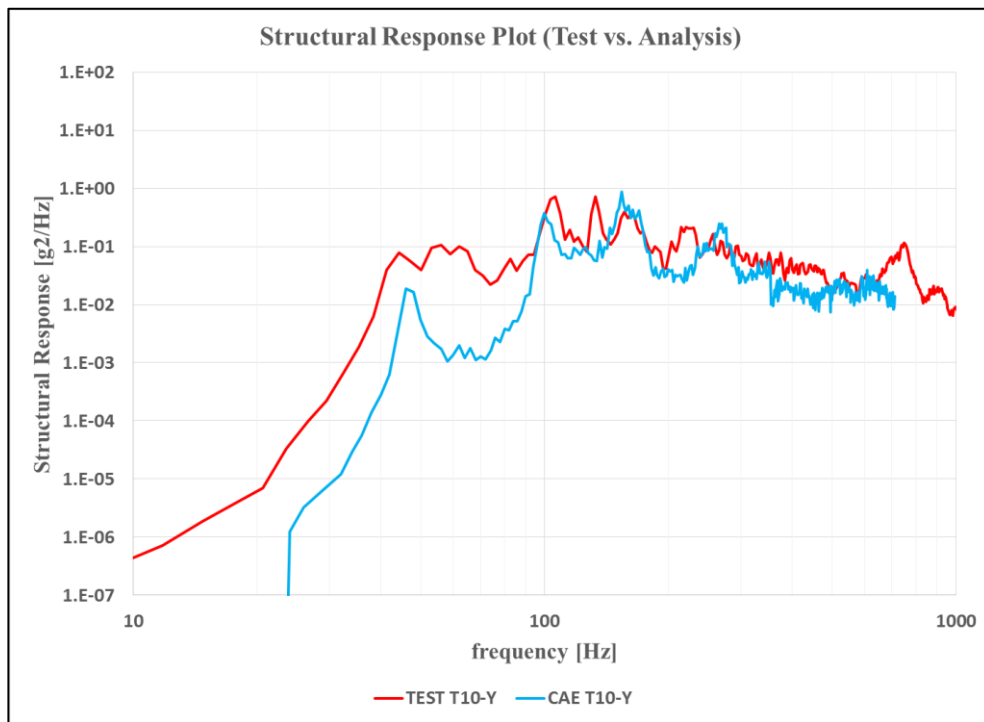


Figure 3.33. Comparison of Analysis Results with Test Data at T10-Y

One of the most important properties of the simulations or analysis is to examine any possible effects on the structure or the structures' any responses like acceleration, displacements, forces, stresses so on. Up to this point, only the acceleration responses of the structures are considered. However; the next figure displays the von Mises stress of the just near elements of the points MR2, MR16 and T10 since von Misses are obtained from the elements in the software. The plot gives the information that the maximum stress is seen on the main reflector among these three curves. The maximum values of three curves are in the order of kPa or a few MPa. Thus, there is not any damage threat as a result of the analysis when these stress are compared to material properties that were given in the Introduction chapter.

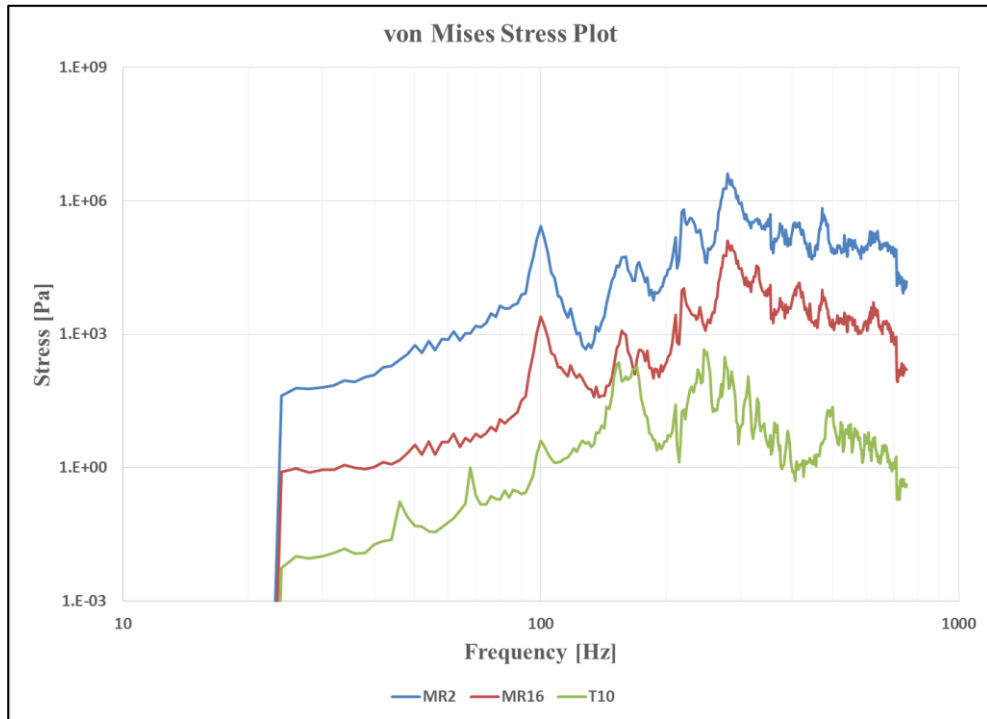


Figure 3.34. von Mises Stress Outputs of the MR2, MR16 and T10

In addition to these results, ACTRAN proposes the displacement plots at the specific frequencies. The critical frequencies that the von Mises stress plots of the antenna are maximum are determined via Figure 3.34. Therefore, displacement and stress outputs at frequencies of 46Hz, 100Hz, 160Hz, 246Hz and 280Hz will be presented in the plots from Figure 3.35 to Figure 3.39. The stresses that the specimen is subjected to give a good ability to discuss the situation of the structure under the environmental circumstances. At this point, the vibro-acoustic analysis results are discussed in terms of stress. It is seen that from the figures below, the maximum stress is seen at the 280Hz plot as in the order of few MPa's. Since the stress values change depending on the positions they are considered locally. The main reason for this is the high sound pressure level at this frequency band.

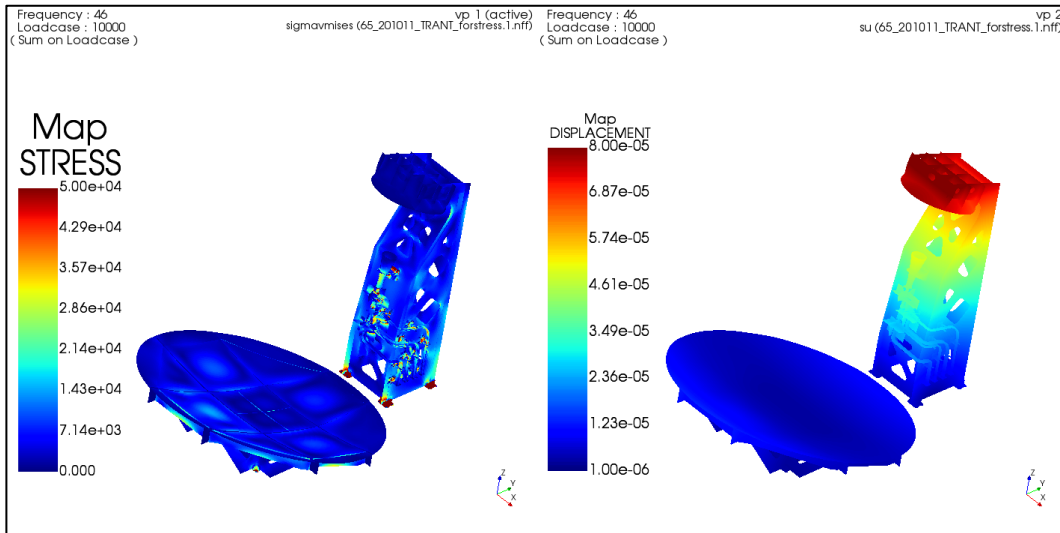


Figure 3.35. Vibro-Acoustic Analysis' Displacement and Stress Results Graphs at 46Hz

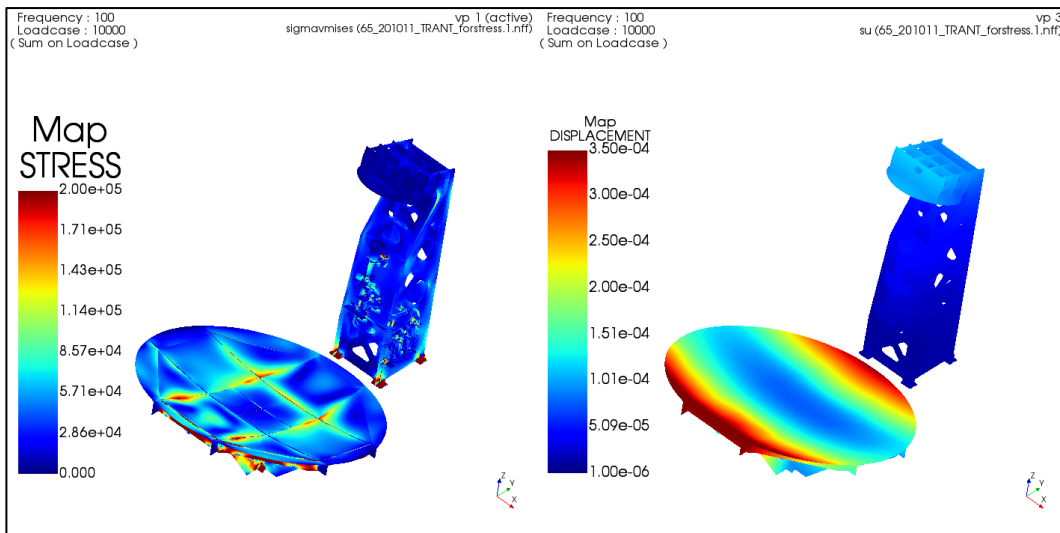


Figure 3.36. Vibro-Acoustic Analysis' Displacement and Stress Results Graphs at 100Hz

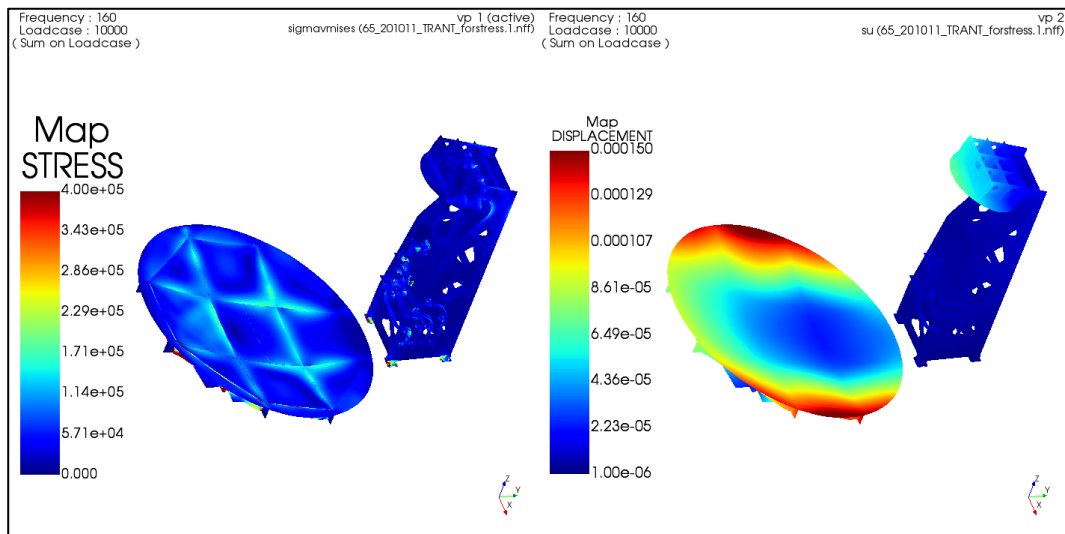


Figure 3.37. Vibro-Acoustic Analysis' Displacement and Stress Results Graphs at 160Hz

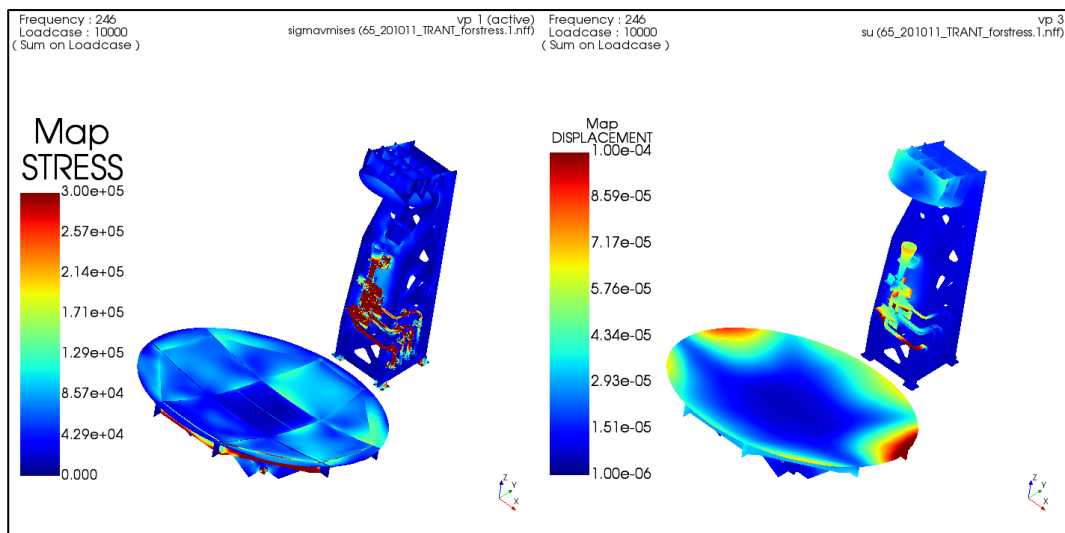


Figure 3.38. Vibro-Acoustic Analysis' Displacement and Stress Results Graphs at 246Hz

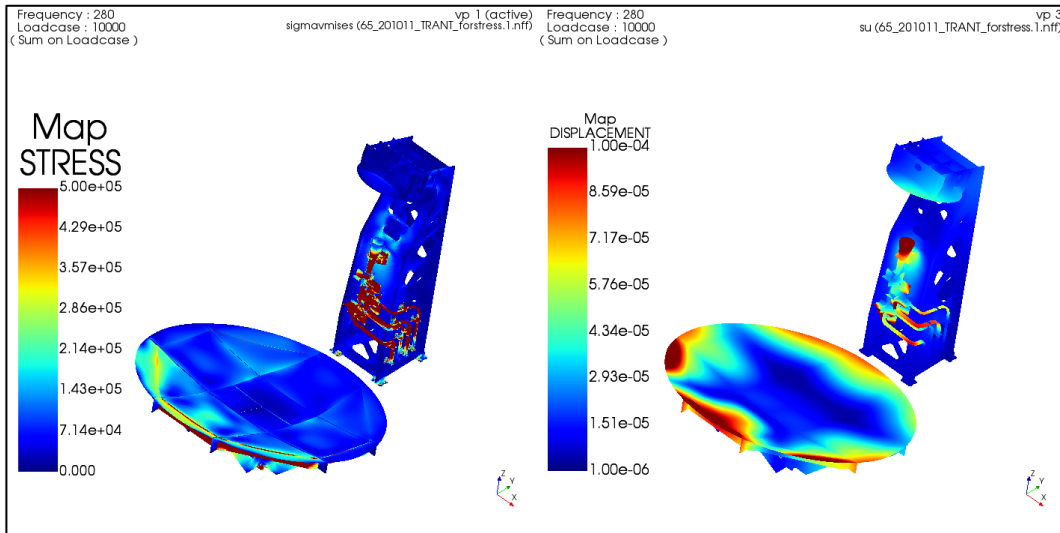


Figure 3.39. Vibro-Acoustic Analysis' Displacement and Stress Results Graphs at 280Hz

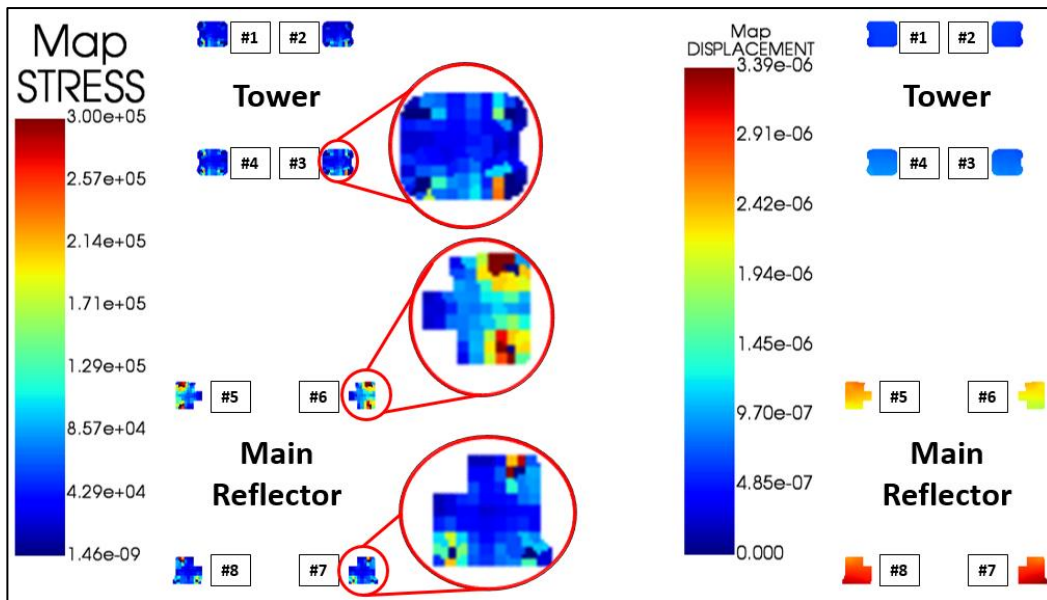


Figure 3.40. Stress and Displacement Graph of Bottom Surface of Brackets at 280Hz

In order to show the critical brackets and their locations Figure 3.40 is given. In this figure, the stress and displacements are given at the bottom surfaces of the brackets. It can be referred that, the tower brackets labeled as #1 to #4 have insignificant stress and displacement distributions. On the other hand, the main reflector brackets labeled as #5 to #8 have comparatively large stress and displacement distributions. Although it is expected that the maximum stress and displacement distributions should be at the

brackets #7 and #8 which are the closest brackets to the main reflector tip, this is not the obtained case as it can be seen from the figure. It can be said that brackets #5 and #6 including 2 mounting interface holes has the largest stress distribution around the holes. However, the maximum displacements occur at the main reflector's other brackets numbered as #7 and #8. The displacement distribution is as expected, but the different results at the stress distribution can be explained by the different number of mounting interfaces. Although the total stress is shared by 3 connectors at the brackets #7 and #8, it is shared by 2 connectors for the brackets #5 and #6. This assessment might be a valid input for the design process. Increasing the number of connectors at brackets #5 and #6 would be a good design improvement. In summary, the maximum stress and displacements at the brackets are measured as 2.78MPa and 0.0129mm. Besides, the stress distribution on the composite structures is measured as 500kPa at 280Hz shown on the figures.

For the vibro-acoustic analyses, it can be concluded that although the acceleration response curves do not exactly match with the test data, both of them have similar trends and magnitudes, there are only slight changes between those. Additionally, the displacement response plot and graphs show that the displacements of the antenna under the corresponding sound pressure level are not much high, in the order of hundred micrometers. If the displacement has been high, the functionality of the antenna would be harmed since even micrometers are so critical for satellite applications. Last but not least, the stress graphs show that the maximum stresses are 500kPa and 2MPa on the composite and interface brackets. These small values prove that there is not any potential damage at the structure since the stresses resulted from vibro-acoustic analysis are smaller than tensional, compressive and flexural strengths of the composite components. As it is expected, the stresses change with the confronting sound pressure level, in parallel. Therefore, according to acoustic tests and vibro-acoustic analyses results, there are no threats for the structure due to acoustic loading.



## CHAPTER 4

### CONCLUSION AND FUTURE WORK

#### 4.1. Conclusion

Satellites and their components have distinctive properties because of their specific environmental and operational conditions. There are always strict and unbreakable limits on them, especially because of the launchers. First of all, those structures have to be lightweight for the reason of capacity of the rocket launcher. Then, the random vibration and acoustic load resulted from the engines and turbulent air conditions of the rocket may have critical destructive effects on the light and large structures. Moreover, they should be strong enough to resist the space environmental conditions, which are low and high operational temperatures. Therefore, in the light of these conditions, the space reflector antenna that is responsible for the communication of a Turkish space program is manufactured. The antenna is a large and light-weight composite structure which may be sensitive to the acoustic loading.

In this work, the manufacturing processes, vibration, vibro-acoustic tests and corresponding analyses are presented. Firstly, a sandwich composite structure composed of carbon honeycomb and CFRP face sheets and its manufacturing details is briefly explained. Some design and manufacturing tips are provided. Then, sine sweep tests are performed up to 2000 Hz by using 7 accelerometers and the results are presented. The main aim of these tests is to obtain information that is used for calibration of the analysis model of the antenna. Hence, the natural frequencies of both subassemblies which are tower and main reflector are determined by the corresponding frequencies of the peaks obtained from the test results.

Furthermore, finite element model of the antenna is prepared in HyperMesh and MSC Patran. This model is used as a base model throughout the thesis. Both composite and

metallic parts are modeled via QUAD and TRIA cards which are shell elements. Using these 2-dimensional elements have reduced the computational cost both time and required memory. The model is used for both modal and frequency response analyses by using MSC NASTRAN, which is commonly used in space applications because of improvements on it were performed by NASA. First of all, modal analyses of tower and main reflector are separately performed by using 'SOL103' solution type. Model is updated by adjusting the stiffness values of the nodes simulating the bolts. After the iterative updates, the natural frequencies are obtained with a maximum error of 3% up to 750 Hz. Although the sine sweep tests are performed up to 2000 Hz, 750 Hz is selected as the upper limit due to decreasing of the acoustic input at frequencies higher than 750 Hz. Next, frequency response analysis is done for both sub-assemblies. The main object of this analysis is to arrange the peak values at the natural frequencies that were specified by the modal analysis through different damping ratio values. Therefore, the damping ratios are sensitively chosen for the main reflector and especially tower.

Acoustic tests and structural responses of the antenna are one of the most critical issues of this thesis. Since acoustic tests are rarely performed, its contribution is significant. The acoustic tests are performed in a reverberant chamber providing an environment with diffuse acoustic pressure. The acoustic loading of 145.6dB (OASPL) determined by the launcher is applied to the antenna, which can be a large pressure level for a light space structure. This overall sound pressure level is applied to the structure in one-octave band up to 8 kHz. The test is controlled by a feedback system which uses 8 microphones. The success of the test in terms of reaching the required acoustic levels is shown by these microphone measurements and their comparison with the pressure values dictated by the standards. For the structural part, the response of the antenna is measured by using 35 accelerometers. The structural success of the test is shown by the pre and post level acoustic tests. Those tests are performed just before and after the qualification level tests. Their close results at each accelerometer imply that no structural damage and changes occurred during the test. In addition to this low level

tests, the functional tests also proved that there are no significant structural changes to the antenna.

Vibro-acoustic analysis is one of the most challenging parts of this study. Finite element technique is used both acoustic and structural parts. The analysis is performed in the MSC ACTRAN. The software requires structural modal analysis of the antenna and couples those results with the acoustic region constructed in it. One hundred sixty plane wave sources were used to obtain the acoustic domain for the analysis. The acceleration and displacement outputs at the nodes corresponding to accelerometer locations are obtained from the FEM analysis. The analysis results are compared with the test results in order to prove the success of the analysis. Therefore, although vibration results of the acoustic analysis do not exactly match with the test results, the match seem to be better than the other studies listed in the literature review. The general behaviors and the peak values are similar to the test as displayed in the related sections.

Finally, the vibro-acoustic analysis has several advantages for structural space applications. The first reason, is the the lack of opportunities to perform several acoustic tests because of the cost of the tests and the specimen. The other reason is the possible destructive effect of acoustic loading. Performing the tests is not possible for each design change, for example. If any changes in the design is required, the analysis model can be directly used to see its effect without any test. As the output of this thesis study, a numerical model exists which can be used to understand the effect of any design change on the acoustic qualification test results.

#### **4.2. Future Work**

Although it is thought that successful results are obtained throughout the thesis work, there are still some weaknesses. In this section, possible work to improve such a thesis will be discussed.

To begin with, using modal tests probably give more accurate results than the sine sweep tests for determining the natural frequencies. Modal tests present both the

natural frequencies and the mode shapes of the structures. Moreover, modal updating could be performed by using appropriate engineering tools rather than iterative and manual stiffness determination in vibration analysis. By using these tools, the model can be easily updated by using the test data.

This thesis' FEM acoustic results may be replaced or compared by the BEM or SEA analysis. Especially for the analysis at high frequencies SEA can be used and all results may be compared with FEM results and optimum solution technique would be presented for the space antennas at high frequencies.

Furthermore, from this study the small stress values show that there are no structural threats to the antenna. On the other hand, since the functionality of the space structures depends on few micrometer difference on the positioning of the components, loosening at the brackets' connectors torques may require independent study. The stresses that are resulting in loosening on the connectors can be determined by an additional study. The vibro-acoustic analyses stress results can be compared with stress values which results in loosening and the conditions for loosening of the connectors may be assessed with numerical means.

## REFERENCES

- [1] Ullio, Roberto & Marucchi-Chierro, Pietro. (2005). GOCE satellite vibro- acoustic performance predictions using Alenia integrated F.E.M. & S.E.A. approach. European Space Agency, (Special Publication) ESA SP. 581. 79.
- [2] Ariane 5. (n.d.). Retrieved December 25, 2019, from [http://www.esa.int/Enabling\\_Support/Space\\_Transportation/Launch\\_vehicles/Ariane\\_5](http://www.esa.int/Enabling_Support/Space_Transportation/Launch_vehicles/Ariane_5).
- [3] Hambric, S.A. & Sung, S.H. & Nefske, Donald. (2014). Engineering Vibroacoustic Analysis: Methods and Applications. 10.1002/9781118693988.
- [4] Boshouwers, J., Gimersky, M., Grenier, C., Poulin, D., Riendeau, S., & Uher, J. (2017). Design and implementation of the Koreasat-3 Ka-band FSS antenna. Symposium on Antenna Technology and Applied Electromagnetics, ANTEM 1998 - Conference Proceedings, 423–426 <https://doi.org/10.1109/ANTEM.1998.7861676>
- [5] Thermal Conductivity of selected Materials and Gases. (n.d.). Retrieved December 25, 2019, from [https://www.engineeringtoolbox.com/thermal-conductivity-d\\_429.html](https://www.engineeringtoolbox.com/thermal-conductivity-d_429.html).
- [6] Xia, L.-J & Jin, X.-D & Wang, Y.-B. (2003). Equivalent analysis of honeycomb sandwich plates for satellite structure. 37. 999-1001.
- [7] British Standard. (1993). General Tolerances. BS-EN-22768-1:1993.
- [8] United States., & Battelle Memorial Institute. (2008). MMPDS-04: Metallic materials properties development and standardization (MMPDS). Washington, D.C.: Federal Aviation Administration.
- [9] NASA. (2011). Payload Vibroacoustic Test Criteria. NASA Technical Standards System, 8–39.
- [10] ECSS. (2009). Space engineering - System engineering general requirements. ECSS-E-ST-10C. (March), 100.
- [11] Hansen, C. H. (2018). Foundations of vibroacoustics. [electronic resource]. Taylor & Francis, a CRC title, part of the Taylor & Francis imprint, a member of the Taylor & Francis Group, the academic division of T&F Informa, plc.
- [12] Sikström, J. (2011). Vibro-acoustic analysis of a satellite reflector antenna using FEM (Dissertation). Retrieved from <http://urn.kb.se/resolve?urn=urn:nbn:se:umu:diva-39875>

- [13] Stavrinidis, C., Witting, M., Ikoss, S. I., & Klein, M. (2001). Advancements in vibroacoustic evaluation of satellite structures. *Acta Astronautica*, 48(4), 203–210. [https://doi.org/10.1016/S0094-5765\(00\)00123-5](https://doi.org/10.1016/S0094-5765(00)00123-5)
- [14] A. D. Pierce, *Acoustics; An introduction to its Physical Principles and Applications*, 2 ed., Acoustical Society of America, Woodbury, New York, 1989.
- [15] Smith, A. (2004). Space engineering. *Space Science*, (June), 443–458. [https://doi.org/10.1142/9781860944574\\_0014](https://doi.org/10.1142/9781860944574_0014)
- [16] Hughes, W., & Glenn, N. (2019). Overview of the Acoustic Testing of the European Service Module Structural Test Article (E-STA). (March 2017).
- [17] Wickramasinghe, Viresh & Grewal, Anant & Zimcik, David & Woronko, Andrew & Rossignol, Patrick & Philie, Vincent-Olivier & O’Grady, Mark & Singhal, Raj. (2011). Acoustic Testing and Response Prediction of the CASSIOPE Spacecraft. 10.1007/978-1-4419-9302-1\_4.
- [18] Calvi, Adriano & Aglietti, Guglielmo & Albus, J. & Bellini, M. & Burtin, D. & Cavro, Etienne & Dupré, J. & Fabriés, C. & Fransen, S. & Gangloff, D. & Girard, A. & Gualtieri, N. & Itta, A. & Kerschen, Gaëtan & Konrad, W. & Morisset, R. & Nali, Pietro & Newerla, A. & Quagliotti, G. & Wijker, Jaap. (2013). ECSS- E-HB-32-26A Spacecraft Mechanical Loads Analysis Handbook.
- [19] Haiyang, Gao & Xinglin, Guo & Yicun, Xie & Yanjing, Yang & Ouyang, Huajiang. (2020). Fault Detection for a Satellite-like Structure Using Sine Sweep Vibration Test Data. 10.1007/978-981-13-8331-1\_34.
- [20] Mangal, S. K., & Gupta, A. K. (2016). Optimization of parameters for damping in sandwich structures. *International Journal of Performability Engineering*, 12(3), 203–214.
- [21] Chai, S. F., Wang, P., Wu, Z. J., Wang, J., & Che, G. F. (2015). Acceleration Data Acquisition and Analysis Method of Shaking Table Test. *Applied Mechanics and Materials*, 724, 205–212. <https://doi.org/10.4028/www.scientific.net/amm.724.205>
- [22] Sarafin, T., Demchak, L., & Browning, M. (2017). Vibration Testing of Small Satellites - Part III - Rev. A. *Vibration Testing of Small Satellites*, 1–11.
- [23] Siemens Product Lifecycle Management Software Inc. (2014). *NX Nastran User’s Guide*. 886.
- [24] KGSTOCKGEARS. (2007). Technical Data Technical Data. *Pnas*, 1, 38–40. Retrieved from [https://www.kggear.co.jp/en/wp-content/themes/bizvektor-global-edition/pdf/TechnicalData\\_KGSTOCKGEARS.pdf](https://www.kggear.co.jp/en/wp-content/themes/bizvektor-global-edition/pdf/TechnicalData_KGSTOCKGEARS.pdf)

- [25] Line, P. (2004). MSC.Nastran TM 2004. Optimization. Retrieved from <http://www.ae.metu.edu.tr/~ae464/refman.pdf>.
- [26] Ley, W., Wittmann, K., & Hallmann, W. (2009). Handbook of space technology. Wiley.
- [27] Wijker, J. J. (2008). Spacecraft Structures. [electronic resource]. Springer Berlin Heidelberg.
- [28] Thermal Expansion Coefficients. (n.d.). Retrieved December 25, 2019, from <http://www.owl.net.rice.edu/~msci301/ThermalExpansion.pdf>.
- [29] Bai, Z., Zhao, Y., Ma, W., & Tian, H. (2008). Modal analysis for small satellite system with finite element method. 2008 2nd International Symposium on Systems and Control in Aerospace and Astronautics, ISSCAA 2008, 0(3), 3–7. <https://doi.org/10.1109/ISSCAA.2008.4776403>
- [30] Boudjemai, A., Amri, R., Mankour, A., Salem, H., Bouanane, M. H., & Boutchicha, D. (2012). Modal analysis and testing of hexagonal honeycomb plates used for satellite structural design. *Materials & Design*, 266–275. <https://doi.org/10.1016/j.matdes.2011.09.012>
- [31] Pretlove, A. J. (1965). Free vibrations of a rectangular panel backed by a closed rectangular cavity by a closed rectangular cavity. *Journal of Sound and Vibration*, 2(3), 197–209. [https://doi.org/10.1016/0022-460X\(65\)90108-2](https://doi.org/10.1016/0022-460X(65)90108-2)
- [32] Cotoni, V., Shorter, P., & Langley, R. (2007). Numerical and experimental validation of a hybrid finite element-statistical energy analysis method. *The Journal of the Acoustical Society of America*, 122(1), 259–270. <https://doi.org/10.1121/1.2739420>
- [33] Denli, H., & Sun, J. Q. (2007). Structural-acoustic optimization of composite sandwich structures: A review. *Shock and Vibration Digest*, 39(3), 189–200. <https://doi.org/10.1177/0583102406074086>
- [34] Roibas, Elena & Chimeno, Marcos & Martínez-Calvo, B. & Lopez-Díez, J. & Fajardo, Pablo & Fernandez, M.J. & Simon, F.. (2012). Criteria for mathematical model selection for satellite vibro-acoustic analysis depending on frequency range. European Space Agency, (Special Publication) ESA SP. 691.
- [35] Viscardi, M., Arena, M., Barra, G., & Guadagno, L. (2017). Smart carbon-epoxy laminate with high dissipation properties for vibro-acoustic optimization in the turboprop aircraft. *International Journal of Mechanics*, 11(March 2017), 51–57.
- [36] Marshall, P., McQuigg, T., Inoyama, D., Stoumbos, T., & Kapania, R. (2019). Acoustic analysis of spacecraft cavities using the boundary element method. AIAA Scitech 2019 Forum. <https://doi.org/10.2514/6.2019-0203>

- [37] United Launch Alliance. (2010). Atlas V Launch Services User's Guide. Retrieved from <http://www.ulalaunch.com/uploads/docs/AtlasVUsersGuide2010.pdf>
- [38] United Launch Alliance. (2013). Delta IV Launch Services User's Guide. June, (June).
- [39] Space Exploration Technologies. (2009). Falcon 9 Launch Vehicle Payload User's Guide. Retrieved from <https://www.spaceflightnow.com/falcon9/001/f9guide.pdf>.
- [40] Lazan, B.J. Damping of Materials and Members in Structural Mechanics. Oxford Pergamon Press, Oxford, 1968.
- [41] Nanda, B K. Study of the Effect of Bolt Diameter and Washer on Damping in Layered and Jointed Structure. Journal of Sound and Vibration, 2006;290(35): 1290-1314
- [42] Nanda, B K, and A K Behera. Study on Damping in Layered and Jointed Structures with Uniform Pressure Distribution at the Interfaces. Journal of Sound and Vibration, 1999; 226(4): 607-624.
- [43] Turkish Aerospace Space Systems Assembly, Integration and Test Center. Retrived from [https://www.tusas.com/uploads/2019/07/ait\\_center\\_2019-jul-en.pdf](https://www.tusas.com/uploads/2019/07/ait_center_2019-jul-en.pdf).
- [44] Free Field Technologies SA. (2019). MSC ACTRAN 19.1 User's Guide Volume 1, Installation, Operations, Theory and Utilities. 864.
- [45] Siemens Product Lifecycle Management Software Inc. (2014). NX Nastran 10 Quick Reference Guide. 2556.

## APPENDICES

### A. MSC NASTRAN's Composite Calculations

In this part, detailed formulation of NASTRAN about composite modelling will be presented [25].

Deflections at the x, y and z-directions are denoted by U,V and W, respectively and  $\theta$  symbolizes the rotation about those axes.

$$U = U_0 + z\theta_y \quad (22)$$

$$V = V_0 + z\theta_x \quad (23)$$

The relationship between stress and strain are also given below:

$$\begin{Bmatrix} \varepsilon_x \\ \varepsilon_y \\ \gamma_{xy} \end{Bmatrix} = \begin{Bmatrix} \frac{\partial U_0}{\partial x} \\ \frac{\partial V_0}{\partial y} \\ \frac{\partial U_0}{\partial y} + \frac{\partial V_0}{\partial x} \end{Bmatrix} + z \begin{Bmatrix} \frac{\partial \theta_y}{\partial x} \\ -\frac{\partial \theta_x}{\partial y} \\ \frac{\partial \theta_y}{\partial y} - \frac{\partial \theta_x}{\partial x} \end{Bmatrix} = \begin{Bmatrix} \varepsilon_x^0 \\ \varepsilon_y^0 \\ \gamma_{xy}^0 \end{Bmatrix} - z \begin{Bmatrix} \chi_x \\ \chi_y \\ \chi_{xy} \end{Bmatrix} \quad (24)$$

### Tsai-Wu Failure Criterion

For the composite modelling, PCOMP card uses Tsai-Wu Failure criterion. NASTRAN user manual gives the detail of this formulation as [25]:

$$FI = \left(\frac{1}{X_t} - \frac{1}{X_c}\right)\sigma_1 + \left(\frac{1}{y_t} - \frac{1}{y_c}\right)\sigma_2 + \frac{\sigma_1^2}{x_t x_c} + \frac{\sigma_2^2}{y_t y_c} + \frac{\sigma_{12}^2}{s^2} + 2F_{12}\sigma_1\sigma_2 \quad (25)$$

Where X and Y shows the principal 1 and 2 directions of the materials, subscripts 't' and 'c' reflects the tension and compression stress, respectively and 's' shows the allowable shear stress of the material.

## B. Additional Sine Sweep Test Data

In this part additional sine sweep test graphs will be provided. Remember that X-axis graphs of tower and man reflector was provided at Section 0. Here, Y-axis graphs of them are given below. Accelerometers label and corresponding measurement directions, channel ID of data acquisition system, sensitivity, measured maximum response and overload situations are presented in Table 0.1. Responses at normal scale for each test (up to 750Hz) will be also provided below.

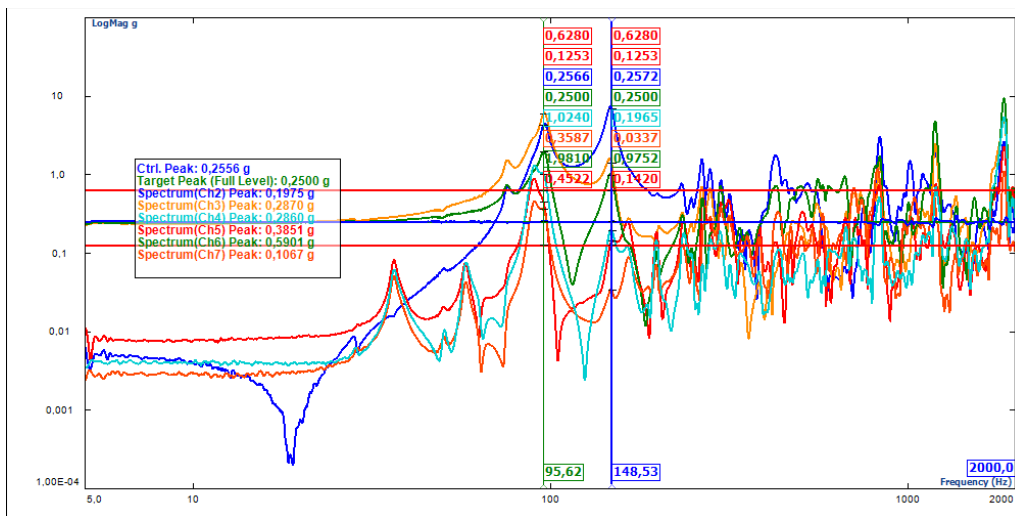


Figure 0.1. Sine Sweep Test Results of Tower in Y-axis

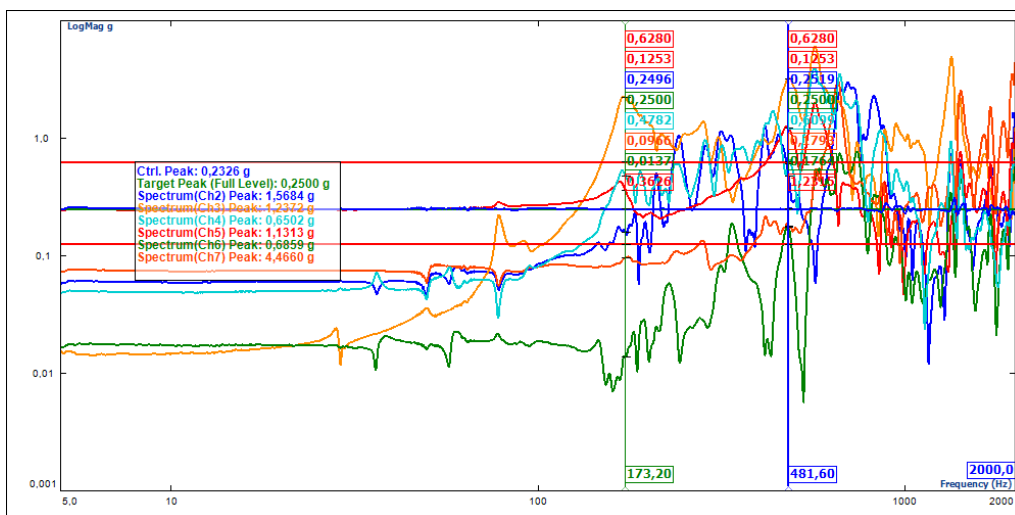


Figure 0.2. Sine Sweep Test Results of Main Reflector in Y-axis

Table 0.1. Situations of Each Channels for Sine Sweep Test

	<b>Accelerometer ID</b>	<b>Direction</b>	<b>Channel ID</b>	<b>Sensitivity (mV/g)</b>	<b>Max (g)</b>	<b>Overload</b>
<b>Tower X-Axis</b>	sr1	N	Ch2	9,607	1.15487	No
	t8	Y	Ch3	9,767	2.63191	No
	t8	X	Ch4	10,3	6.96091	No
	t7	X	Ch5	9,788	4.78043	No
	t5	Y	Ch6	9,729	0.73885	No
	t5	X	Ch7	9,523	2.43856	No
	Fixture	X	Ch8	9,205	0.25981	No
<b>Tower Y-Axis</b>	sr1	N	Ch2	9,607	7.35775	No
	t8	Y	Ch3	9,767	6.16409	No
	t8	X	Ch4	10,3	1.31859	No
	t7	X	Ch5	9,788	0.89623	No
	t5	Y	Ch6	9,729	1.99456	No
	t5	X	Ch7	9,523	0.68109	No
	Fixture	Y	Ch8	9,205	0.26029	No
<b>Main Reflector X-Axis</b>	mr3	N	Ch2	9,205	4.04223	No
	mr4	N	Ch3	10,3	1.41251	No
	mr1	N	Ch4	9,767	8.48810	No
	mr5	Y	Ch5	9,507	0.58496	No
	mr5	X	Ch6	9,788	1.68626	No
	mr5	Z	Ch7	9,729	1.60690	No
	Fixture	X	Ch8	9,523	0.25960	No
<b>Main Reflector Y-Axis</b>	mr3	N	Ch2	9,205	2.98749	No
	mr4	N	Ch3	10,3	6.01916	No
	mr1	N	Ch4	9,767	3.96032	No
	mr5	Y	Ch5	9,507	2.01081	No
	mr5	X	Ch6	9,788	0.76832	No
	mr5	Z	Ch7	9,729	3.07303	No
	Fixture	Y	Ch8	9,523	0.25994	No

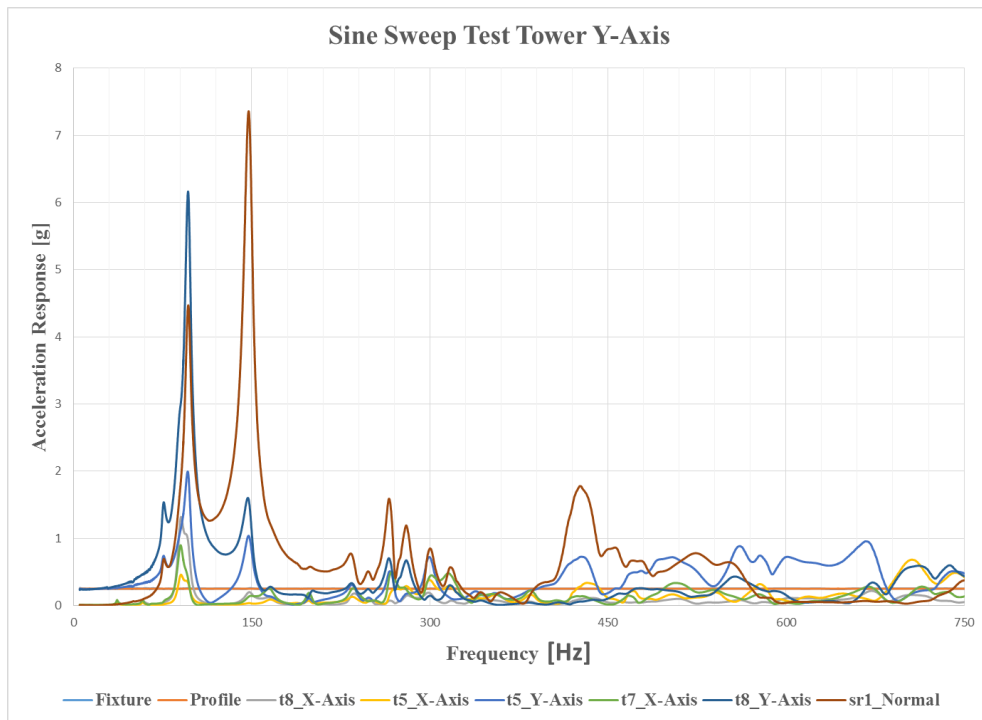


Figure 0.3. Sine Sweep Test Results of Tower Y-Axis (up to 750Hz)

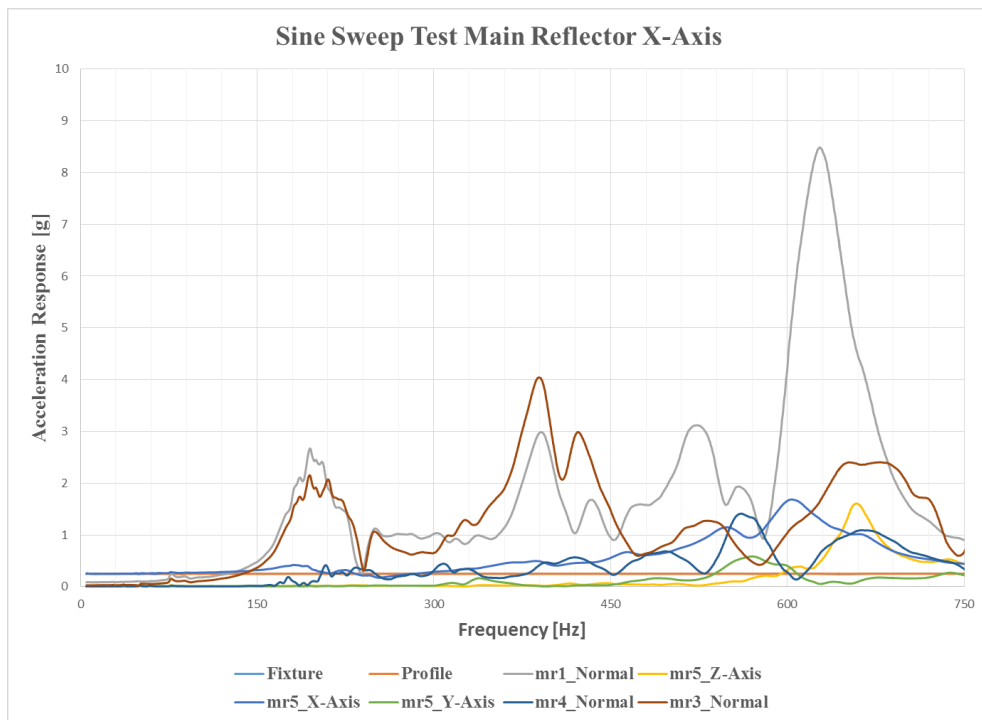


Figure 0.4. Sine Sweep Test Results of Main Reflector X-Axis (up to 750Hz)

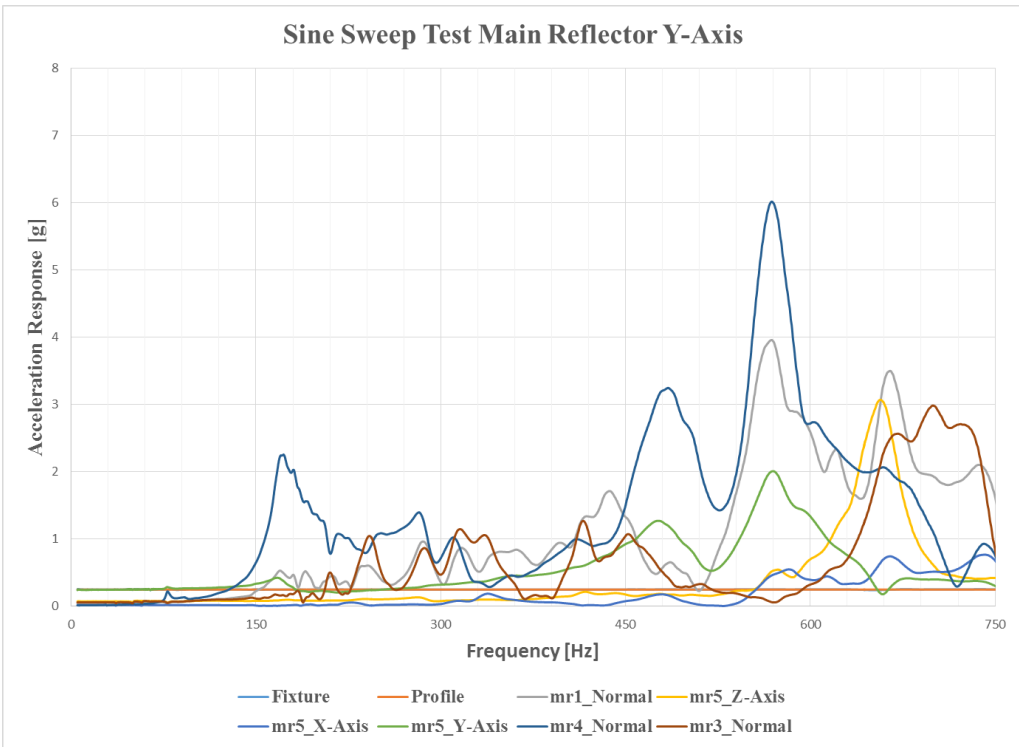


Figure 0.5. Sine Sweep Test Results of Main Reflector Y-Axis (up to 2000Hz)

Table 0.2. 273 Natural Frequencies of Tower Subassembly

91.7	408.7	661.9	918.5	1133.9	1318.0	1487.2	1673.9	1822.8	1984.4
96.9	415.4	663.9	933.1	1138.8	1321.8	1501.3	1692.2	1829.0	1988.9
167.4	421.0	675.5	937.2	1144.0	1323.4	1505.7	1698.3	1837.1	1995.0
177.5	444.4	682.3	947.1	1151.3	1329.6	1516.2	1702.5	1846.3	
179.1	451.2	691.3	953.2	1153.5	1334.9	1520.2	1703.5	1854.3	
189.5	457.8	697.1	957.0	1157.6	1339.0	1523.6	1704.5	1856.3	
199.0	462.1	707.2	958.0	1159.8	1350.1	1526.5	1709.2	1859.5	
211.6	465.8	721.1	963.6	1162.4	1352.0	1537.2	1721.9	1862.4	
216.4	473.8	723.9	974.9	1166.5	1353.2	1538.8	1723.8	1865.2	
218.7	482.0	727.7	979.7	1171.7	1358.8	1543.5	1725.6	1869.2	
237.0	487.6	739.8	985.9	1180.6	1363.4	1547.4	1731.6	1878.6	
241.0	499.3	745.3	994.1	1186.7	1378.9	1550.5	1736.5	1881.2	
251.3	509.5	750.8	995.7	1198.0	1384.8	1559.7	1740.4	1885.3	
253.5	513.9	766.0	1001.8	1203.9	1394.7	1561.2	1748.9	1889.2	
255.6	516.3	775.8	1006.8	1208.5	1395.1	1567.8	1750.0	1891.4	
260.9	523.5	791.6	1011.2	1215.5	1396.4	1574.1	1752.7	1892.8	
273.8	535.9	805.6	1017.2	1220.8	1412.2	1585.6	1758.7	1899.5	
280.1	545.4	810.4	1017.7	1226.1	1422.5	1590.0	1761.3	1912.0	
285.6	559.7	811.3	1031.7	1231.8	1429.0	1594.6	1765.2	1925.6	
288.2	569.7	816.0	1035.7	1239.0	1430.5	1606.0	1768.8	1926.4	
299.9	570.6	820.4	1036.7	1241.3	1435.7	1616.8	1771.0	1931.4	
310.2	591.3	831.8	1059.6	1244.6	1439.5	1620.8	1785.1	1934.5	
313.4	596.5	838.0	1065.0	1258.9	1444.9	1626.1	1786.0	1939.1	
332.3	605.8	851.9	1079.2	1274.0	1452.0	1630.3	1793.2	1945.0	
334.2	624.8	864.2	1085.2	1278.5	1454.8	1634.4	1800.6	1948.6	
342.2	630.0	871.8	1089.8	1285.1	1463.9	1642.4	1801.6	1955.5	
346.4	636.7	879.4	1096.8	1294.0	1472.6	1645.3	1805.5	1960.7	
357.8	647.0	892.9	1107.3	1298.5	1475.5	1658.1	1809.0	1971.5	
373.0	652.4	900.6	1116.3	1301.5	1475.8	1661.7	1817.4	1977.7	
382.6	658.7	905.6	1123.1	1313.5	1484.2	1665.6	1818.7	1982.2	

Table 0.3. 250 Natural Frequencies of Main Reflector Subassembly

199.0	724.6	1009.8	1207.4	1380.6	1550.8	1698.1	1837.5	1958.2
216.4	735.3	1012.7	1216.2	1387.2	1556.1	1700.2	1839.2	1960.5
243.0	738.3	1013.5	1220.3	1388.5	1559.4	1704.3	1850.5	1962.0
244.3	751.2	1023.8	1224.5	1404.8	1569.9	1706.7	1852.5	1965.0
257.3	755.9	1036.1	1226.9	1409.0	1571.4	1709.0	1857.5	1967.1
283.9	765.1	1049.0	1235.7	1412.8	1579.1	1714.5	1860.5	1970.5
297.2	773.7	1051.0	1241.2	1417.4	1582.8	1723.5	1863.0	1972.2
317.3	782.6	1056.6	1242.3	1423.3	1586.9	1727.6	1869.4	1974.8
361.2	794.0	1058.4	1251.0	1431.7	1590.5	1729.4	1872.1	1978.5
414.4	795.4	1072.0	1255.0	1436.8	1595.5	1735.5	1874.2	1983.7
431.5	806.2	1077.5	1260.0	1447.8	1598.9	1748.7	1877.2	
457.5	825.9	1081.9	1266.3	1449.7	1600.5	1751.0	1882.0	
476.2	841.6	1092.1	1275.3	1453.1	1603.9	1758.0	1884.9	
495.5	848.0	1097.2	1280.5	1463.0	1607.9	1762.9	1888.3	
500.0	868.5	1098.4	1288.1	1468.3	1612.6	1764.5	1897.2	
513.2	883.2	1109.4	1294.7	1474.3	1616.7	1768.1	1903.3	
525.5	887.2	1115.8	1298.5	1478.3	1618.6	1775.8	1906.6	
528.7	889.1	1121.0	1304.6	1482.6	1624.6	1781.5	1908.2	
536.5	892.0	1123.7	1308.5	1486.1	1629.7	1789.3	1916.2	
571.9	906.2	1130.3	1315.2	1488.8	1637.8	1793.0	1922.4	
578.7	916.8	1132.7	1323.2	1497.1	1644.2	1796.8	1923.6	
584.5	932.9	1144.5	1326.0	1506.8	1652.6	1801.6	1926.5	
598.2	938.9	1148.0	1327.5	1509.9	1656.7	1803.8	1931.6	
606.6	952.3	1155.8	1332.0	1512.3	1660.6	1808.1	1935.8	
611.3	968.2	1158.6	1343.2	1517.3	1666.7	1811.8	1936.2	
639.7	971.4	1163.7	1349.4	1523.7	1671.2	1813.1	1941.5	
642.0	980.4	1173.5	1358.3	1532.0	1673.6	1817.1	1945.1	
657.8	985.7	1189.0	1360.4	1534.5	1684.7	1827.3	1946.8	
674.1	995.6	1196.7	1365.9	1538.6	1689.8	1827.6	1951.5	
675.4	999.2	1199.5	1369.7	1547.9	1691.1	1836.3	1955.0	